44889

National Library of Canada / Bibliothèque nationale du Canada

CANADIAN THESES ON MICROFICHE / THÈSES CANADIENNES SUR MICROFICHE

NAME OF AUTHOR/NOM DE L'AUTEUR Graeme Alexander Dewar

TITLE OF THESIS/TITRE DE LA THÈSE Ferromagnetic Antiresonant Microwave Transmission through Nickel

UNIVERSITY/UNIVERSITÉ Simon Fraser University

DEGREE FOR WHICH THESIS WAS PRESENTED/ GRADE POUR LEQUEL CETTE THÈSE FUT PRÉSENTÉE Doctor of Philosophy

YEAR THIS DEGREE CONFERRED/ANNÉE D'OBTENTION DE CE DEGRÉ 1979

NAME OF SUPERVISOR/NOM DU DIRECTEUR DE THÈSE Professor J. F. Cochran

DATED/DATÉ _____ SIGNED/SIGNÉ _____

PERMANENT ADDRESS/RÉSIDENCE FIXE [redacted]

NOTICE

The quality of this microfiche is heavily dependent upon the quality of the original thesis submitted for microfilming. Every effort has been made to ensure the highest quality of reproduction possible.

If pages are missing, contact the university which granted the degree.

Some pages may have indistinct print especially if the original pages were typed with a poor typewriter ribbon or if the university sent us a poor photocopy.

Previously copyrighted materials (journal articles, published tests, etc.) are not filmed.

Reproduction in full or in part of this film is governed by the Canadian Copyright Act, R.S.C. 1970, c. C-30. Please read the authorization forms which accompany this thesis.

THIS DISSERTATION HAS BEEN MICROFILMED EXACTLY AS RECEIVED

AVIS

La qualité de cette microfiche dépend grandement de la qualité de la thèse soumise au microfilmage. Nous avons tout fait pour assurer une qualité supérieure de reproduction.

S'il manque des pages, veuillez communiquer avec l'université qui a conféré le grade.

La qualité d'impression de certaines pages peut laisser à désirer, surtout si les pages originales ont été dactylographiées à l'aide d'un ruban usé ou si l'université nous a fait parvenir une photocopie de mauvaise qualité.

Les documents qui font déjà l'objet d'un droit d'auteur (articles de revue, examens publiés, etc.) ne sont pas microfilmés.

La reproduction, même partielle, de ce microfilm est soumise à la Loi canadienne sur le droit d'auteur, SRC 1970, c. C-30. Veuillez prendre connaissance des formules d'autorisation qui accompagnent cette thèse.

LA THÈSE A ÉTÉ MICROFILMÉE TELLE QUE NOUS L'AVONS REÇUE

FERROMAGNETIC ANTIRESONANT MICROWAVE TRANSMISSION THROUGH NICKEL

by

Graeme A. Dewar

B.Sc., Bishop's University

A THESIS SUBMITTED IN PARTIAL FULFILLMENT

OF THE REQUIREMENTS FOR THE DEGREE OF

DOCTOR OF PHILOSOPHY

in the Department

of

Physics

SIMON FRASER UNIVERSITY

June 1978

PARTIAL COPYRIGHT LICENSE

I hereby grant to Simon Fraser University the right to lend my thesis or dissertation (the title of which is shown below) to users of the Simon Fraser University Library, and to make partial or single copies only for such users or in response to a request from the library of any other university, or other educational institution, on its own behalf or for one of its users. I further agree that permission for multiple copying of this thesis for scholarly purposes may be granted by me or the Dean of Graduate Studies. It is understood that copying or publication of this thesis for financial gain shall not be allowed without my written permission.

Title of Thesis/Dissertation:

Ferromagnetic Antiresonant Microwave Transmission through Nickel

Author:

(signature)

Graeme Alexander DEWAR

(name)

(date)

APPROVAL

Name: Graeme A. Dewar

Degree: Doctor of Philosophy

Title of Thesis: Ferromagnetic Antiresonant Microwave Transmission through Nickel.

Examining Committee:

Chairman: Suso Gygax

John F. Cochran
Senior Supervisor

Anthony S. Arrott

Richard H. Enns

Bretislav Heinrich

Thomas R. Carver
External Examiner
Professor
Princeton University, Princeton New Jersey

Date Approved: 22. June 78

ABSTRACT

The temperature dependence of the ferromagnetic anti-resonant (FMAR) transmission of 24 GHz microwaves through polycrystalline and single crystal nickel samples has been studied. Between 300K and 637K measurements of transmission amplitude vs. magnetic field can be described by the usual equation of motion for the magnetization using a Landau-Lifshitz damping parameter of $2.45 \pm .1 \times 10^{8} sec^{-1}$ and a g-factor of $2.187 \pm .005$, both temperature independent.

Meausrements of the maximum transmission amplitude at FMAR vs. temperature were obtained between 120K and 637K. These measurements confirmed the temperature independence of the damping above 300K and indicated a rapid increase in the damping below 200K. This increase in the damping is in agreement with the results Bhagat and Hirst (1966) obtained from ferromagnetic resonance absorption measurements.

The FMAR transmission signal was too small to be observed below 45 ± 5K. A second transmissi on peak at an applied field corresponding to ferromagnetic resonance developed at temperatures less than 40K. The origin of this new transmission peak is not clear.

ACKNOWLEDGEMENT

First, and foremost, I wish to acknowledge the many pleasant hours spent with John Cochran discussing various aspects of the experiments and results related in this thesis, as well as myriads of other conversational forrays into physics.

To Bretislav Heinrich go my thanks for innumerable tips on working with fragile samples and for his perpetual willingness to lend a hand or toss out a blend of advice and ideas.

I note here my thanks to Rick Baartman for the many exchanges of information, not uncommon to people working on closely related topics. To Andrew Kurn go my thanks for those eleventh hour resurrections of buried data sets.

Thanks, too, to Frank Wick and the guys in the machine shop who produced for me two major pieces of apparatus which functioned well beyond expectation. Also, I appreciate the able assistance I received from the Physics Department's technicians. And, thank you, Marion Jacques, for converting a randomly ordered hodgepodge of hand-printed scrawls and computer printed hard copy into a readable form, all the while maintaining a cool head as whole chapters, conceived and created, refused to be delivered.

Finally, I wish to acknowledge the financial support of the National Research Council of Canada and Simon Fraser University which made this work possible.

TABLE OF CONTENTS

	Page
Approval	ii
Abstract	iii
Acknowledgements	iv
List of Tables	vii
List of Figures	viii
I. INTRODUCTION	1
II. TRANSMISSION CALCULATION	9
2.1 Conductivity	10
2.2 Dielectric Constant	11
2.3 Permeability	12
2.4 Maxwell's Equations and Propagation Constant	24
2.4a Perpendicular Configuration	24
2.4b Parallel Configuration	29
2.5 The Boundary Value Problem	33
2.5a Perpendicular Configuration	33
2.5b Parallel Configuration	37
2.6 Example Calculations	38
III. EXPERIMENT	49
3.1 Microwave Circuit	49
3.2 Microwave Cavities	51
3.3 Magnet System	59
IV. TRANSMISSION MEASUREMENTS ON POLYCRYSTALLINE NICKEL	60
4.1 Samples and Sample Preparation	60
4.2 Analysis of Data	66

		Page
4.2a	$T < T_c$	66
4.2b	$T \approx T_c$	70
4.2c	The Role of Strain	74
4.3	Results	78
4.3a	Damping Parameter	78
4.3b	Maximum Transmission Amplitude	84
4.3c	g-factor	88
4.3d	Transmission above T_c	90
4.3e	Magnetization	95
V.	NICKEL SINGLE CRYSTAL MEASUREMENTS	98
5.1	Sample Preparation	100
5.2	Transmission Experiments	104
5.3	Results: 77K to 300K	105
5.3a	Sample Characterization	105
5.3b	Damping Parameter	109
5.4	Discussion of Results: 77K to 300K	113
5.5	Results: 4K to 77K	117
5.6	Discussion of Results: 4K to 77K	124
VI.	CONCLUSION	125
	APPENDIX I	129
	APPENDIX II	136
	APPENDIX III	139
	APPENDIX IV	143
	REFERENCES	148

LIST OF TABLES

Table		Page
2.1	Parameters used for calculations shown in Figs. 2.6 to 2.9, unless otherwise stated ...	40
4.1	Physical parameters of samples	63
4.2	Parameters determined from transmission measurements at 364°C, Figs. 4.4 and 4.5	81
5.1	Parameters used in transmission calculation for comparison with NiSgLXtL#3 room temperature measurements	107
A.1	R.F. demagnetization factors: special cases for cubic anisotropy	134
A.2	R.F. demagnetization factors: uniform planar strain	135

LIST OF FIGURES

Figure		Page
1.1	Transmission amplitude vs. magnetic field at 224°C, perpendicular configuration	3
1.2	Transmission amplitude vs. magnetic field at 224°C, parallel configuration	4
2.1	Vector quantities entering Equations (2.6) and (2.7)	14
2.2	Geometrical illustration of the Landau-Lifshitz, Gilbert, and Bloembergen forms of damping	17
2.3	Co-ordinate systems fro the description of the sample orientation and for the equation of motion of the magnetization	21
2.4	The real and imaginary parts of the permeability μ_+	30
2.5	Schematic of waves involved in the boundary value problem	34
2.6	Transmitted amplitude vs. magnetic field showing the effect of different g-factors and damping parameters	42
2.7	Transmitted amplitude vs. magnetic field for the parallel and perpendicular configurations	44
2.8	Calculated amplitude vs. phase of transmitted signal for two thickness-damping combinations	45
2.9	Transmitted amplitude vs. magnetic field illustrating the effect of magnetostriction..	47
3.1	Microwave circuit schematic	52
3.2	View of cavities and sample	54
3.3	Schematic of beryllium-copper cavities	58
4.1	Measured resistivity of nickel foil as a function of temperature	65
4.2	Transmission amplitude vs. magnetic field at 272°C, parallel configuration	68

Figure		Page
4.3	Transmission amplitude vs. magnetic field at 272°C, perpendicular configuration	69
4.4	The calculated shift of the position of the FMAR peak in the perpendicular configuration caused by thermal strain vs. temperature	76
4.5	Landau-Lifshitz damping parameter for nickel as a function of temperature	79
4.6	Bloembergen damping parameter for nickel vs. temperature	82
4.7	Maximum transmission amplitude at FMAR plotted as a function of temperature	86
4.8	The g-factor of nickel plotted as a function of temperature.....	89
4.9	Calculated permeability of nickel at various temperatures	91
4.10	Transmission amplitude vs. magnetic field at 364°C, parallel configuration	92.
4.11	Transmission amplitude vs. magnetic field at 364°C, perpendicular configuration	93
4.12	Magnetization as a function of temperature ..	96
5.1	Sample and diaphragm	102
5.2	Transmission amplitude vs. magnetic field for Ni8μ	108
5.3	Landau-Lifshitz damping parameter vs. temperature for Ni8μ	112
5.4	Transmission amplitude vs. magnetic field for Ni3	118
5.5	Calculated transmission amplitude vs. magnetic field for 4.2μm and 2.8μm thicknesses	119
5.8	Measured transmission amplitude vs. magnetic field for Ni3μ at various temperatures	121
AIV.1	Side and end schematic views of electro-polishing apparatus	146
AIV.2	Sample mounting detail	147

CHAPTER 1

INTRODUCTION

The physics community has exerted a great deal of effort on the study of the radio frequency properties of magnetic materials since Griffiths (1946) first demonstrated that a magnetic field influenced the surface impedance of nickel. The microwave absorption maxima Griffiths observed became known as ferromagnetic resonance (FMR). From the surface impedance extracted from ferromagnetic resonance experiments one could obtain information about the magnetization, g-factor, magnetic anisotropy, magnetic damping, exchange, and the surface pinning of a ferromagnetic metal (MacDonald 1951, Ament and Rado 1955, Rado and Weertman 1959). In practice, the shape of the magnetic field dependent surface impedance near FMR depends in a very complex manner on all the above parameters, making it difficult to disentangle effects due to magnetic damping from effects due to exchange and surface pinning.

Heinrich and Meschyerakov (1969, 1970) showed that permalloy exhibited a peak in the transmitted microwave signal at an applied magnetic field which corresponded to a minimum in the radio frequency permeability (real part of $\mu_{RF} = 0$). This phenomenon is known as ferromagnetic antiresonant (FMAR) transmission. The enhanced transmission at FMAR of a ferromagnetic metal was predicted by Kaganov (1959) and is related to the microwave transmission maxima discovered earlier in

gadolinium by Lewis et al. (1966).

This FMAR transmission peak arises because the permeability modulates the skin depth of the microwave radiation within the magnetic metal[1]. Depending on the metal, the permeability can increase the decay length of the radiation by a factor of from five to ten. Since the transmitted signal depends exponentially on the inverse decay length, the transmitted signal can vary by orders of magnitude as the magnetic field is swept through FMAR. Typical examples of FMAR transmission through nickel are illustrated in Figs. 1.1 and 1.2.

Heinrich and Mescheryakov have shown that the magnetic field dependence of the transmission of radiation through ferromagnetic metals can be used to obtain the g-factor, saturation magnetization, and damping uncomplicated by effects due to exchange and surface pinning. Thus the FMAR transmission technique is more attractive than the FMR absorption technique for determining these material parameters. Further, FMAR transmission is a bulk phenomenon; it is insensitive to surface pinning and the RF radiation probes the total thickness of the sample. This differs from FMR for which the shape and position of the FMR absorption line are dependent upon the degree of surface pinning, and for which only a layer approximately 100 Å thick is probed by 24 GHz radiation. FMAR measurements are, therefore, far less sensitive to the condition of the sample surfaces than

---

[1]Of course, the permeability also plays a role in determining how much radiation is reflected and transmitted at the surface of the metal.

Fig. 1.1: Transmission amplitude vs. applied magnetic field for a polycrystalline specimen. The magnetic field was parallel to the plane of the disc shaped sample. The temperature was 224°C. The calculated transmission (solid line) is normalized to the experimental peak amplitude (points). Parameters used for the calculated transmission are: R.F. frequency = 23.825 GHz, g = 2.187, M_o = 377 Gauss, resistivity = 17.82×10^{-6} Ω-cm, thickness = 19.12 μm, and $\lambda = 2.45 \times 10^{8} sec^{-1}$.

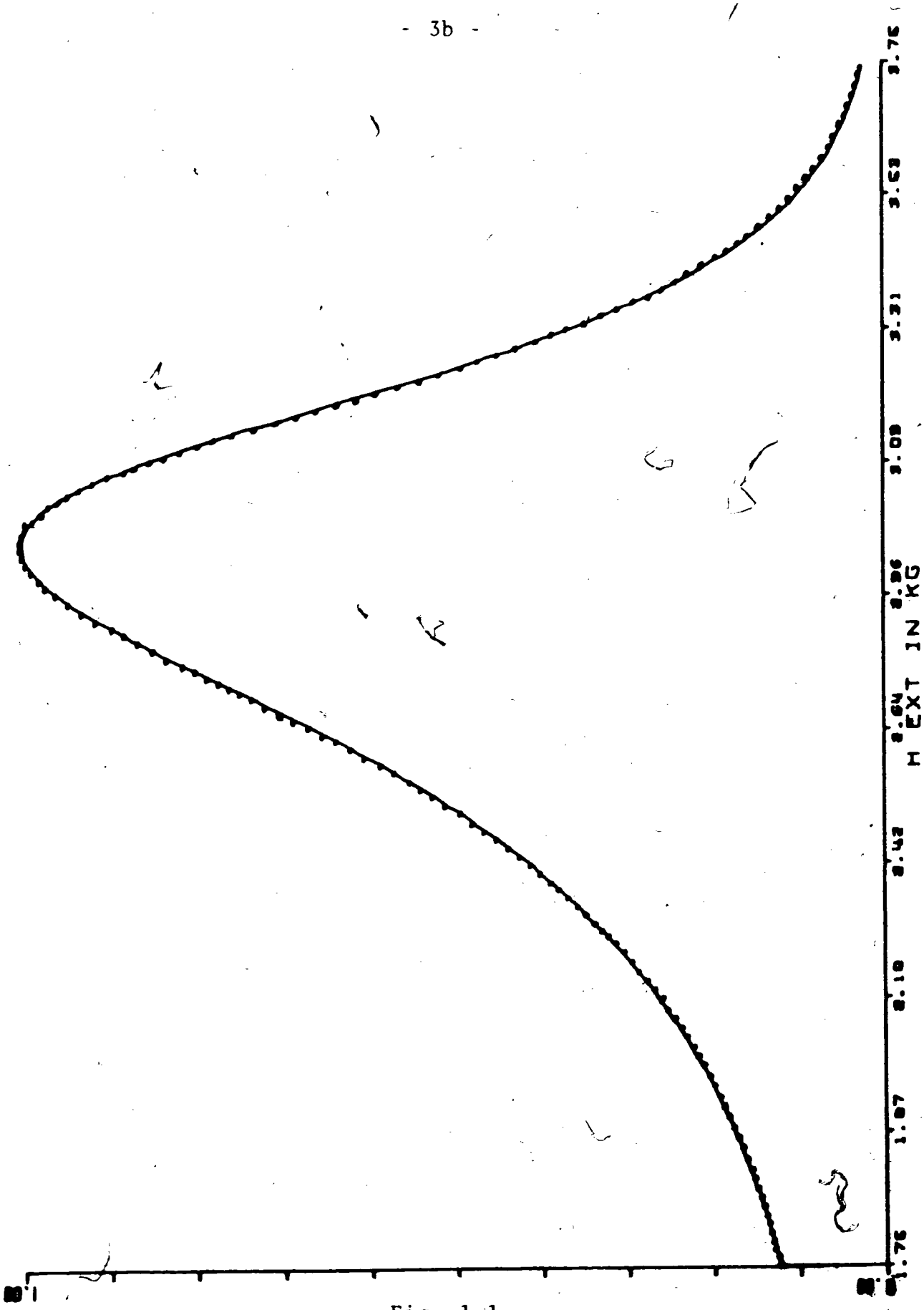

Fig. 1.1

Fig. 1.2: Transmission amplitude vs. applied magnetic field for the same polycrystalline sample as in Fig. 1.1 but with the applied field normal to the plane of the sample. Parameters used for the calculation (solid line) are: R.F. frequency = 23.825 GHz, g = 2.187, M_o = 377 Gauss, resistivity = 17.82×10^{-6} Ω-cm, thickness = 19.12 μm, and $\lambda = 2.45 \times 10^{8} sec^{-1}$. The data (points) were obtained at 224°C.

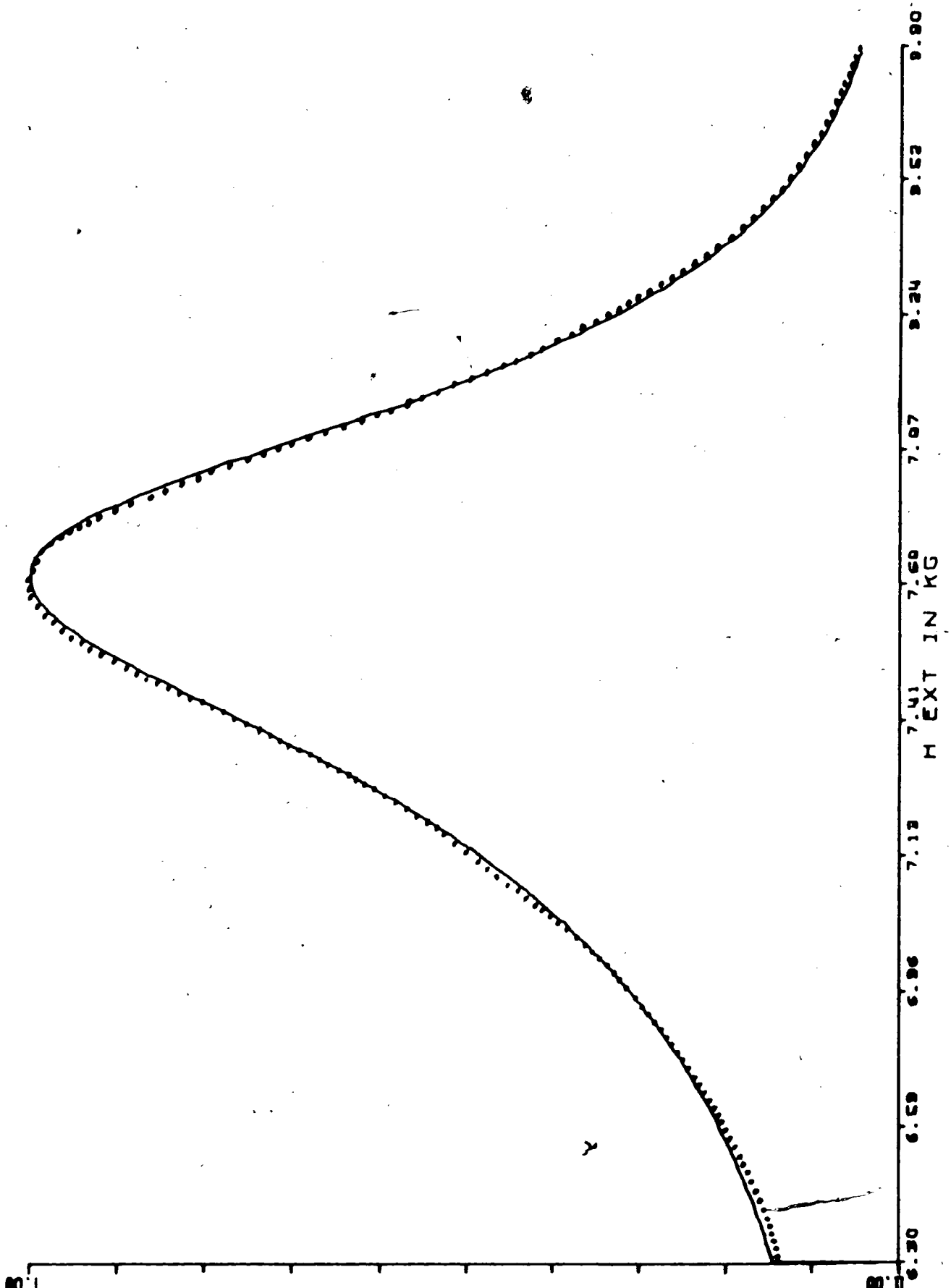

Fig. 1.2

FMR measurements and this minimizes problems associated with the preparation of reproducibly clean, smooth surfaces.

Most of this thesis concerns the study of the R.F. magnetic properties of nickel using the FMAR transmission technique. The type of data available from experiment is exemplified by Figs. 1.1 and 1.2. The calculated curves were fitted to the two sets of data using only four parameters: two line positions (g-factor and magnetization) and two linewidths (damping)[2]. The close agreement between the data and calculation demonstrate the confidence one can place in this method for determining material parameters.

The motivation behind using the microwave transmission technique to study nickel was two-fold. First, previous FMR measurements made by Bhagat and Chichlis (1969) had indicated that the high temperature magnetic damping for nickel, i.e. the damping for temperatures of the order of the Curie temperature of 357°C, was half the room temperature value. Also, the g-factor displayed a slight temperature dependence. Both these results were in disagreement with the results of FMR experiments performed earlier by Rodbell (1965). Rodbell had reported that both the magnetic damping and g-factor for nickel were temperature independent over the range -120°C to 360°C. Moreover, Bhagat and Rothstein (1971) suggested that the usual phenomenological approach to describing the dynamic

---

[2]The damping parameter used in the calculations shown in Figs. 1.1 and 1.2 were not constrained to be equal.

response of the magnetization (see Chapter 2) was incapable of describing FMR absorption measurements on nickel at temperatures near the Curie temperature. Since the magnetic damping in nickel is more than twice as large as for the other ferromagnetic 3-d transition metals, and the microscopic origin of damping in nickel for this temperature range is not clearly understood, a re-examination of nickel's R.F. magnetic properties using the FMAR transmission technique was in order. The results of this investigation, described in Chapter 4, indicate that both the magnetic damping and g-factor for nickel were temperature independent between room temperature and 364°C.

Second, Bhagat and Hirst (1966) discovered that nickel's FMR absorption linewidth rapidly increased as the temperature was decreased below room temperature. The interpretation of this observation is complicated by the role the conductivity plays in determining the FMR absorption linewith. In order to analyze their data, Bhagat and Hirest calculated the surface impedance of nickel in the anomalous skin effect régime, i.e. in the régime in which the mean free path of the conduction electrons is longer than the characteristic wavelength of the R.F. radiation in the metal. The results obtained using the non-local conductivity appropriate to the anomalous skin effect régime showed that the damping parameter for nickel at temperatures less than 50K was six times larger than the room temperature value. The temperature range over which the damping increased to the low temperature value coincided with

the onset of the anomalous skin effect régime. The FMAR transmission measurements described in Chapter 5 were undertaken in order to remove any doubt that the increased low temperature damping was not an artifact of the anomalous skin effect régime. The wavelength of the R.F. radiation in a ferromagnetic metal is much longer at FMAR than at FMR and, hence, the anomalous skin effect sets in at a lower temperature for the FMAR measurement. Thus the interpretation of the FMAR transmission measurement is not complicated by effects due to a non-local conductivity over the temperature range in which Bhagat and Hirest reported the magnetic damping to rapidly increase. The results of the FMAR measurements, described in detail in Chapter 5, do indeed confirm this rapid increase of the magnetic damping.

A new peak was observed in the magnetic field dependent transmission of microwaves through nickel. This peak occurred at a magnetic field corresponding to FMR and was most pronounced at temperatures below 20K. The nature of this peak is not clear and further experiments beyond the scope of this thesis are necessary to elucidate the origin of this transmission peak.

The remainder of this thesis is organized as follows. In Chapter 2 the transmission calculation is described. The relevant material parameters are introduced, three possible phenomenological statements of the equation of motion for the magnetization are developed, and Maxwell's equations are

solved to find the transmitted microwave field for two specific cases appropriate to the experiment. The chapter ends with several example calculations which illustrate the information one can obtain from microwave transmission measurements.

Chapter 3 deals with the experimental apparatus used to take the measurements. A detailed description of the microwave cavities used in the various temperature ranges covered in the experiments is presented along with a short description of the microwave circuit and magnet system.

Chapter 4 and Chapter 5 contain the descriptions and results of the high temperature and low temperature measurements, respectively. The substance of these chapters has been stated above.

Chapter 6 concludes the thesis with a summary of the major results and conclusions which can be drawn from them. Finally, some follow-up experiments pertaining to the new transmission peak are suggested.

CHAPTER 2

TRANSMISSION CALCULATION

The calculation of the outcome of a microwave transmission experiment breaks naturally into two parts. First, one must describe the relevant properties of the material being studied. For our purposes these are the properties which enter Maxwell's equations through the constitutive relations, namely the conductivity, the dielectric constant, and the permeability. Second, one must solve a boundary value problem. In this problem microwaves are incident on one side of a slab of material and one determines the amplitude and phase of the microwave signal emerging from the other side of the slab.

This chapter is organized as follows. Brief discussions of the conductivity and dielectric constant are followed by an extensive description of the permeability as a function of applied magnetic field. A simplified expression for the permeability, combined with Maxwell's equations, is used to solve the boundary value problem in two particular but important cases. A more complete expression for the permeability is given in Appendix II. Finally, a series of plots of transmitted signal vs. applied magnetic field is presented which show how sensitive these plots are to the material parameters used in the calculation. This illustrates how material properties can be accurately determined by comparing the calculations with the experimental data.

2.1 Conductivity

The conductivity enters into the calculation outlined here through Ohm's Law.

$$\vec{j} = \sigma \vec{e} \qquad (2.1)$$

Here $\vec{j}$, σ, and $\vec{e}$ are the current density, conductivity, and electric field, respectively. The conductivity appropriate to our experiments is ordinarily the d.c. conductivity. (It is not appropriate to use the simple d.c. conductivity if the electron mean free path is longer than the skin depth. This case is discussed in Chapter 5.) The microwave electric fields appear static to the electrons in the metal because their collision time ($\approx 10^{-14}$sec, Mott and Jones 1936) is much shorter than the microwave period ($\approx 10^{-10}$sec). Additionally, the electron mean free path ($\approx 10^{-6}$cm, Mott and Jones 1936) is short in comparison to the skin depth (10^{-4}cm). Thus the microwave electric fields appear constant in time and space throughout the lifetime of a given electron state. Moreover, magnetoresistive effects are small (Potter 1931, Marcus and Langenberg 1963). Under these conditions the simple d.c. conductivity used in Equation (2.1) yields an adequate description of the electron response to the microwave electric field.

A note of caution is in order here. The microwave signal inside a ferromagnetic metal includes a part which is essentially a driven spin wave. This spin wave can be

characterized by a decay length $\approx 10^2$ times shorter than the skin depth for the electromagnetic wave, i.e. the spin wave decays in a length comparable to the electron mean free path. In this case the d.c. conductivity is not appropriate and Ohm's Law is invalid. Fortunately, these spin waves have very little effect on transmission at FMAR. (See Cochran et al. 1977(a).) Further discussion of this point is postponed until Chapter 5.

2.2 Dielectric Constant

The dielectric constant, ε, enters into the calculation in the familiar Maxwell equation,

$$\nabla \times \vec{h} = \frac{4\pi}{c} \vec{j} + \frac{\varepsilon}{c} \frac{\partial \vec{e}}{\partial t} \qquad (2.2)$$

Using Ohm's Law, Equation (2.1), and allowing the electromagnetic fields to have the time and frequency dependence $\exp(i\omega t)$, Equation (2.2) becomes:

$$\nabla \times \vec{h} = \left(\frac{4\pi\sigma + i\varepsilon\omega}{c} \right) \vec{e} \qquad (2.3)$$

Typically, $\sigma \approx 10^{17}\ \text{sec}^{-1}$ and $\omega \approx 10^{11}\ \text{sec}^{-1}$. The dielectric constant is a number of the order of unity and, hence, the term containing ε in Equation (2.3) is $\approx 10^7$ times smaller than the term containing the conductivity. This means that the displacement current is much smaller than the conduction current over the frequency range of interest here. Therefore, the term containing the dielectric constant can be ignored.

2.3 Permeability

The microwave properties of interest in ferromagnetic metals manifest themselves in the radio frequency permeability or, equivalently, in the radio frequency susceptibility. Essentially, the permeability includes in Maxwell's equations the effects of the response of the magnetization to the electromagnetic radiation in the metal.

Consider a unit volume of magnetic material of magnetization $\vec{M}$ in an external magnetic field $\vec{H}$. This magnetic field exerts a torque $\vec{L}$, where

$$\vec{L} = \vec{M} \times \vec{H} \qquad (2.4)$$

on the angular momentum $\vec{J}$ of the magnetic carriers. The magnetization is related to the angular momentum by

$$\vec{M} = -\gamma \vec{J} \qquad (2.5)$$

where $\gamma = |ge/2mc|$ is the magnetomechanical ratio. Here e,m, and g are the electronic charge, mass, and spectroscopic splitting factor[1]. Using the usual relation between torque and angular momentum,

$$\text{i.e.} \quad \vec{L} = \frac{d}{dt}\vec{J} \qquad (2.6)$$

---

[1] The name "spectroscopic splitting factor" is reserved for the g-factor appropriate to an electromagnetic experiment. The g-factor found in a mechanical experiment is called the "magnetomechanical factor". For a discussion of the difference between these two g-factors, see Kittel (1949).

as well as Equations (2.4) and (2.5), one obtains the following equation of motion for the magnetization:

$$\frac{d\vec{M}}{dt} = -\gamma (\vec{M} \times \vec{H}) \qquad (2.7)$$

This results in the familiar precession of the magnetization about the applied magnetic field, Fig. 2.1. Note, however, that the case considered here is unlike the situation one considers in nuclear magnetic resonance where each spin precesses independently of all the others in one of a few quantized states. Here the exchange interaction locks the spins of the individual electrons together and the magnetization, characterized by a quantum number $\gtrsim 10^{22}$ precesses about the external field. This justifies the classical description employed throughout this discussion.

Equation (2.7) is not complete because there is no means for the magnetization to reach its lowest energy configuration with $\vec{M} \parallel \vec{H}$. In magnetic metals the magnetization attains its equilibrium direction very quickly ($\lesssim 10^{-8}$ sec). The detailed description of the relaxation of the magnetization to its equilibrium direction should be based on a microscopic theory which includes a mechanism whereby individual spins flip and give up magnetic energy to the lattice. No such complete theory exists for the materials we are interested in. A possible microscopic mechanism which may account for part of the magnetic relaxation in nickel is described by Kambersky (1970) and by Korenman and Prange (1972). This mechanism is

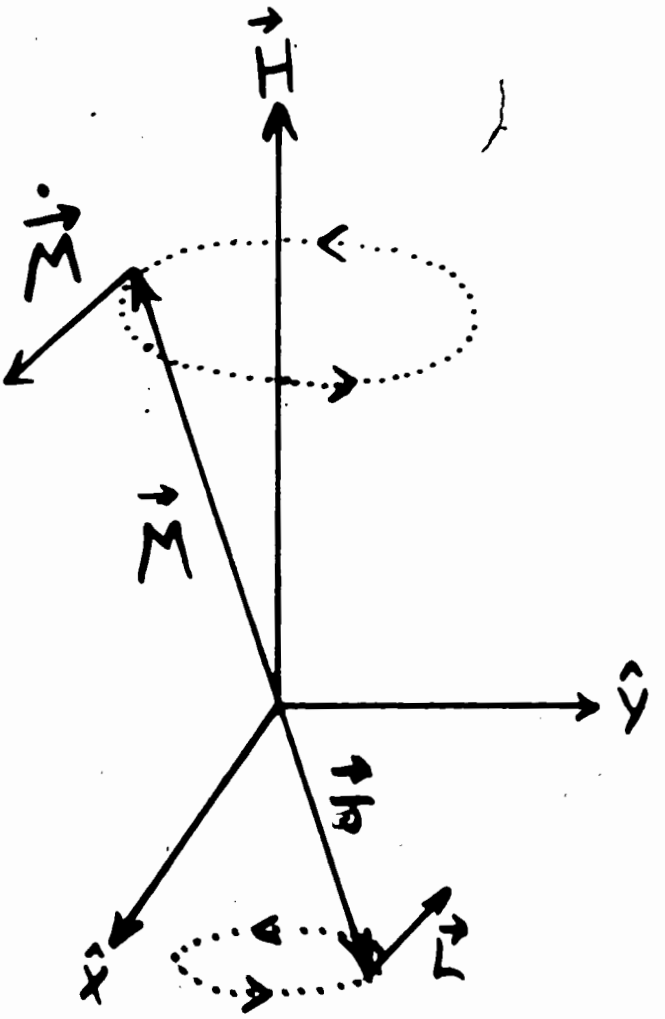

Fig. 2.1: Vector quantities entering Equations (2.6) and (2.7).

discussed further in Chapter 5.

In the absence of a detailed description of the magnetic relaxation, phenomenological damping terms were added to Equation (2.7). The first such damping term to be considered was introduced by Landau and Lifshitz in 1935. They proposed the following form of the damping:

$$\frac{-\lambda}{M_o^2} (\vec{M} \times (\vec{M} \times \vec{H})) \qquad (2.8a)$$

In this term M_o is the magnitude of the saturation magnetization and λ is a phenomenological constant with dimensions of sec^{-1}. Gilbert (1955) modified this term by replacing $\vec{M} \times \vec{H}$ with $d\vec{M}/dt$. The damping term then becomes

$$\frac{G}{\gamma M_o^2} (\vec{M} \times \frac{d\vec{M}}{dt}) \qquad (2.8b)$$

where G is the phenomenological damping constant. This form of damping causes the magnetization to relax toward its instantaneous equilibrium direction whereas the Landau-Lifshitz damping term causes the magnetization to relax towards the final equilibrium direction obtained when $d\vec{M}/dt = 0$. For small damping $\vec{M} \times \vec{H}$ and $d\vec{M}/dt$ are very nearly in the same direction and G and λ then have the same numerical values.

Bloembergen (1950) introduced the transverse relaxation approximation encountered in nuclear magnetic resonance as a possible relaxation term. This term has the form

$$- \frac{(\vec{M} - \vec{M}_o)_\perp}{\tau} \qquad (2.8c)$$

Here the subscript "$\perp$" indicates that only the component of $(\vec{M} - \vec{M}_o)$ which is perpendicular to $\vec{M}_o$ is considered. The damping is characterized by the decay time τ. The Bloembergen form of damping is basically different from the Landau-Lifshitz or Gilbert forms of damping in that the magnitude of $\vec{M}$ is not conserved, i.e. longitudinal relaxation is ignored. However, in the limit of light damping this difference is small and comparison of terms (2.8a) and (2.8c) in Equation (2.7) shows that $1/\tau \approx \lambda(\omega/\gamma M_o)$.

The effect of these phenomenological damping terms is illustrated in Fig. 2.2. These damping terms are not the only possible ones. However, almost all experiments involving reflection or transmission of microwaves from magnetic materials have been compared with calculations employing one of these damping terms. Diffusion of the magnetic carriers is an additional damping mechanism but experience shows that the effect of diffusion is quite small. (See Cochran et al. 1977a and References therein.)

The equation of motion for the magnetization developed thus far contains terms proportional to the torque on the magnetization due to an applied magnetic field $\vec{H}$. In a real material there eixst other sources of torque on the magnetization, for example anisotropy and shape demagnetization

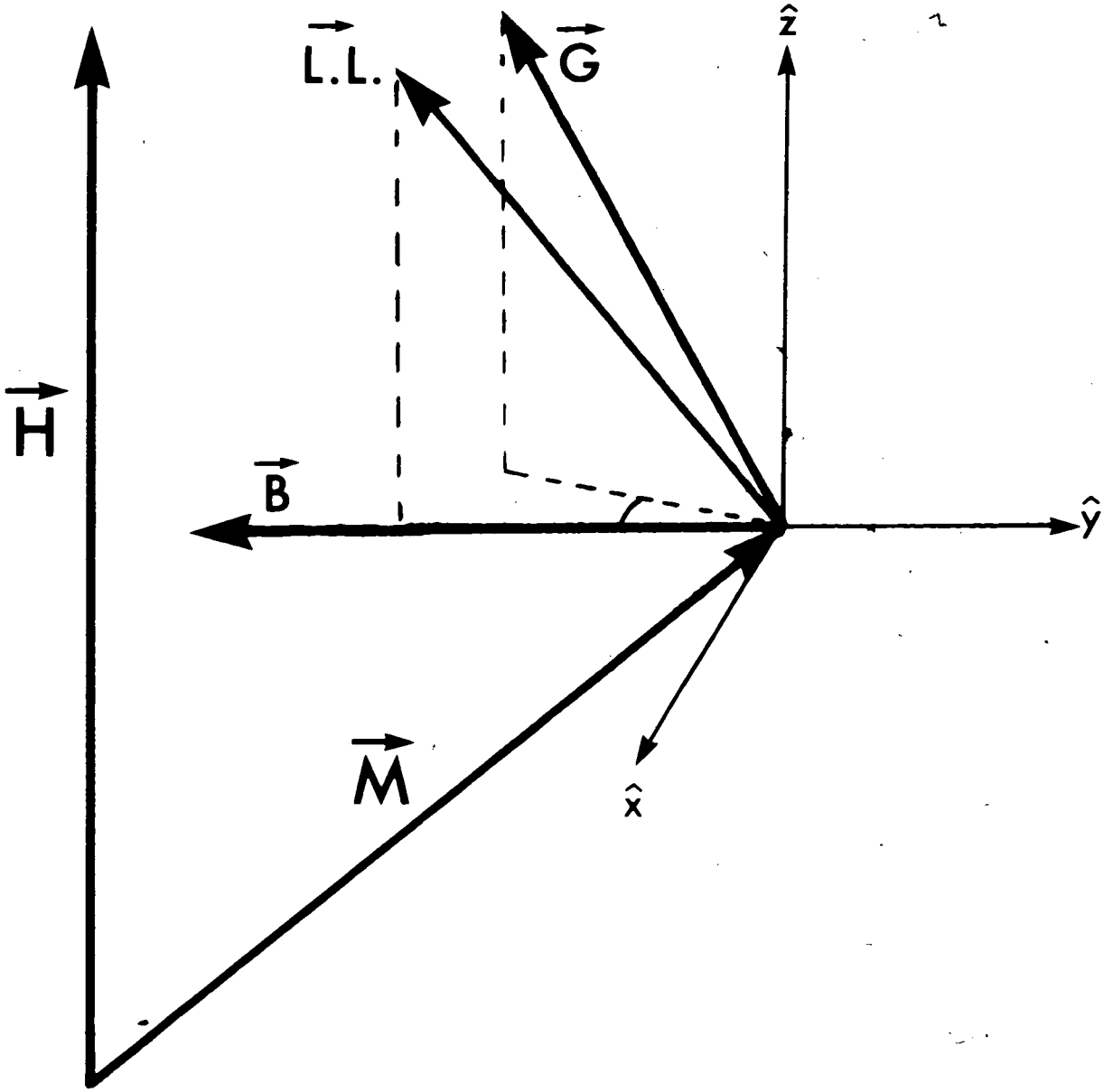

Fig. 2.2: Illustration of the direction of the Landau-Lifshitz ($\vec{L.L.}$), Gilbert ($\vec{G}$), and Bloembergen ($\vec{B}$) damping terms. $\vec{H}$ is parallel to the $\hat{Z}$-axis and $\vec{M}$ is in the $\hat{Y}$-$\hat{Z}$ plane.

effects, which enter into the equation of motion. These torques are conventionally expressed in terms of an effective demagnetizing field proportional to the magnetization (Macdonald 1951). These demagnetizing fields can be lumped in with the applied field (and the exchange field discussed below) to yield a net effective field acting on the magnetization. The equation of motion then becomes

$$\frac{d\vec{M}}{dt} = -\gamma(\vec{M} \times \vec{H}_{eff}) + \left\{ \begin{array}{l} \frac{-\lambda}{M_s^2}(\vec{M} \times \vec{M} \times \vec{H}_{eff}) \\ \frac{G}{\gamma M_s^2}(\vec{M} \times d\vec{M}/dt) \\ -\frac{(\vec{M} - \vec{M}_o)_\perp}{\tau} \end{array} \right\} \qquad (2.9)$$

where only one of the damping terms in parentheses is chosen. The effective field is written as:

$$\vec{H}_{eff} = \vec{H}_o + \vec{h} + \vec{H}_D + \vec{h}_D + \vec{h}_{exch} \qquad (2.10)$$

The first two terms on the right side of Equation (2.10), H_o and h, represent the total magnetic field applied to the magnetization. This applied field is separated into two parts for convenience: $\vec{H}_o$ is the static applied field and $\vec{h}$ is the magnetic field associated with the microwave radiation in the material. $\vec{H}_D$ is the static demagnetizing field proportional to the equilibrium magnetization, $\vec{M}_o$, i.e.

$$\vec{H}_D = -4\pi \bar{\bar{D}} \vec{M}_o \tag{2.11}$$

Similarly,

$$\vec{h}_D = -4\pi \bar{d} \vec{m} \tag{2.12}$$

where $\vec{m} = \vec{M} - \vec{M}_o$ (2.13)

The tensor demagnetizing factors $\bar{\bar{D}}$ and $\bar{d}$ are calculated explicitly for contributions due to sample shape, magnetocrystalline anisotropy, and magnetostriction in Appendix I.

The final term in Equation (2.10) is the exchange field. This field was first considered with reference to spin waves by Herring and Kittel (1951) and incorporated into the effective field by Ament and Rado (1955). The Coulomb exchange interaction which is responsible for maintaining ferromagnetism cannot exert a torque on the magnetization directly. (This large effective field is parallel to the magnetization.) However, a magnetization which is non-uniform in space will experience a transverse restoring force tending to produce a uniform magnetization. The first term in the Taylor expansion for the potential energy of the magnetization about its spatially uniform configuration is proportional to the second spatial derivative of $\vec{M}$. (The first derivative is zero because a spatially uniform magnetization is the minimum exchange energy configuration.)

One can also write this energy as the dot product of the magnetization and the exchange field h_{exch}, i.e.

$$\frac{1}{2}\vec{M}\cdot\vec{h}_{exch} \propto \frac{\nabla^2 M}{M_o} \qquad (2.14)$$

and introducing the exchange constant A as the constant of proportionality one obtains

$$\vec{h}_{exch} = \frac{2A\,\nabla^2\vec{M}}{M_o^{\,2}} \qquad (2.15)$$

This exchange field is introduced here for the sake of completeness. This field plays a small role in determining the microwave transmission and can safely be neglected. (See Cochran et al. 1977a and References therein.)

The purpose of this section is to obtain an expression for the microwave permeability. This can be done in a straightforward manner from Equation (2.9). For concreteness consider the co-ordinate system of Fig. 2.3. The $(\hat{X},\hat{Y},\hat{Z})$ co-ordinate system is the natural reference system to describe the geometry of the magnetic material. It is the laboratory co-ordinate system. The magnetic material is taken to be a slab of finite thickness with the Z axis normal to the slab. However, the (X', Y', Z') co-ordinate system of Fig. 2.3 is the natural reference system in which to describe the permeability. Since the magnitude of the magnetization is to a very good approximation independent of the microwave

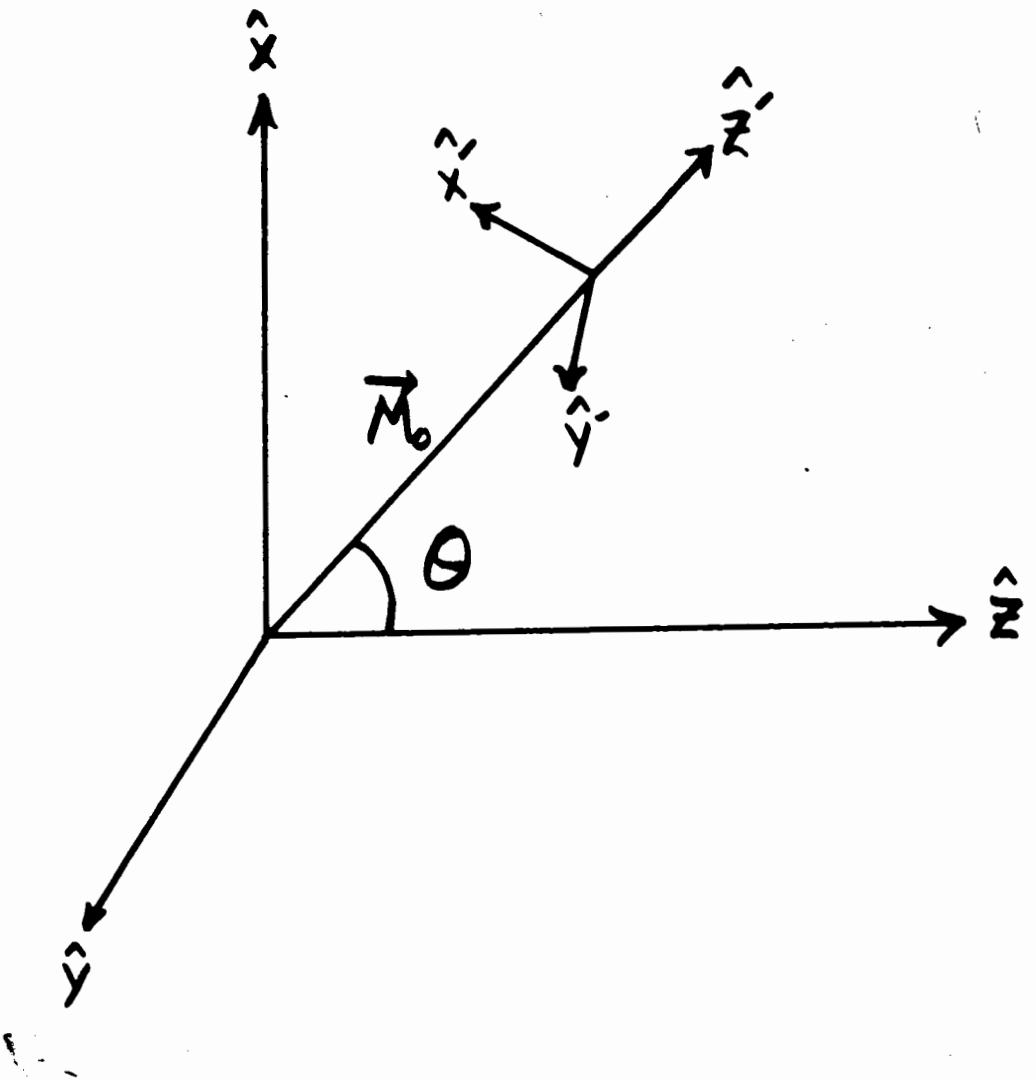

Fig. 2.3: Co-ordinate systems for the description of the sample orientation (unprimed) and for the equation of motion of the magnetization (primes).

field, then to first order the magnetization can only move perpendicular to $\vec{M}_o$. Thus in the co-ordinate system in which Z' is parallel to $\vec{M}_o$ the response of the magnetization to the microwave field is limited to the $\hat{X}'$-$\hat{Y}'$ plane. In general $\vec{M}_o$ is at some angle θ from the Z axis. It is convenient to orient the $\hat{X}'$-$\hat{Y}'$ axes so that X' is in the direction of increasing θ. Equation (2.9), for the choice of Landau-Lifshitz damping, can now be expressed as:

$$
\begin{aligned}
i\omega m_{X'} = & -\gamma\Big((H_{o_{Z'}} - 4\pi D_{Z',Z'} M_o) m_{Y'} \\
& - M_o\Big(h_{Y'} + \frac{2Ak^2}{M_o^2} m_{Y'} - 4\pi(d_{Y',X'} m_{X'} + d_{Y',Y'} m_{Y'})\Big) \\
& - \frac{\lambda}{M_o}\Big((H_{o_{Z'}} - 4\pi D_{Z',Z'} M_o) m_{X'} \\
& - M_o\Big(h_{X'} + \frac{2Ak^2}{M_o^2} m_{X'} - 4\pi(d_{X',X'} m_{X'} + d_{X',Y'} m_{Y'})\Big)\Big)
\end{aligned}
\tag{2.16a}
$$

$$
\begin{aligned}
i\omega m_{Y'} = & -\gamma\Big(-(H_{o_{Z'}} - 4\pi D_{Z',Z'} M_o) m_{X'} \\
& + M_o\Big(h_{X'} + \frac{2Ak^2}{M_o^2} m_{X'} - 4\pi(d_{X',X'} m_{X'} + d_{X',Y'} m_{Y'})\Big) \\
& - \frac{\lambda}{M_o}\Big((H_{o_{Z'}} - 4\pi D_{Z',Z'} M_o) m_{Y'} \\
& - M_o\Big(h_{Y'} + \frac{2Ak^2}{M_o^2} m_{Y'} - 4\pi(d_{Y',X'} m_{X'} + d_{Y',Y'} m_{Y'})\Big)\Big)
\end{aligned}
\tag{2.16b}
$$

and

$$i\omega m_{Z'} = 0 \tag{2.16c}$$

Several points concerning Equation (2.16) are in order. First, the quantities $\vec{m}$ and $\vec{h}$ are assumed to have wavelike time and space dependence, i.e. these quantities vary as $\exp(i\omega t - kZ)$ where k is a complex propagation constant to be determined. Second, $\vec{m}$ and $\vec{h}$ are small in magnitude compared to $\vec{M}$ and $\vec{H}_o$. In Equation (2.16) terms which are of second order in small quantities have been dropped. Thus Equation (2.16) is a linearized version of Equation (2.9). Third, in the limit $\vec{m} \rightarrow 0$, $\vec{h} \rightarrow 0$ the magnetization attains its equilibrium direction and there is no torque acting on the magnetization. This fact has been used to eliminate all terms in Equation (2.16) which are not proportional to $\vec{m}$ or $\vec{h}$.

Equation (2.16) is a relation between the radio frequency magnetization and magnetic field. After some manipulation this equation can be brought into the form

$$\vec{m} = \overline{\overline{\chi}}\, \vec{h} \tag{2.17}$$

and the permeability we wish to find is then

$$\overline{\overline{\mu}} = \overline{\overline{I}} + 4\pi\, \overline{\overline{\chi}}. \tag{2.18}$$

where $\bar{\bar{I}}$ is the unit tensor. Derivation of Equation (2.18) fulfills the purpose of this section. Explicit expressions for the elements of the permeability tensor are given in Appendix II.

2.4a Maxwell's Equations and Propagation Constant: Perpendicular Configuration

The permeability developed in the previous section merely relates the magnetic induction $\vec{b}$ to the magnetic field $\vec{h}$. Maxwell's equations impose further conditions on these quantities. In order to simplify the solution for the waves inside a ferromagnetic metal, two specific but important special cases will be considered. Here the case in which the applied magnetic field is perpendicular to the plane of an infinite slab ($\theta = 0°$ in Fig. 2.3) is discussed. This is known as the perpendicular configuration. In the next section the case in which the magnetic field is applied in the plane of the slab ($\theta = 90°$) is discussed.

The solutions of Maxwell's equations for the perpendicular configuration are most simply described using circularly polarized waves. The transformation from the $(\hat{X},\hat{Y},\hat{Z})$ co-ordinate system of Fig. 2.3 is accomplished by the matrix

$$\bar{\bar{R}} = \begin{pmatrix} \frac{1}{\sqrt{2}} & \frac{i}{\sqrt{2}} & 0 \\ \frac{1}{\sqrt{2}} & -\frac{i}{\sqrt{2}} & 0 \\ 0 & 0 & 1 \end{pmatrix} \qquad (2.19)$$

Of course the inverse of $\overline{\overline{R}}$ is simply its transposed complex conjugate $\overline{\overline{R}}^{+}$. To simplify matters further, only waves travelling in the Z direction will be considered[2]. Maxwell's equations can then be explicitly written as:

$$\nabla \cdot \vec{e} = \frac{\partial e_Z}{\partial Z} = 0 \qquad (2.20a)$$

$$\nabla \cdot \vec{b} = \frac{\partial b_Z}{\partial Z} = 0 \qquad (2.20b)$$

$$\nabla \times \vec{e} = \begin{pmatrix} \frac{\partial}{\partial Z} e_+ \\ \frac{\partial}{\partial Z} e_- \\ 0 \end{pmatrix} = \begin{pmatrix} + \frac{i}{c} \frac{\partial}{\partial t} b_+ \\ - \frac{i}{c} \frac{\partial}{\partial t} b_- \\ 0 \end{pmatrix} \qquad (2.20c)$$

$$\nabla \times \vec{h} = \begin{pmatrix} \frac{\partial}{\partial Z} h_+ \\ \frac{\partial}{\partial Z} h_- \\ 0 \end{pmatrix} = \begin{pmatrix} - \frac{4\pi\sigma i}{c} e_+ \\ + \frac{4\pi\sigma i}{c} e_- \\ 0 \end{pmatrix} \qquad (2.20d)$$

The permeability can also be straightforwardly expressed in circularly polarized co-ordinates. Starting with the usual relation between b and h, namely

---

[2]This is not a particularly restrictive condition. The index of refraction for a metal is so large ($\sim 10^4$) that microwaves are refracted normal to the surface no matter what the angle of incidence is.

$$\vec{b} = \overline{\overline{\mu}}\,\vec{h} \tag{2.21}$$

and by applying the matrix $\overline{\overline{R}}$, then

$$\vec{b}_c = \overline{\overline{R}}\,\overline{\overline{\mu}}\,\vec{h} = \overline{\overline{R}}\,\overline{\overline{\mu}}\,\overline{\overline{R}}^{+}\,\vec{h}_c$$

or

$$\overline{\overline{\mu}}_c = \overline{\overline{R}}\,\overline{\overline{\mu}}\,\overline{\overline{R}}^{+} \tag{2.22}$$

where the subscript "c" indicates a circularly polarized basis. Explicitly

$$\overline{\overline{\mu}}_c = \begin{pmatrix} \mu_+ & 0 & 0 \\ 0 & \mu_- & 0 \\ 0 & 0 & \mu_{ZZ} \end{pmatrix} \tag{2.23}$$

This diagonalized permeability can be used in Equation (2.20c) to eliminate $\vec{b}$. Remembering that the solutions go like $\exp[i\omega t - kZ]$, where k is the propagation constant, then Equations (2.20c) and (2.20d) reduce to

$$k_{\pm}^2 = \frac{+4\pi\omega\sigma\, i}{c^2}\,\mu_{\pm} \tag{2.24}$$

In summary, Maxwell's equations and the equation of motion, i.e. Equations (2.20) and (2.21), constitute two independent systems of linear algebraic equations, one set positively polarized and one set negatively polarized. The requirement that these equations have nonzero solutions results in a dispersion relation, Equation (2.24), which determines the propagation constants of the waves inside a magnetic metal.

Insight into the nature of the solutions above can be gained by studying the permeability in Equation (2.24). Neglecting magnetocrystalline anisotropy and magnetostriction and remembering that we are also ignoring exchange, then Equation (2.18) yields:

$$\mu_+ = \frac{\frac{\omega}{\gamma} - H_o\left(1 + \frac{i\lambda}{\gamma M_o}\right)}{\frac{\omega}{\gamma} - (H_o - 4\pi M_o)\left(1 + \frac{i\lambda}{\gamma M_o}\right)} \qquad (2.25a)$$

$$\mu_- = \frac{\frac{\omega}{\gamma} + H_o\left(1 - \frac{i\lambda}{\gamma M_o}\right)}{\frac{\omega}{\gamma} + (H_o - 4\pi M_o)\left(1 - \frac{i\lambda}{\gamma M_o}\right)} \qquad (2.25b)$$

and

$$\mu_{zz} = 1 \qquad (2.25c)$$

This permeability has two special values of applied magnetic field associated with it. First, if

$$H_o = \frac{\omega}{\gamma} + 4\pi M_o \qquad (2.26)$$

then

$$\mu_+ = \frac{4\pi M_o + \frac{i\lambda}{\gamma M_o}\left(4\pi M_o + \frac{\omega}{\gamma}\right)}{\left(\frac{\omega}{\gamma}\right)\left(\frac{i\lambda}{\gamma M_o}\right)} \qquad (2.27a)$$

and

$$\mu_- = \frac{\frac{\omega}{\gamma}\left(2 - \frac{i\lambda}{\gamma M_o}\right) + 4\pi M_o\left(1 - \frac{i\lambda}{\gamma M_o}\right)}{\left(\frac{\omega}{\gamma}\right)\left(2 - \frac{i\lambda}{\gamma M_o}\right)} \qquad (2.27b)$$

In the limit of small damping $\mu_+ \to \infty$ whereas $\mu_- \to 1 + \frac{2\pi M_o}{\frac{\omega}{\gamma}}$.

Thus the positively polarized wave has a large value for its permeability and Equation (2.24) shows that this wave is heavily attenuated. This is known as ferromagnetic resonance (FMR). Note that positive circular polarization corresponds to an R.F. field with the same sense of precession as the magnetization about an external magnetic field.

Second, if

$$H_o = \frac{\omega}{\gamma} \qquad (2.28)$$

then

$$\mu_+ = \frac{-\frac{i\lambda}{\gamma M_o}}{\frac{4\pi M_o}{\omega/\gamma}\left(1 + \frac{i\lambda}{\gamma M_o}\right) - \frac{i\lambda}{\gamma M_o}} \qquad (2.29a)$$

and

$$\mu_- = \frac{2 - \frac{i\lambda}{\gamma M_o}}{2 - \frac{i\lambda}{\gamma M_o} - \frac{4\pi M_o}{\omega/\gamma}\left(1 - \frac{i\lambda}{\gamma M_o}\right)} \qquad (2.29b)$$

In the limit of small damping $\mu_+ \to 0$ whereas $\mu_- \to \frac{2}{2 - \frac{4\pi M_o}{\omega/\gamma}}$.

This shows that the k_+ in Equation (2.24) is small for this value of applied field and the wave is only lightly attenuated. Hence, there is the potential for the wave to penetrate through a moderately thick slab of magnetic metal. This is called ferromagnetic antiresonance (FMAR). The complete expression for μ_+ is plotted as a function of magnetic field in Fig. 2.4.

2.4b Maxwell's Equations and Propagation Constants: Parallel Configuration

The geometry considered in this section is such that the magnetic field and magnetization are parallel to the $\hat{X}$-axis of Fig. 2.3. This changes the solution to Maxwell's equations obtained in the previous section in two ways. First, the shape demagnetization factor which enters Equation (2.16) is $D_{Z'Z'} = D_{XX} = 0$ whereas this term was 1 in the perpendicular configuration. Second, the Maxwell equation $\nabla \cdot \vec{b} = 0$ is not simply satisfied by $b_Z = h_Z = 0$ as in the perpendicular configuration. Here $b_Z = 0$ but $h_Z = -4\pi M_Z \neq 0$. This can be seen by noting that if the magnetization is perturbed from equilibrium it tends to precess about the $\hat{X}$-axis with $M_Z \neq 0$. The conventional approach to guarantee that the permeability always yields $b_Z = \mu_{ZX} h_X + \mu_{ZY} h_Y + \mu_{ZZ} h_Z = 0$ is to substitute $h_Z = -4\pi M_Z$ into Equation (2.16). Then the permeability becomes

Fig. 2.4: The real (R) and imaginary (I) parts of the permeability μ_+. The scale shown here is in arbitrary units (1 unit equals a permeability of 5.758). Parameters used in the calculation were: R.F. frequency = 24.00 GHz, g = 2.187, M_o = 486 G, and $\lambda = 2.45 \times 10^8 sec^{-1}$.

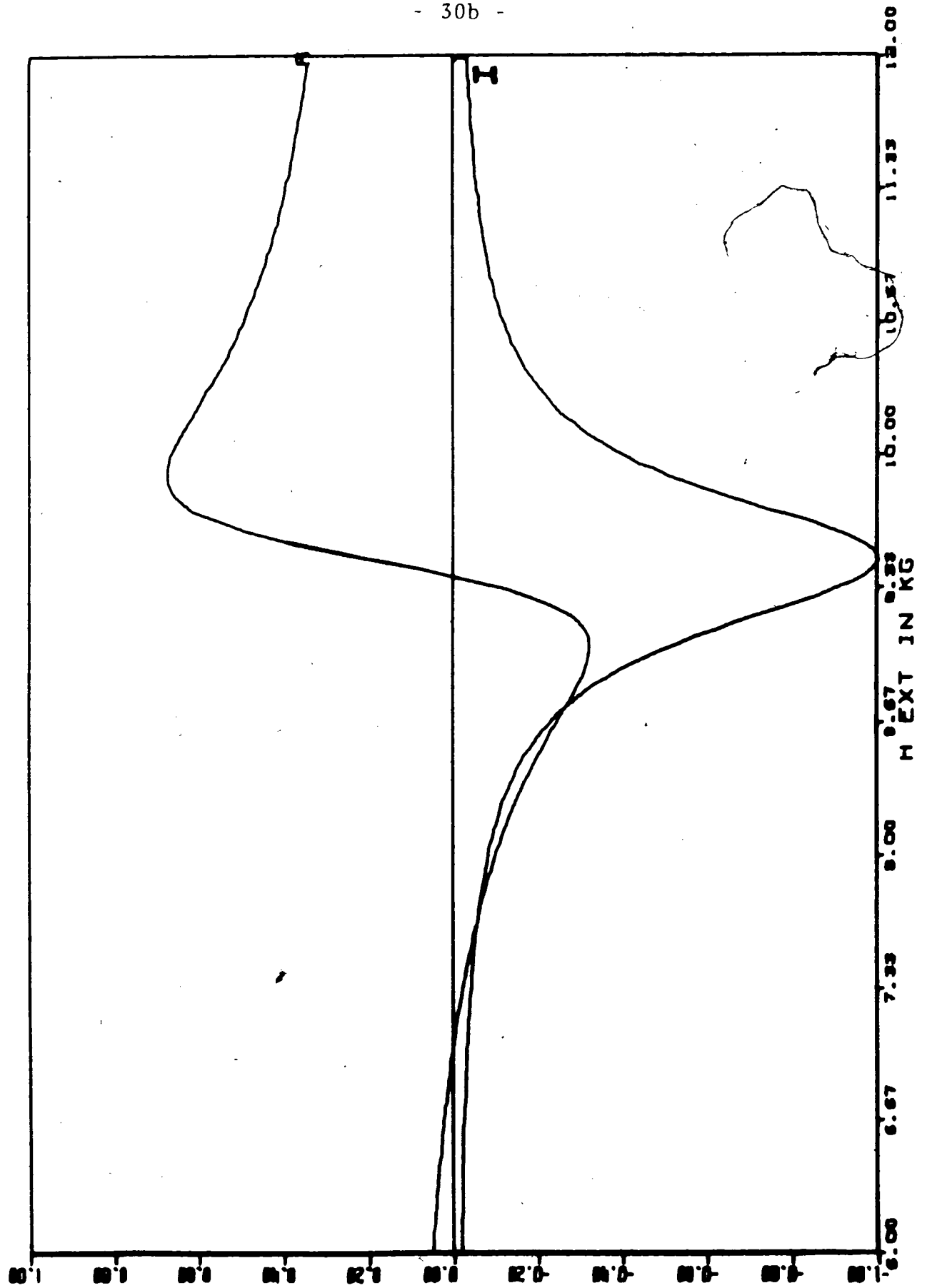

Fig. 2.4

$$\overline{\overline{\mu}} = \begin{pmatrix} 1 & 0 & 0 \\ 0 & \mu_{YY} & 0 \\ 0 & \mu_{ZY} & 1 \end{pmatrix} \qquad (2.30)$$

where

$$\mu_{YY} = \frac{(H_o+4\pi M_o)^2\left[1+\left(\frac{\lambda}{\gamma M_o}\right)^2\right]-\left(\frac{\omega}{\gamma}\right)^2+2\,\frac{i\lambda}{\gamma M_o}\,\frac{\omega}{\gamma}\,(H_o+4\pi M_o)}{H_o(H_o+4\pi M_o)\left[1+\left(\frac{\lambda}{\gamma M_o}\right)^2\right]-\left(\frac{\omega}{\gamma}\right)^2+\frac{i\lambda}{\gamma M_o}\,\frac{\omega}{\gamma}\,(2H_o+4\pi M_o)} \qquad (2.31a)$$

and

$$\mu_{ZY} = \frac{H_o(H_o+4\pi M_o)\left[1+\left(\frac{\lambda}{\gamma M_o}\right)^2\right]-\left(\frac{\omega}{\gamma}\right)^2+\frac{i\lambda}{\gamma M_o}\,\frac{\omega}{\gamma}\,(2H_o+4\pi M_o)-i\,\frac{\omega}{\gamma}\,4\pi M_o}{H_o(H_o+4\pi M_o)\left[1+\left(\frac{\lambda}{\gamma M_o}\right)^2\right]-\left(\frac{\omega}{\gamma}\right)^2+\frac{i\lambda}{\gamma M_o}\,\frac{\omega}{\gamma}\,(2H_o+4\pi M_o)} \qquad (2.31b)$$

Only two of Maxwell's equations remain to be satisfied, i.e.

$$\nabla \times \vec{e} = \begin{pmatrix} -\frac{\partial e_Y}{\partial Z} \\ +\frac{\partial e_X}{\partial Z} \\ 0 \end{pmatrix} = \frac{-1}{c} \begin{pmatrix} \frac{\partial h_X}{\partial t} \\ \mu_{YY} \frac{\partial h_Y}{\partial t} \\ 0 \end{pmatrix} \qquad (2.32a)$$

$$\nabla \times \vec{h} = \begin{pmatrix} -\frac{\partial h_Y}{\partial Z} \\ +\frac{\partial h_X}{\partial Z} \\ 0 \end{pmatrix} = \frac{4\pi\sigma}{c} \begin{pmatrix} e_X \\ e_Y \\ 0 \end{pmatrix} \qquad (2.32b)$$

Operating on the time and space dependence $\exp[i\omega t - kZ]$, Equation (2.32) reduces to

$$k^2 = i \frac{4\pi\omega\sigma}{c^2} \qquad (2.33a)$$

and

$$k^2 = i \frac{4\pi\omega\sigma}{c^2} \mu_{YY} \qquad (2.33b)$$

As with the perpendicular configuration there are two propagation constants. The uninteresting value of k (Equation (2.33a)) corresponds to a linearly polarized wave with $\vec{h}_{RF} \| \vec{M}_o$. This wave is the same as one would find in a nonmagnetic metal. The second propagation constant

(Equation (2.33b)) corresponds to a wave with $\vec{h}_{RF} \perp \vec{M}_o$. This propagation constant is modulated by μ_{YY}. The phenomena of ferromagnetic resonance and ferromagnetic antiresonance can be seen to exist for the parallel configuration by noting that $\mu_{YY} \to \infty$ as $\lambda \to 0$ for an applied magnetic field which satisfies

$$\frac{\omega}{\gamma} = [(H_o)(H_o + 4\pi M_o)]^{1/2} \tag{2.34}$$

and that $\mu_{YY} \to 0$ as $\lambda \to 0$ for

$$H_o = \omega/\gamma - 4\pi M_o. \tag{2.35}$$

The magnetic field values at which FMR and FMAR occur for the parallel configuration are different from the perpendicular configuration. This difference can be exploited to measure M_o. Otherwise, these two configurations are quite similar.

2.5a The Boundary Value Problem: Perpendicular Configuration

The expressions for the propagation constants developed thus far remain to be incorporated into an explicit calculation of the microwave transmission through a slab of magnetic metal. Here the perpendicular configuration is dealt with. The waves we are concerned with are schematically indicated in Fig. 2.5. A circularly polarized wave in free space of amplitude e_o, h_o is normally incident on the slab. A wave of amplitude e_R, h_R is reflected and a wave of amplitude e_F, h_F propagates into the slab. At the back of the slab some radiation of amplitude

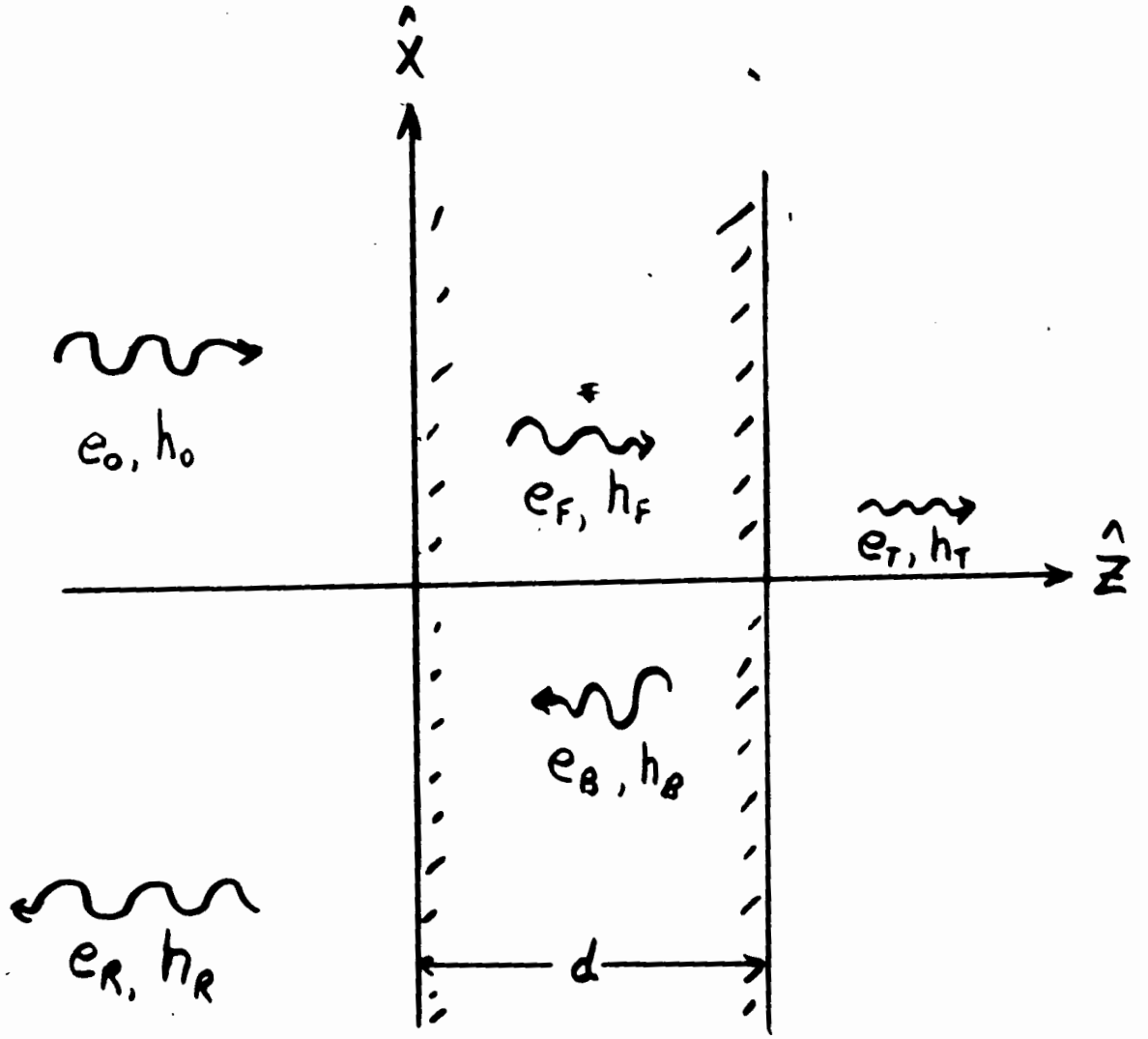

Fig. 2.5: Schematic of waves involved in the boundary value problem. The waves are either circularly polarized (perpendicular configuration) or linearly polarized (parallel configuration).

e_B, h_B is internally reflected. Subscripts referring to positive or negative polarization have been supressed since all the waves are of the same polarization. The amplitudes of these waves can be determined by requiring that tangential $\vec{h}$ and tangential $\vec{e}$ be continuous at each surface of the slab. At the front surface we have

$$h_o + h_R = h_F + h_B \exp(-kd) \tag{2.36a}$$

$$e_o + e_R = e_F + e_B \exp(-kd) \tag{2.36b}$$

and at the back surface

$$h_F \exp(-kd) + h_B = h_T \tag{2.36c}$$

$$e_F \exp(-kd) + e_B = e_T \tag{2.36d}$$

The electric fields are eliminated from these equations by noting that Equation (2.20d) may be rewritten as

$$e_+ = - \frac{i\omega\delta^2 k_+}{c} h_+ \tag{2.37a}$$

and

$$e_- = + \frac{i\omega\delta^2 k_-}{c} h_- \tag{2.37b}$$

where

$$\delta^2 = \frac{c^2}{4\pi\omega\sigma} \tag{2.38}$$

Similarly, in free space where the waves have the harmonic

dependence $\exp[i\omega t - \frac{i\omega}{c} z]$,

$$e_+ = -i\, h_+ \tag{2.39a}$$

and

$$e_- = +i\, h_- \tag{2.39b}$$

Expressions (2.37) and (2.39) apply to forward propagating waves; for backward propagating waves the terms on the right in Equations (2.37) and (2.39) must be multiplied by -1. After the electric fields are eliminated from Equation (2.36) this system of four algebraic equations can be solved for the transmitted wave in terms of the incident wave, i.e.

$$\frac{h_T}{h_o} = \frac{4\,\frac{\omega k \delta^2}{c}}{(1 + \frac{\omega k \delta^2}{c})^2\, e^{kd} - (1 - \frac{\omega k \delta^2}{c})^2\, e^{-kd}} \tag{2.40}$$

Equation (2.40) is true for both polarizations separately. This equation constitutes the solution to the boundary value problem in the perpendicular configuration. It is apparent that all one need do to calculate the transmitted signal is feed the material parameters into Equation (2.25) to calculate $\mu_\pm$ and hence obtain $k_\pm$ from Equation (2.24). All the information about the magnetic properties of the material is contained in $k_\pm$. Substitution of $k_\pm$ into Equation (2.40) immediately yields the desired transmission amplitude.

2.5b The Boundary Value Problem: Parallel Configuration

The solution to the boundary value problem in the parallel configuration proceeds in the same manner as for the perpendicular configuration. Since the linearly polarized wave with $\vec{h}_{RF} \| \vec{M}_o$ does not contain any information about the magnetic system, only incident radiation with $\vec{h}_{RF} \perp \vec{M}_o$ will be discussed here. Fig. 2.5 illustrates the boundary value problem. An incident wave of amplitude e_o, h_o gives rise to a reflected wave e_R, h_R and a transmitted wave e_F, h_F at the front surface of the slab. At the back surface of the slab the forward propagating wave is partly reflected to form a backward propagating wave of amplitude e_B, h_B and partly transmitted to form the transmitted wave of amplitude e_T, h_T. Continuity of $\vec{e}$ and $\vec{h}$ at the front and back surfaces require that

$$h_o + h_R = h_F + h_B \exp(-kd) \tag{2.41a}$$

$$e_o + e_R = e_F + e_B \exp(-kd) \tag{2.41b}$$

$$h_F \exp(-kd) + h_B = h_T \tag{2.41c}$$

$$e_F \exp(-kd) + e_B = e_T \tag{2.41d}$$

Here the h's are all polarized along the $\hat{Y}$-axis and the e's are polarized along the $\hat{X}$-axis. The electric fields inside the metal may be eliminated by rewriting Equation (2.32b) as

$$e_X = \frac{i\omega}{c} k \delta^2 h_Y \tag{2.42a}$$

and

$$e_X = - \frac{\omega}{c} k \delta^2 h_Y \qquad (2.42b)$$

for backward propagating waves. Of course, in free space we have

$$e_X = h_Y \qquad (2.43a)$$

for forward propagating waves and

$$e_X = -h_Y \qquad (2.43b)$$

for backward propagating waves. Solution of Equation (2.41) for the transmitted wave then yields:

$$\frac{h_T}{h_o} = \frac{4 \frac{\omega k \delta^2}{c}}{(1 + \frac{\omega k \delta^2}{c})^2 e^{kd} - (1 - \frac{\omega k \delta^2}{c})^2 e^{-kd}} \qquad (2.44)$$

This equation is formally identical to Equation (2.40). This constitutes the solution to the boundary value problem in the parallel configuration.

2.6 Example Calculations

The material presented in this chapter is meant to indicate precisely what is involved in calculating a plot of transmitted microwave signal vs. magnetic field. Thus far the prescription for the calculation (neglecting exchange) has been given.

Ultimately these calculations are compared with experimental data and the parameters describing the material are adjusted within the calculations to obtain the best agreement with the experimental data. This procedure is most useful if each parameter of interest affects the calculation in a manner relatively independent of all other parameters. In this section the effect of various parameters on the calculations is illustrated.

The material parameters entering into the calculation are:

1) Magnetization.
2) Spectroscopic splitting factor (g-factor).
3) Magnetic damping.
4) Shape demagnetization factors.
5) Conductivity.
6) Sample thickness.
7) Anisotropy (magnetocrystalline and magnetostrictive).
8) Exchange constant and exchange boundary conditions (Appendix III).

The set of figures which follow are typical of nickel at 200°C. The specific parameters used in the following figures are listed in Table 2.1.

Figure 2.6 shows how the lineshape of the transmitted amplitude vs. magnetic field varies with different values of the Landau-Lifshitz damping parameter and g-factor. The calculations were made for the case in which the magnetization is perpendicular to the plane of the slab. Curves a, b and

Table 2.1

Parameters used for calculations shown in Fig. 2.6 to 2.9, unless otherwise stated. The material parameters correspond to nickel at 200°C.

f	R.F. frequency	24.000 GHz
g	g-factor	2.187
M_o	magnetization	399 gauss
ρ	resistivity	16.5×10^{-6} Ω-cm
(σ)	(conductivity)	($5.36 \times 10^{16} sec^{-1}$)
d	thickness	2.0×10^{-3} cm
λ	damping	$2.45 \times 10^{8} sec^{-1}$

c were calculated using $\lambda = 2.4 \times 10^8 sec^{-1}$, $g = 2.19$; $\lambda = 2.5 \times 10^8 sec^{-1}$, $g = 2.19$; and $\lambda = 2.4 \times 10^8 sec^{-1}$, $g = 2.20$. The peak transmission amplitude for each curve has been normalized to 1.0. Identical curves could have been produced using either the Gilbert or Bloembergen form of damping. The damping clearly dominates the linewidth and the g-factor determines the position of the peak transmission. However, the damping does have a small effect on the position of the peak transmission (see curves a and b). Although it is not indicated in Fig. 2.6, the fact that the shape demagnetization factor is $D_{ZZ} < 1$ for a finite sample also alters the peak position slightly.

The magnetization has only a weak effect on the transmission lineshape of Fig. 2.6. However, if the magnetization is in the plane of the slab and linearly polarized radition is incident such that $\vec{h} \perp \vec{M}_o$, then the position of the peak transmission is drastically altered. As shown previously, FMAR occurs for the parallel configuration at an applied field $H_o \approx \omega/\gamma - 4\pi M_o$. (The approximation sign is used here because $D_{XX} \neq 0$ for a finite sample and this changes the condition described by Equation (2.35) by introducing the demagnetization field $4\pi D_{XX} M_o$.) Transmission amplitude vs. applied magnetic field calculations for both the parallel and perpendicular configurations are shown in Fig. 2.7. Curves a and b are for the parallel configuration and curves c and d are for the perpendicular configuration. The separation between these two sets of curves is proportional to the magnetization.

Fig. 2.6: Transmitted amplitude vs. magnetic field showing the effect of different g-factors and damping parameters.
Curve (a): $\lambda = 2.4 \times 10^{8} sec^{-1}$, $g = 2.19$;
Curve (b) $\lambda = 2.5 \times 10^{8} sec^{-1}$, $g = 2.19$; and
Curve (c) $\lambda = 2.4 \times 10^{8} sec^{-1}$, $g = 2.20$.
In all cases the magnetic field is perpendicular to the plane of the slab. Other parameters used were: $f = 24.000$ GHz, $M_o = 399$ G, $\sigma = 5.36 \times 10^{16} sec^{-1}$, and $d = 20\mu m$.

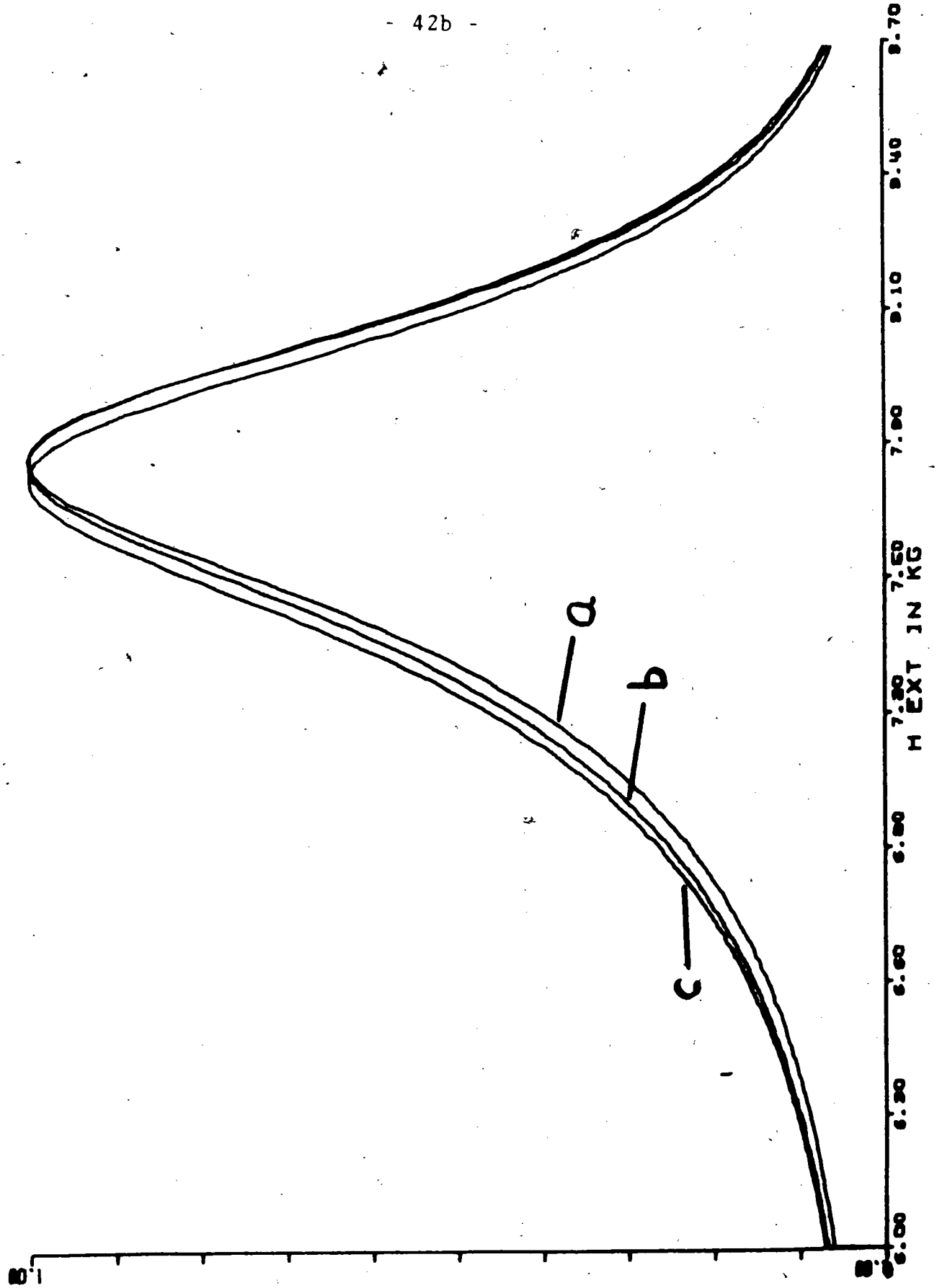
a
b
c
H EXT IN KG

Thus far the effect of the g-factor, magnetization, and magnetic damping have been shown to determine the lineshape and position of the transmitted signal. The other parameters used in the calculation can minic the effect of these parameters somewhat. Figure 2.7 shows the effect of the slab thickness and/or conductivity on the transmission lineshape. Both of these parameters enter the calculation through the term exp[-kd] where $k \propto \frac{1}{\delta} \propto \sqrt{\sigma}$ and, hence, both parameters have an identical effect on the calculated transmission. Curves a and b of Fig. 2.7 are calculated for a thickness of 20μ and 18μ, respectively, and curves c and d are calculated for a conductivity of $5.36 \times 10^{16} sec^{-1}$ and $4.47 \times 10^{16} sec^{-1}$. One can see that the broadening of the transmission lineshape with decreased thickness or conductivity is more symmetric than the broadening introduced by the damping parameter (Fig. 2.6). This is more easily discerned if the plot of the amplitude vs. phase of the transmitted signal, i.e. the locus plot, is concerned. In Fig. 2.8 two different pairs of damping and thickness were used to calculate locus plots. The parameters were chosen such that the usual graphs of transmitted amplitude vs. magnetic field were identical to within three thicknesses of the lines used to draw these figures. The difference between these two sets of parameters is quite apparent in the locus plot in Fig. 2.8.

Magnetocrystalline anisotropy and magnetostriction enter the calculation through the radio frequency demagnetization

Fig. 2.7: Transmitted amplitude vs. magnetic field for the parallel (curves (a) and (b)) and perpendicular (curves (c) and (d)) configurations. Parameters used were: (a) d = 20 μm, $\lambda = 5.36 \times 10^{16} sec^{-1}$; (b) d = 18 μm, $\lambda = 5.36 \times 10^{16} sec^{-1}$; (c) d = 20 μm, $\lambda = 5.36 \times 10^{16} sec^{-1}$; (d) d = 20μm, $\lambda = 4.47 \times 10^{16} sec^{-1}$. Also, see Table 2.1. Parameters common to all curves were f = 24.000 GHz, g = 2.187, M_o = 399 G, and $\lambda = 2.45 \times 10^{8} sec^{-1}$.

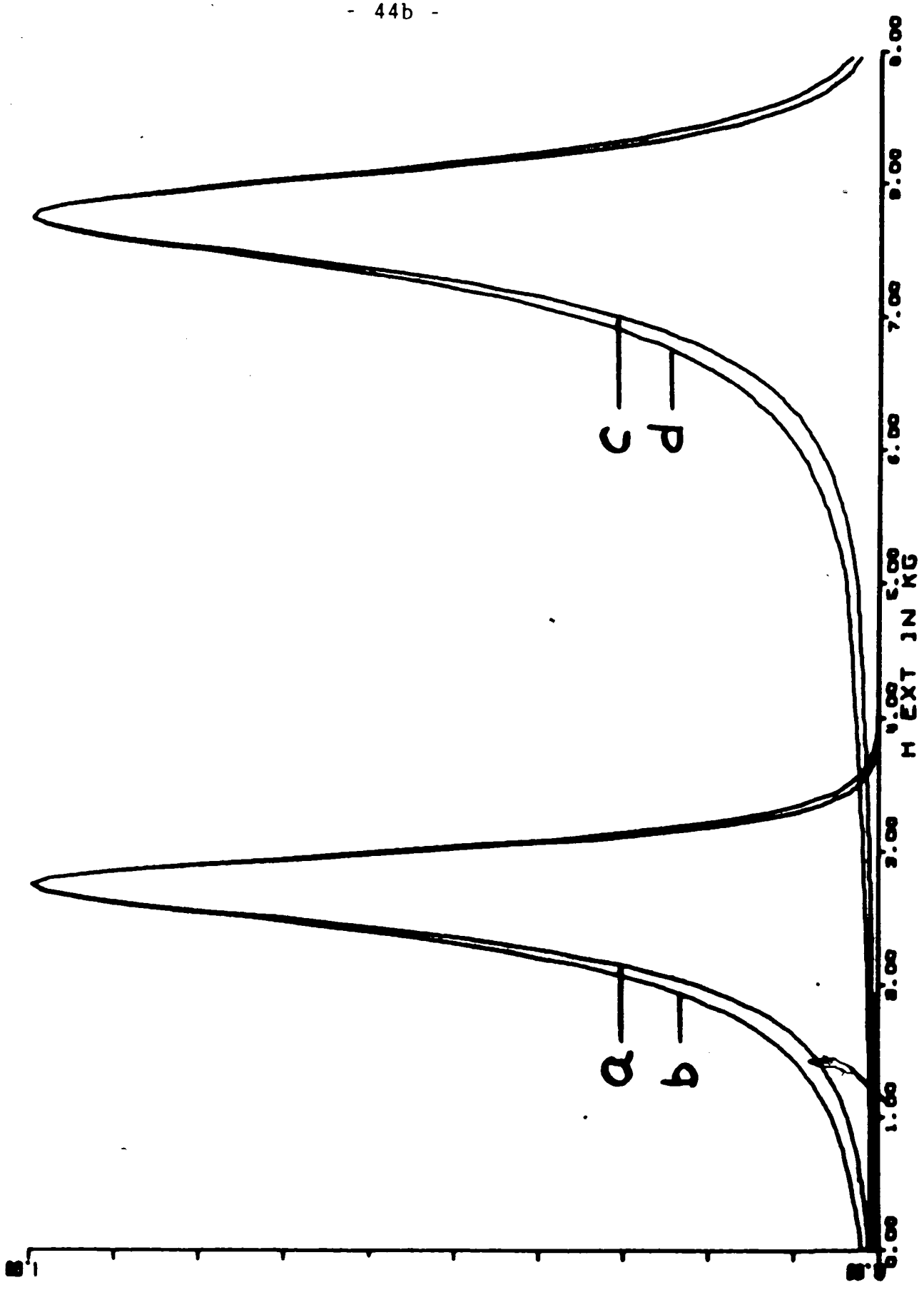
c
d
a
b
H EXT IN KG

Fig. 2.8: Calculated amplitude vs. phase of transmitted signal in the perpendicular configuration for two thickness-damping combinations. In the calculation for curve (a) $d = 20\mu m$ and $\lambda = 2.4 \times 10^{8} sec^{-1}$; for curve (b) $d = 18\mu m$ and $\lambda = 1.9 \times 10^{8} sec^{-1}$. Other parameters used were: $f = 24.000$ GHz, $g = 2.187$, $M_o = 399$ G, and $\lambda = 5.36 \times 10^{16} sec^{-1}$.

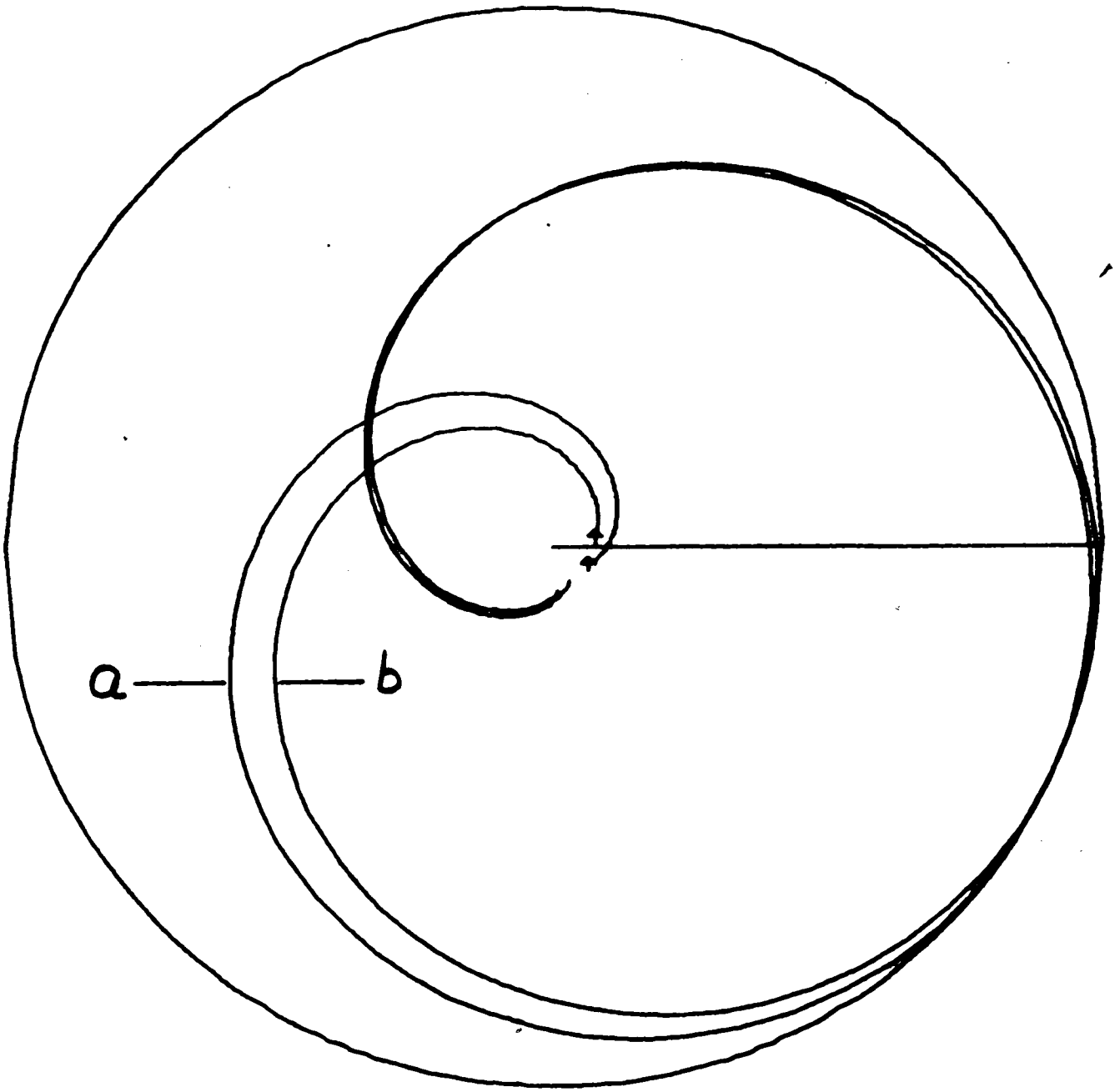
a
b

factors as well as through the static demagnetization factors (Appendix I). These demagnetization factors shift the transmission line position and slightly alter the lineshape. This is shown in Fig. 2.9 for the case of a material of negative magnetostrictive constant in a state of uniform, planar tension. Curves a and b are calculated for the perpendicular configuration; curves c and d are calculated for the parallel configuration. Nonzero magnetostrictive demagnetization factors have been used to calculated curves b and d. Note that the effect of the stress is to shift the transmission lines in a different manner and even to alter the peak amplitude for one configuration. Similar shifts and amplitude changes are associated with magnetocrystalline anisotropy.

The effect of exchange is so small that it is not illustrated here. Changing the exchange constant A by an order of magnitude (1.0×10^{-6} erg/cm to 1.0×10^{-5} erg/cm) and specifying any boundary condition on the radiofrequency magnetization at the sample surface (node, antinode, and anything in between) produces a change in the transmitted signal of less than the thickness of the lines used to draw the figures in this section.

The calculations presented here illustrate the information available from measurements of microwave transmission vs. magnetic field. In particular, the position and width of the transmission peak in the perpendicular configuration determine the g-factor and the damping parameter; the separation between the peaks in the parallel and perpendicular configurations

Fig. 2.9: Transmitted amplitude vs. applied magnetic field illustrating the effect of magnetostriction. Curves (a) and (b) are for the perpendicular configuration, curves (c) and (d) are for the parallel configuration. A magnetostrictive R.F. demagnetization factor of $\frac{3\lambda_s\sigma}{4\pi M_o^2}$ = 3.97×10^{-2} has been used in calculating curves (b) and (d). Other parameters used in the calculation were: f = 24.000 GHz, g = 2.187, M_o = 399 G, σ = $5.36 \times 10^{16} sec^{-1}$, d = 20μm, and λ = $2.45 \times 10^{8} sec^{-1}$.

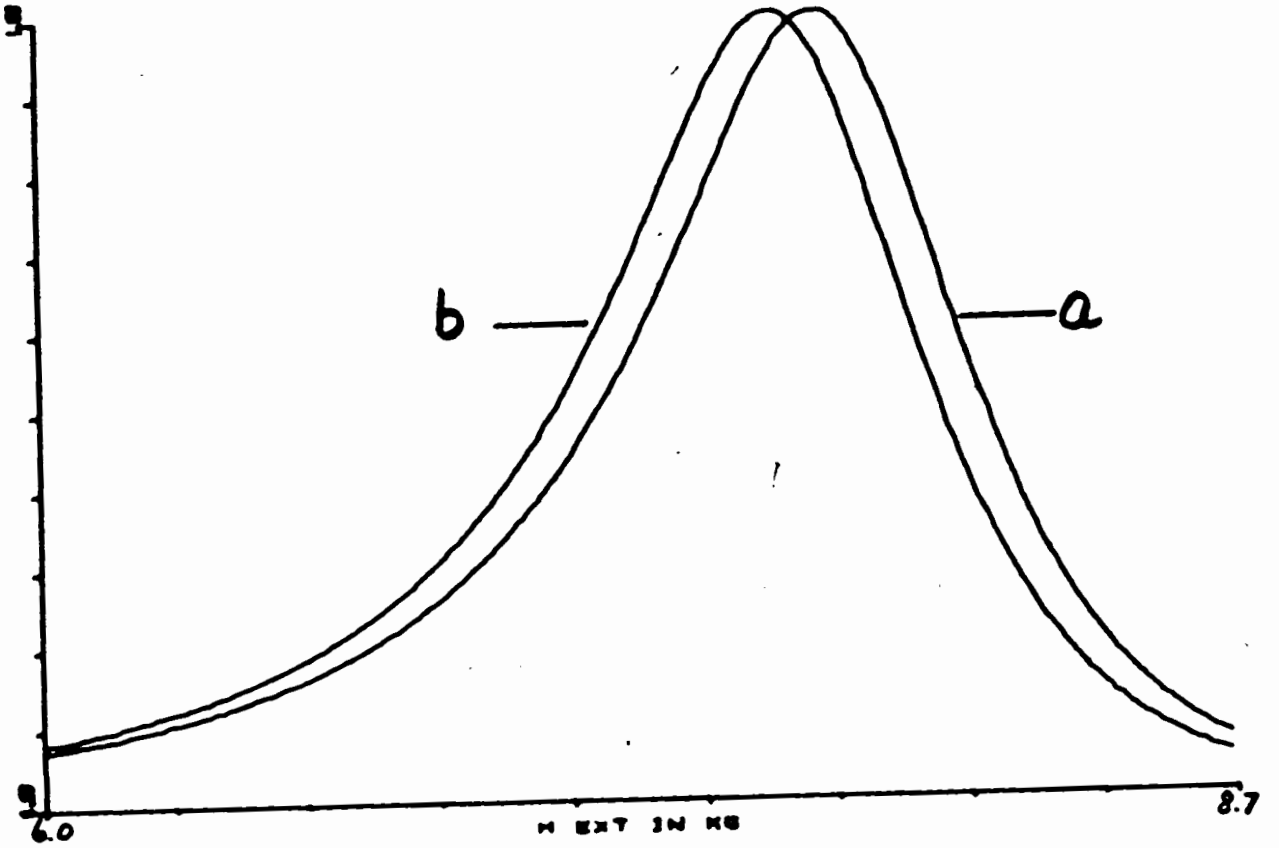

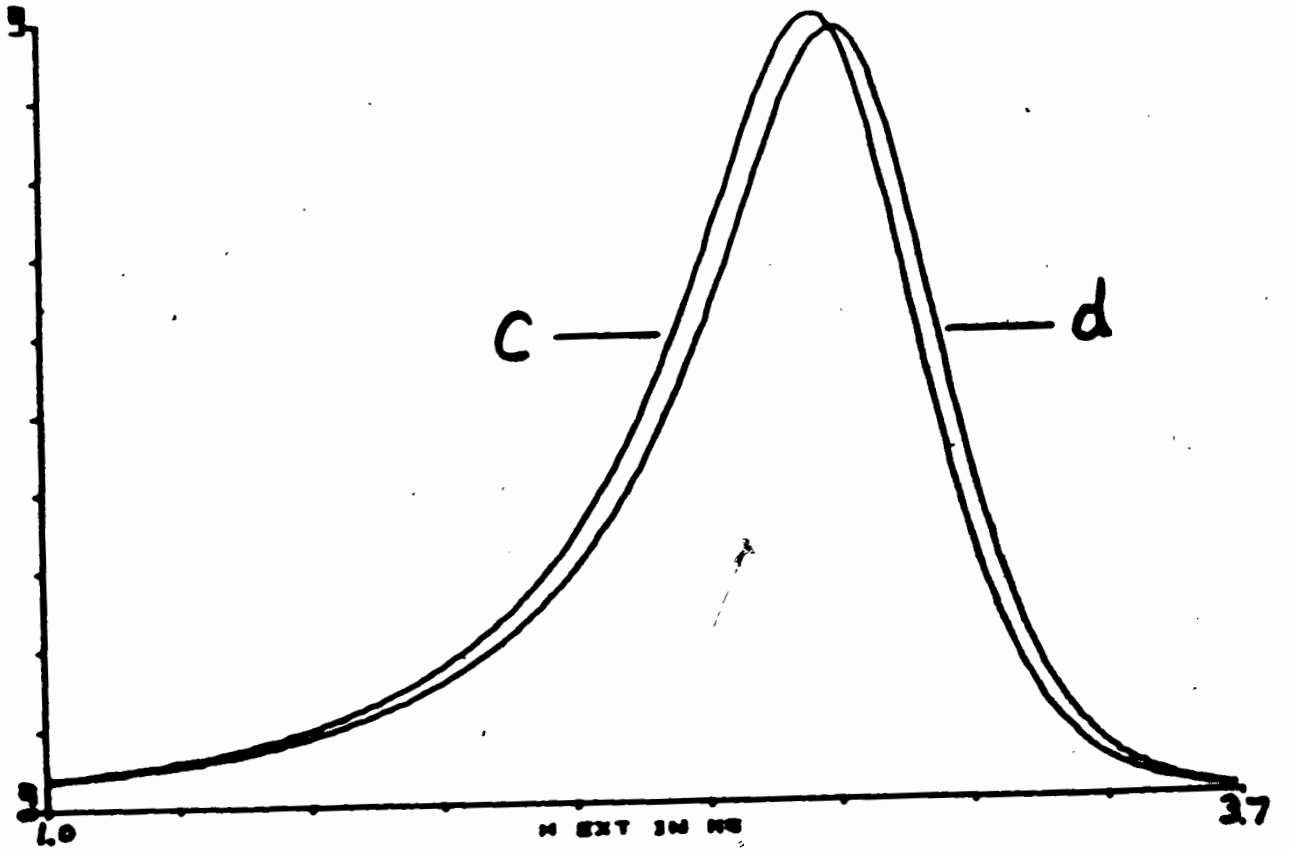

Fig. 2.9

determines the magnetization; and the width of the peak in the parallel configuration provides a second determination of the damping parameter[3]. The other parameters which influence the transmission either have a negligible effect (exchange) or are available from independent measurements or published data (R.F. frequency, sample thickness, resistivity, static demagnetization factors, and anisotropy and magnetostrictive constants).

---

[3] The damping parameter for the parallel configuration need not equal the damping parameter for the perpendicular configuration. If a mechanism exists in which a spin wave of propagation constant $\vec{k} \approx 0$ decays into two spin waves of large $\vec{k}$, then conservation of energy and total $\vec{k}$ allows this process to occur in the parallel configuration and not in the perpendicular configuration. For details of the spin wave dispersion relation see, for example, E.A. Turov in Ferromagnetic Resonance (1966), p.208 et seq.

CHAPTER 3

EXPERIMENT

The details of the apparatus used in the experiments reported here have been published elsewhere (Cochran et al. 1977b). A short description of the microwave circuit and data acquisition system used to record the transmission signal is given here along with a more complete description of the particular microwave cavities used in these experiments.

3.1 Microwave Circuit

The sample being studied formed part of the common wall between two microwave cavities. Microwaves were generated[1] and guided into one of the cavities; the signal which was transmitted through the sample appeared in the second cavity and a fraction of this signal was guided into the receiver section of the microwave circuit (see Fig. 3.1). This received signal was chopped at 30 MHz by a TRG750 electronic switch[2] and fed into a balanced mixer and pre-amplifier[3]. The 30 MHz output of the pre-amplifier was amplified further[4]

---

[1]Between 250 mW and 350 mW of 24 GHz radiation was available from an OK124V11 klystron made by OK1 Electronics of America, Inc., 500 S.E. 24th Street, Fort Lauderdale, Florida, 33316.

[2]Switch made by Alpha Industries, Inc., 20 Sylvan Road, Woburn, Maine, 01801.

[3]LEL KCH-2 switch made by the LEL division, Varian Associates, Copiague, Long Island, New York.

[4]LEL model IF 301-30-10-50 narrow band amplifier.

and then demodulated[5]. The balanced mixer was fed a reference signal coupled from the klystron. This reference signal passed through a precision phase shifter[6] and a 200 Hz chopper[7]. Thus the output of the system was a 200 Hz signal proportional to the amplitude of the received microwave signal in phase with the reference signal. This output was detected by a lock-in amplifier[8] and continuously recorded, along with the magnetic field, on an X-Y recorder and digitally recorded every three to six seconds on paper tape. Each measurement of transmitted amplitude vs. magnetic field was repeated with the phase shifter in the reference line altered by 90° between measurements. In this manner both the amplitude and the relative phase of the transmitted signal as a function of magnetic field were measured. The data were stored on magnetic disc and they were readily available for comparison with computed transmission curves based on the phenomenological theory described in Chapter 2.

Several other features of the microwave circuit bear explanation. A portion of the output of the klystron was

---

[5]HP10514A mixer made by Hewlett Packard Co., 1501 Page Mill Road, Palo Alto, Calif.

[6]DBE 8k9 manufactured by Systron Donney Corp., 1 Systron Dr., Concord, Calif.

[7]TRG K130, Alpha Industries.

[8]Ithaco 391A lock-in amplifier made by Ithaco Inc., 735 W. Clinton St., Ithaca, New York, 14850.

directed through a tunable reference cavity and detected by diode D1 of Fig. 3.1. The voltage across D1 served as an input to a control circuit which locked the frequency of the klystron to the resonant frequency of the reference cavity. Both the transmitter and receiver cavities could be tuned to the output frequency of the klystron by routing the microwave power into either cavity via switches TRG K530 and attenuator DBE 430. The signal refected from each cavity was detected at diode D2 or D3 and the cavities were mechanically tuned by minimizing the reflected signal. The microwave output of the klystron could also be shunted into the detection system through the circuit laballed "calibration line" in Fig. 3.1. This line could be used to direct a known fraction of the klystron output into the detector and this was used to calibrate the receiver and assorted amplifiers. The frequency of the microwave radiation was measured by means of a Hewlett Packard K432A frequency meter. This meter was calibrated with an accuracy of ± 0.01% using the ESR signal of DPPH. Further details concerning the microwave system are given by Cochran et al. (1977b).

3.2 Microwave Cavities

The experiments were carried out with three sets of microwave cavities, each set fabricated from either brass, stainless steel, or beryllium-copper.

The brass and stainless steel cavities were used for the high temperature measurements. Since these two sets of

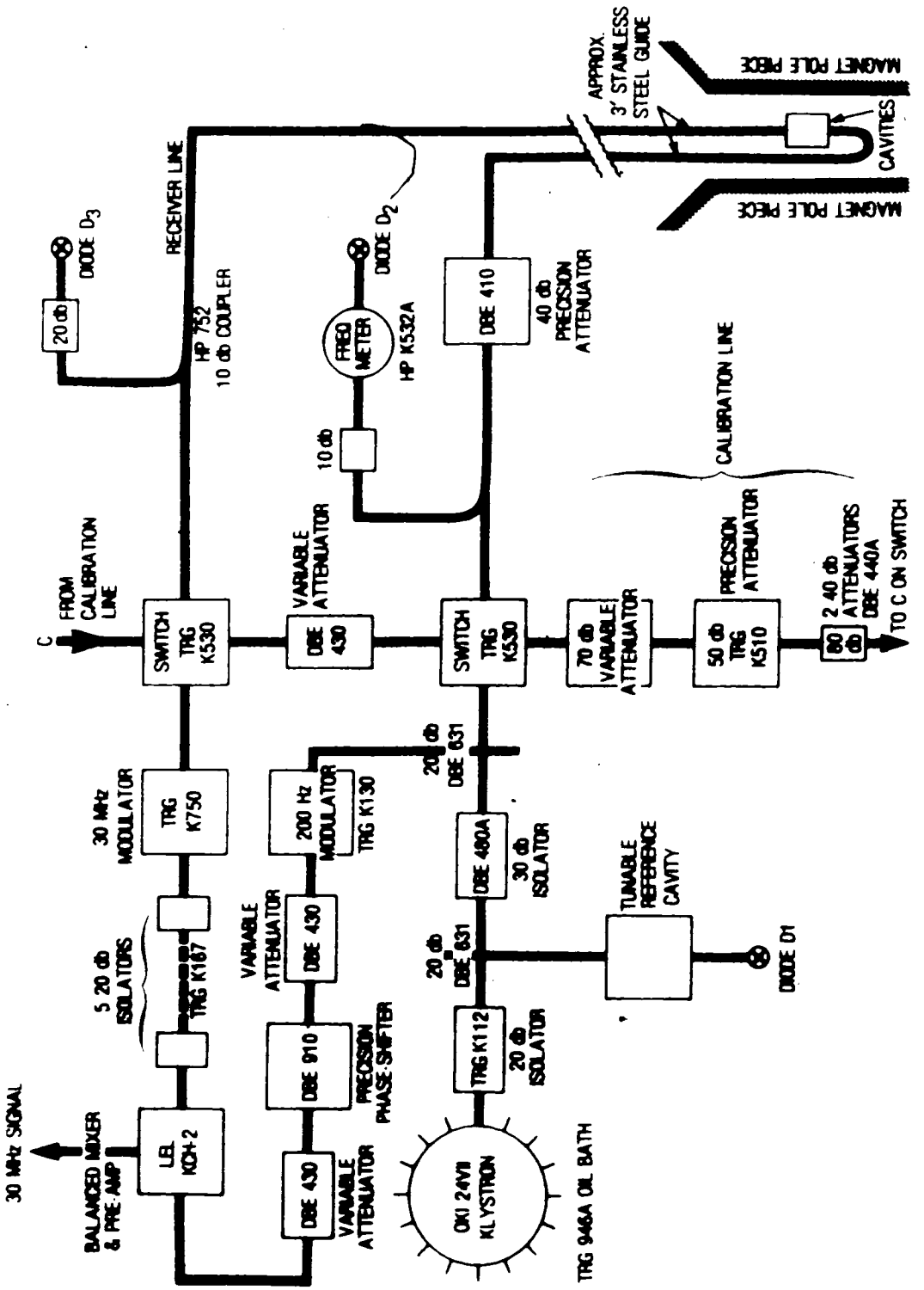

Fig. 3.1: Microwave circuit schematic. From Cochran et al. 1977(b).

cavities were similar in design, only the stainless steel cavities will be described here. The steel cavities are schematically shown in Fig. 3.2.

The stainless steel cavities were fabricated from two blocks of #304 stainless steel. The blocks were machined to the desired outside dimensions and then the cavities were spark cut into the blocks. The final inside dimensions of the cavities were 3.06 × 1.07 × 0.44 cm and coupling holes were cut in the H-wall of the cavities. The cavity quality factors, Q, were determined from the frequency shifts required to detune the critically coupled cavities so that half the incident power was reflected. The receiver and transmitter cavities had unloaded Q's of 1.4×10^3 and 1.2×10^3, respectively. The stainless steel cavities could be separately tuned by means of quartz rods 0.10 cm in diameter (Fig. 3.2). The rods fitted smoothly into holes 1.38 cm long drilled into the end walls of the cavities. These holes were beyond cutoff for the 24 GHz radiation; the fundamental mode in each hole had a damping length of 0.07 cm. Experiments using these cavities could be carried out at constant frequency over a wide temperature range because it was possible to compensate changes in cavity resonant frequency due to thermal expansion by altering the depth of insertion of the quartz tuning rods. The tuning capability of the brass cavities was less extensive in that only one cavity (the transmitter) was tunable via a brass screw threaded into the cavity end-wall. Thus the operating frequency of the brass cavities was

Fig. 3.2: View of cavities and sample: (a) quartz tuning rod, (b) transmitter cavity, (c) coupling hole, (d) sample, (e) critically coupled aperature between cavity and waveguide, (f) copper diaphragm, (g) receiver cavity, (h) interior of the receiver cavity. The transmitter cavity is bolted to the receiver cavity with the sample sandwiched tightly between the cavities. The directions of the RF magnetic field, h_{RF}, and the applied, static field in the parallel and perpendicular configurations, $H_{\parallel}$ and $H_{\perp}$, are indicated. The total height of each cavity is 4.44 cm.

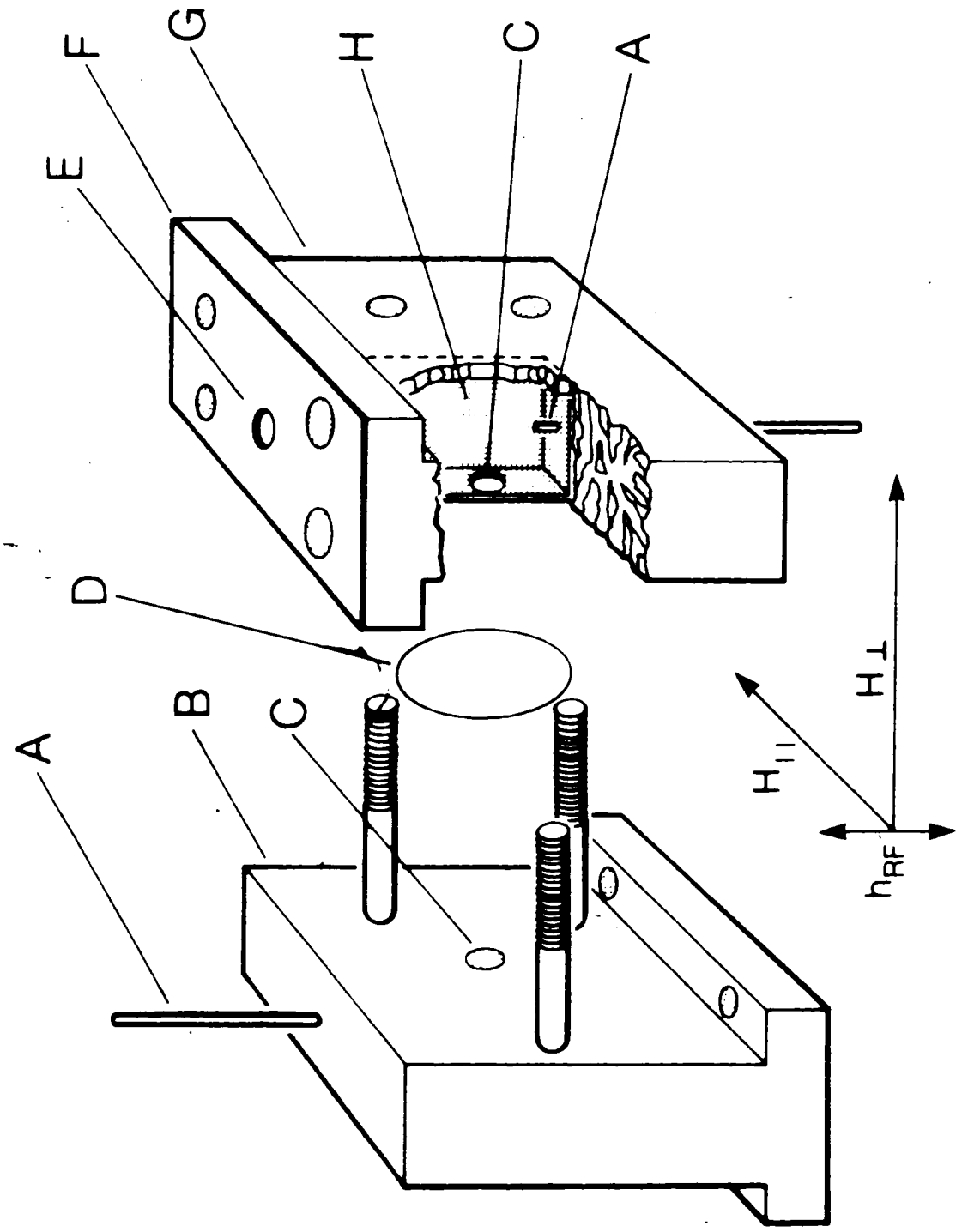
F
G
H
C
A
E
D
B
C
A
$H_{\perp}$
$H_{//}$
h_{RF}

constrained to follow the resonant frequency of the receiver cavity. This resonant frequency decreased with increasing temperatures because of the thermal expansion of the receive cavity.

The stainless steel cavities had two principal advantages over the brass cavities. First, the coefficient of thermal expansion of stainless steel is smaller than that of brass, but larger than that of nickel; at elevated temperatures the stainless steel cavities strained the rigidly clamped[9] nickel sample, but this strain was less than that produced by the brass cavities. Secondly, the brass cavities gave off zinc at elevated temperatures.

The principle disadvantage of the stainless steel cavities was that the steel was strongly paramagnetic[10]. In order to find the magnetic field shift (caused by the cavities) at the position of the specimen, the ESR signal (at 24 GHz) of a piece of DPPH glued to the centre of a copper specimen was measured using both the brass and the stainless steel cavities. The shift in the applied field, at resonance, between the two sets of cavities was determined as a function of angle of applied field with respect to the specimen normal.

---

[9] The sample actually fused to the cavities during the course of the measurements.

---

[10] These cavities eventually became useless when a fraction of the steel transformed to the ferromagnetic phase.

At 20°C the magnetic field at the position of the specimen was 18.6 ± .5 Oe less than the 8.57 kOe magnetic field applied along the specimen normal (along $H_{\perp}$ in Fig. 3.2). The magnetic field at the position of the specimen was 18.4 ± .5 Oe greater than the 8.57 kOe magnetic field applied in the plane of the specimen (along $H_{||}$ in Fig. 3.2). This shift in magnetic field was assumed to vary directly as the applied field and inversely as the absolute temperature of the stainless steel. The latter assumption was found to be consistent with shifts measured over the limited temperature range 20° to 50°C. Also, the shift was homogeneous near the centre of the sample in that the change in the shift caused by moving the piece of DPPH 1.2 mm from the centre of the copper specimen was less than one oersted.

During the measurements the cavity assembly was mounted in a vacuum of at least 10^{-4} torr and heated by a non-inductively wound heater supplied from a Kepco bipolar operational power supply/amplifier [11]. The temperature, monitored by a chromel-alumel thermocouple, was found to be stable to ± 0.5°C over periods comparable to the time required to take a transmission measurement. The nominal error stated by the manufacturer[12] for the thermocouple material was the larger of ± 2°C or + 3/4%.

Each time the heater power was changed the apparatus was left at least four hours before the transmission measurements were made in order for the temperature to stabilize.

---

[11] Kepco, Inc., 131-38 Sanford Avenue, Flushing, New York, 11352.

[12] Thermo Electric (Canada) Ltd., Brampton, Ontario.

The beryllium-copper cavities were used for the low temperature microwave measurements. These cavities were designed to function with the sample mounted in the common end-wall of the cavities[13], Fig. 3.3. (The sample had to be initially mounted on a nickel diaphragm. See Chapter 5.) Beryllium-copper stock was machined into two blocks 2.5 × 2.5 × 3.1 cm and the cavities (1.07 × 0.44 × 3.1 cm) were spark cut through the length of the blocks. Provision was made to tune the cavities with quartz plugs introduced through holes drilled in the sides of the cavities.

The main feature incorporated into these cavities was the capability to remotely tighten or loosen the screws holding the transmitter and receiver cavities together. In operation, the cavity assembly was sealed into a stainless steel can, which excluded liquid nitrogen or helium from the cavities, and the assembly was lowered into a stainless steel dewar (Lyall 1970). The two cavities were tightened, sandwiching the sample between them, only after the temperature of the system was below 80K or stabilized at some higher temperature. This was done to avoid buckling the nickel sample during the cool-down process because of the differential thermal contraction between beryllium-copper and nickel.

---

[13] Note that the magnetic field could be applied only in the plane of the sample.

Fig. 3.3: Schematic of the beryllium-copper cavities. Vertical motion of tuning rod (a) controlled the depth a spring loaded quartz plug (b) entered the cavity. Both cavities were tunable. (Only one tuning rod is shown.) One of the three bolts (c) used to remotely tighten the cavities together is shown. The sample diaphragm (d) served as the common end-wall of the cavities. Critically coupled copper diaphragms (e) served as the remaining end-walls.

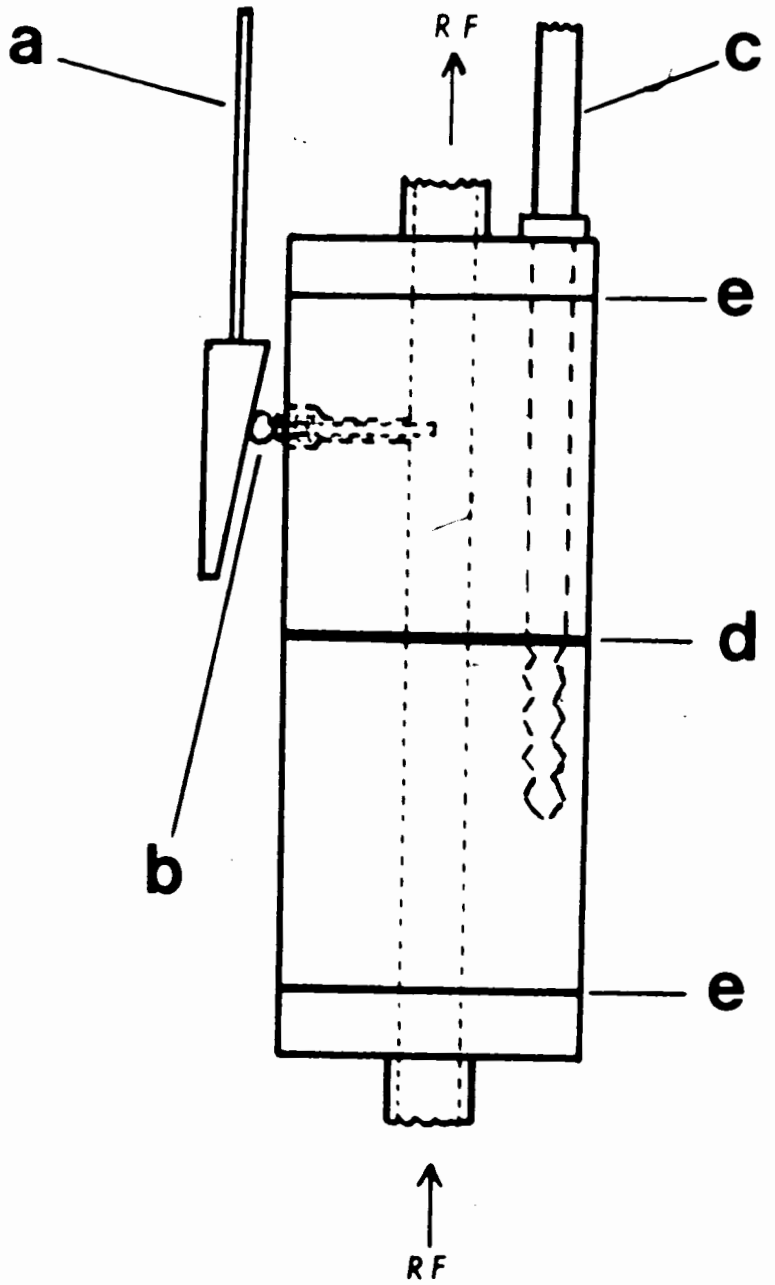

Fig. 3.3

3.3 Magnet System

The sample assembly was mounted in the 8.9 cm gap of a Varian V-3800 thirty-eight centimeter electromagnet[14] having a magnetic field uniform to at least 0.1 oersted over the volume of the specimen. A signal proportional to the magnetic field was obtained from a Bell model 620 gaussmeter[15]. The gaussmeter was usually calibrated from the VFR 2701 Mk II Fieldial magnet power supply and was accurate to ±5 oersted. For one sample, Aug20Ni (see Table 4.1), the field was calibrated with an accuracy of ± 1 oersted by means of an NMR probe.

---

[14] Varian Associates, 611 Hansen Way, Palo Alto, California.

---

[15] F.W. Bell, Inc., Columbus 12, Ohio.

Chapter 4

TRANSMISSION MEASUREMENTS ON POLYCRYSTALLINE NICKEL

Microwave transmission measurements were carried out on polycrystalline nickel foils of 7μm and 20μm thicknesses[1]. The aim of these experiments was to examine the temperature variation of the magnetic damping and g-factor between room temperature and the Curie temperature. The temperature dependent magnetization was also extracted from the transmission data.

This chapter is organized as follows. A short description of the samples and sample preparation is given. Next are two sub-sections which describe how the data were analyzed using a computer program based on the calculations of Chapter 2. Finally, the results of these measurements are presented.

4.1 Samples and Sample Preparation

Samples were cut from 7μm and 20μm thick polycrystalline nickel sheets[2]. Squares of nickel (2 × 2cm) were cut from the sheets with a razor blade and batches of three or four of the

---

[1] Most of the material in this chapter has been reported in the literature (Dewar et al. 1977).

---

[2] Nickel obtained from Goodfellow Metals Ltd., Ruxley Towers, Claygate, Esher, Surrey, England, KT10 OTS. A Certificate of Analysis from the company stated that the principle impurities were: CU (<0.25%), Fe (<0.40%), C (<0.15%), Si (<0.15%), Mn (<0.35%), Mg (<0.20%), Ti (<0.10%), S (<0.10%). The total of all other elements except Co was <0.001%. Nickel (plus some Co) made up more than 99.0% of the foil.

squares were sandwiched, side by side, between two similar Supermalloy squares 50μm thick. Each batch was held between the end faces of two pieces of 2 cm diameter cylindrical stock and turned on a lathe. This procedure produced flat, unscratched discs without burrs on their edges. The discs[3] were placed on either an alumina or a molybdenum substrate and annealed at 1000°C for one hour, with heating and cooling rates of 100 deg/h.

Extensive measurements were made on three specimens. The physical parameters of these specimens are listed in Table 4.1. The mass and diameter of each disc were measured and the thickness was then computed from the density of nickel of 8.902 gm/cm^3 (Metals Handbook, 1961). The thickness and diameter of the discs were used to compute the demagnetization factors by assuming the discs to be uniformly magnetized.[4] (See Kraus and Frait (1973) for a discussion of this approximation.) Under the assumption that the sample was uniformly magnetized perpendicular to the plane of the disc the demagnetization factor D_{zz} appropriate to the centre of the disc can be written as a power series in r, where r is the

[3]The 13mm diameter sample, NiUNJ11B, was not annealed before transmission measurements were made on it.

[4]The demagnetization factor D_{zz} calculated on the assumption that the discs were uniformly magnetized, was within 6 parts in 10^4 of the values obtained using the oblate spheroid model (Schmidt et al., 1964). For example, $D_{zz} = 0.9982$ for sample Ni20. These two calculations are upper and lower bounds for the appropriate demagnetization factor for a right circular disc (Kraus and Frait, 1973).

ratio of the thickness to the diameter of the disc. The first three terms of this series are:

$$D_{zz} = 1 - r + 2r^3 \qquad (4.1a)$$

The demagnetization factor D_{xx} is then determined from

$$D_{xx} = (1 - D_{zz})/2 \qquad (4.1b)$$

The demagnetization factors for the samples used in these measurements, found from Equations (4.1a) and (4.1b), are given in Table 4.1.

One disc, 16mm in diameter, was used with a set of brass microwave cavities; the other discs, 13mm and 18mm in diameter, were used with a set of stainless steel cavities. For the 18mm sample only a central portion smaller than the cavity coupling hole was exposed to RF radiation. This was accomplished by evaporating an annular (2.5mm inside diameter, 18mm outside diameter) aluminum film 1.5μm thick on both sides of the sample. The aluminum was used in an effort to reduce any possible effects on the RF transmission due to inhomogeneous strains in the nickel sample where the edge of the coupling hole gripped it. A similar gold film 6μm thick was evaporated on one side of the 13mm sample. The area of this sample exposed to microwaves was approximately 0.01 cm^2.

Strips of nickel were cut from the same sheets, and given the same thermal treatment, as the samples used in the transmission experiments. These strips were used to determine the

Table 4.1

Physical parameters of samples. Subscripts refer to Figure 2.3. The demagnetization factors were calculated as indicated in Equations (4.1a) and (4.1b).

Name	Diameter	Thickness (μm)	Demagnetization Factors D_{xx}	D_{zz}
Ni20	15.73 ± .02	19.0 ± .6	0.0006	0.9988
Aug20Ni	17.95 ± .02	19.12 ± .02	0.0005	0.9989
NiUNJ11B	13.39 ± .02	7.39 ± .02	0.0003	0.9994

resistivity between room temperature and 400°C. The results of two measurements on the 20μm foil are shown in Fig. 4.1. The thermocouple used to measure the temperature of the stainless steel cavities during the transmission experiments was calibrated against the thermocouple used to make resistivity measurements in order to eliminate uncertainities in the resistivity at a particular temperature due to differences between these thermocouples.

Fig. 4.1. Measured resistivity of nickel foil as a function of temperature for two different samples of 20μm foil. Estimated uncertainty in the resistivity is ≈ 2%. The Curie temperature was obtained from the kink in the curve of resistivity vs. temperature and was found to be T_c = 354 ± 4°C, in good agreement with data reported in the literature, for example: 354°C (Weiss and Forrer 1926) and 358°C (Arrott and Noakes 1967).

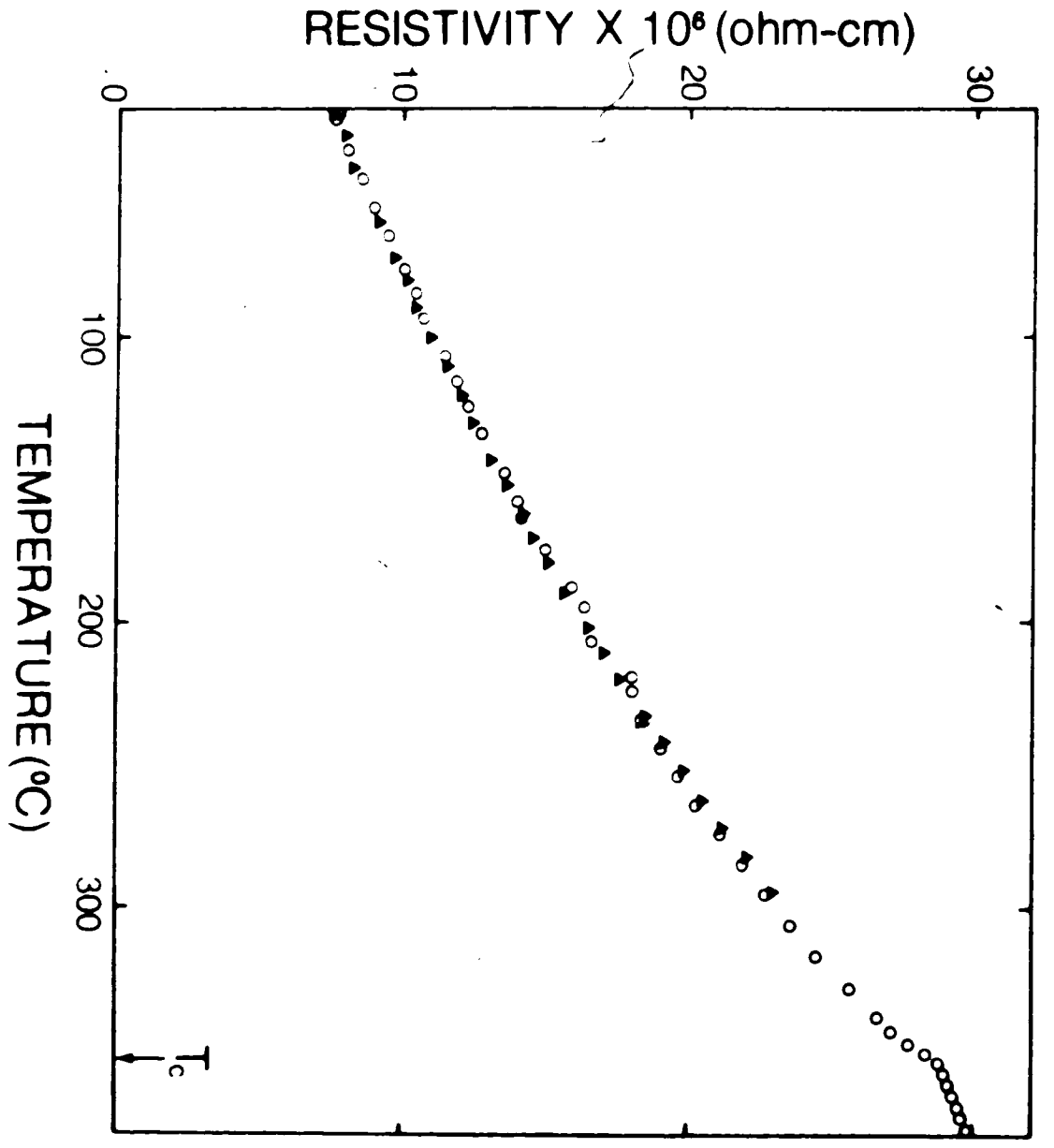
RESISTIVITY X 10⁶ (ohm-cm)
0
10
20
30
TEMPERATURE (°C)
100
200
300
T_c

Fig. 4.1

4.2a Analysis of Data: $T < T_c$

In the calculation of theoretical curves of transmission amplitude versus applied magnetic field it was necessary to specify values for specimen's g-factor, magnetization, and damping parameter along with predetermined values for the thickness, resistivity, and demagnetization factors. First estimates of the g-factor and magnetization were made using the following procedure. If it is assumed that the specimen is an infinite sheet with no magnetic damping, the peak of the transmission curve occurs at

$$H_o = \omega/\gamma \qquad (2.28)$$

in the perpendicular configuration and at

$$H_o = \omega/\gamma - 4\pi M_o \qquad (2.35)$$

in the parallel configuration. (See Chapter 2.) As a first approximation the g-factor was obtained from the position of the peak of the experimental transmission curve in the perpendicular configuration and the magnetization was obtained from the difference between the experimental peak positions in the parallel and perpendicular configurations. These values were then used, together with an estimate of the damping, to calculate a theoretical curve of transmission amplitude versus external field, H_o. This calculated curve was compared directly with the experimental data and corrections to the g-factor. magnetization, and damping parameter were estimated for the

next iteration. Two or three iterations were generally sufficient to obtain excellent agreement between the calculated and observed variation of transmission with magnetic field. Typical examples of the degree of agreement which can be obtained between theory and experiment, for temperatures well below the Curie temperature, are shown in Figs. 4.2 and 4.3 for the parallel and perpendicular configurations, respectively. The small differences between the calculation and experiment, obvious on the low field side of the peak in Figs. 4.2 and 4.3, varied from sample to sample. I attribute these differences to small non-uniformities of the effective field inside the polycrystalline samples arising from magnetocrystalline anisotropy and from the magnetostrictive effective field. (Usually two magnetostrictive constants are used to describe strain effects in a single crystal; in a poly-crystalline material a single, average magnetostrictive constant is used.)

The data presented in Figs. 4.2 and 4.3 was typical of measurements on the polycrystalline nickel samples. The analysis described above was carried out on several tens of sets of transmission data to determine the g-factor, magnetization, and damping parameter for nickel from room temperature to within 30°C of the Curie temperature.

Fig. 4.2. Transmission amplitude vs. applied magnetic field for the 18 mm sample in the parallel configuration. The measurement was made at 272°C. The calculated transmission (solid line) is normalized to the experimental peak amplitude (points). Parameters used for the calculated transmission are: RF frequency = 23.860 GHz, $g = 2.186$, $M_o = 326$ gauss, resistivity = $21.2 \times 10^{-6}\Omega$cm, $3\lambda_s\sigma/4\pi M_o^2 = -2.1 \times 10^{-2}$, $\lambda = 2.4 \times 10^{8}$ sec^{-1}, $D_{xx} = 0.0005$, and $D_{zz} = 0.9989$.

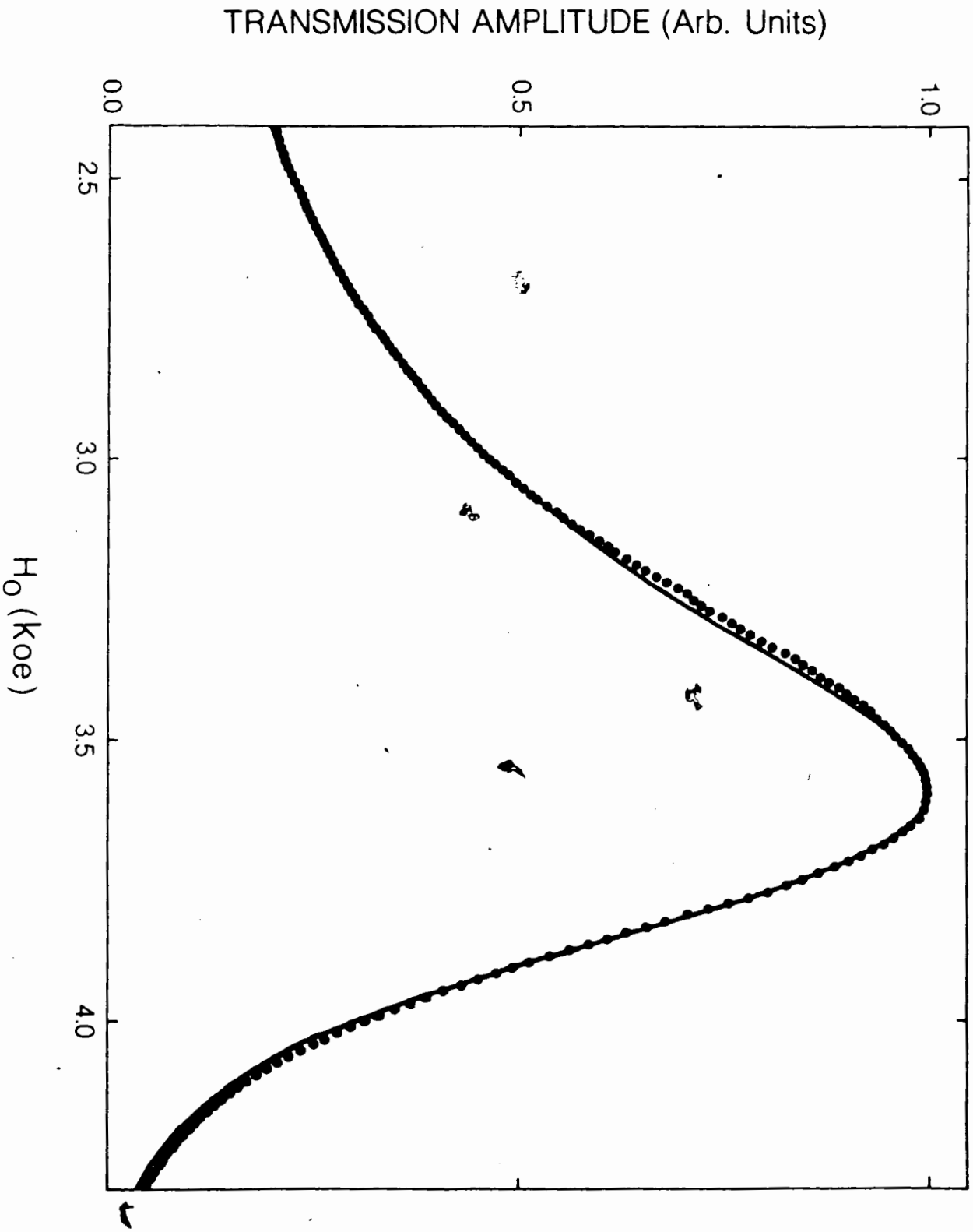

Fig. 4.2

Fig. 4.3: Transmission amplitude vs. applied magnetic field for the 18mm sample in the perpendicular configuration. The measurement was made at 272°C. The calculated transmission (solid line) is normalized the experimental peak amplitude (points). Parameters used for the calculated transmission are: RF frequency = 23.860 GHz, g = 2.186, M_o = 326 gauss, resistivity = 21.2 x $10^{-6}\Omega$cm, $3\lambda_s\sigma/4\pi M_o^2$ = -2.1 x 10^{-2}, λ = 2.4 x 10^8 sec^{-1}, D_{xx} = 0.0005, and D_{zz} = 0.9989.

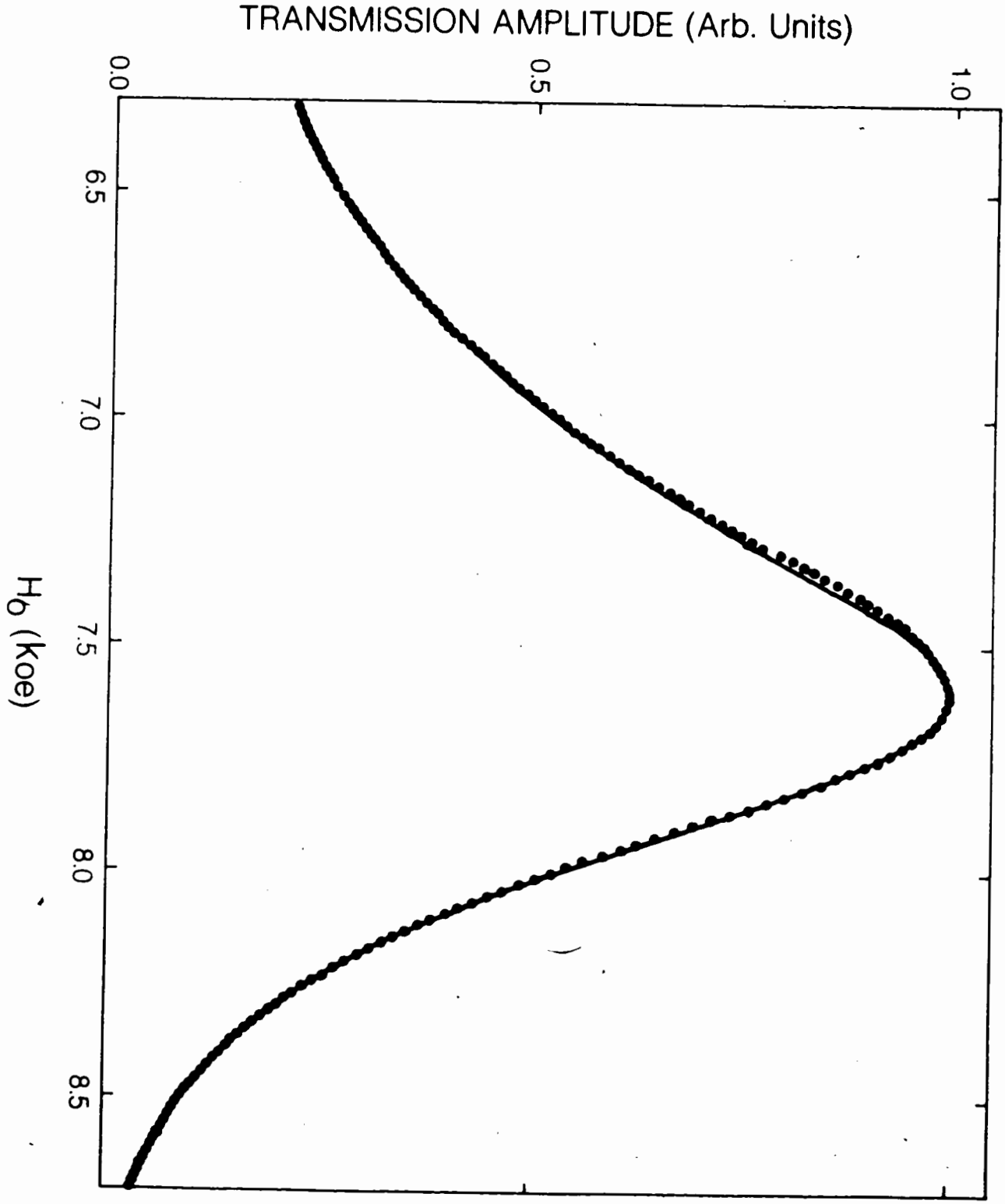
TRANSMISSION AMPLITUDE (Arb. Units)
0.0
0.5
1.0
6.5
7.0
7.5
8.0
8.5
H_0 (Koe)

Fig. 4.3

4.2b Analysis of Data: $T \approx T_c$

For temperatures near T_c the above procedure for obtaining the magnetization, g-factor, and damping was slightly modified because one must take explicitly into account the variation of the magnetization with the magnitude of the internal magnetic field. Near the Curie temperature the magnitude of $\vec{M}_o$ varies appreciably with the strength of the applied field. The equation of state for nickel of Arrott and Noakes (1967),

$$\left(\frac{H}{M_o}\right)^{1/\delta} = \frac{T - T_c}{T_1} + \left(\frac{M_o}{M_1}\right)^{1/\beta} \qquad (4.2)$$

was used to calculate M_o at given values of temperature, T, and static internal field,

$$H = |\vec{H}_o + \vec{H}_D|. \qquad (4.3)$$

In the limit of zero applied field M_o becomes M_s, the saturation magnetization[5]. In Equation (4.2) T_1, M_1, δ, and β are fitting parameters.

Instead of fitting the transmission data to g, λ, and M_o they were fitted to g, λ, and $(T - T_c)$ using the Arrott and Noakes (1967) equation of state, Equation (4.2). A set of transmission data consisted of one measurement made in the

---

[5] This assumes a specimen which consists of a single domain. The theory cannot, of course, describe a multi-domain system and it is therefore only valid for fields sufficiently large to remove all domain boundaries from the active volume of the specimen.

parallel configuration and one measurement made in the perpendicular configuration. Both transmission measurements were made at the same temperature. The procedure used to find $(T - T_c)$, g, and the damping was as follows:

1) An initial estimate of $(T - T_c)$ was made. This was done by either estimating M_o from the separation of the transmission peaks in the parallel and perpendicular configurations and then using the Arrott and Noakes equation[6] to obtain $(T - T_c)$ or by directly using the measured temperature of the sample and the Curie temperature as determined from resistivity measurements. The method used to obtain the initial estimate of $(T - T_c)$ was not crucial.

2) The initial value for the g-factor was estimated from the position of the transmission peak in the perpendicular configuration.

3) An initial value for the damping parameter was estimated from the width of the transmission peak in the perpendicular configuration.

4) Values for $(T - T_c)$, g, and the damping were used to generate curves of transmission amplitude versus applied magnetic field in which the magnitude of the magnetization, as given by the Arrott and Noakes

---

[6]The parameters Arrott and Noakes (1967) determined for Equation (4.2) (δ = 1.31, β = 0.3864, M_1 = 39.5 G, and T_1 = 0.309°C) were used in this analysis.

equation (Equation (4.2)), was allowed to vary with the internal field. These curves were calculated for both the parallel and perpendicular configurations.

5) Comparison with experiment indicated how the parameters $(T - T_c)$ g, and the damping had to be modified to secure better agreement between theory and experiment. (The damping parameter for the parallel configuration was allowed to take on a value different from the damping used for the perpendicular configuration.)

6) Steps (4) and (5) were repeated until no further improvement between the theoretical and experimental curves could be made.

For temperatures near T_c the shapes of the experimental transmission curves were sensitive to the procedure used to determine the transmission zero. In this case the experimental transmission at 11 kOe was arbitrarily assigned the value zero and the calculated transmission curves were altered by subtracting the calculated transmission at 11 kOe from the curves. This subtraction of a vector baseline (amplitude and phase) from the theoretical transmission curves made very little difference to the shapes of the curves except for temperatures above T_c, where the transmitted amplitude was a very slow function of applied magnetic field. (See Figs. 4.10 and 4.11). The transmission amplitude at 11 kOe included leakage between the cavities but in the perpendicular

configuration it also included the transmitted left-hand circularly polarized radiation which does not interact strongly with the magnetization.

The transmission measurements made in the vicinity of the Curie temperature were influenced by two effects which were negligible at lower temperatures. First, the magnitude of the magnetization was magnetic field dependent and, second, there was significant transmission through the sample for all values of applied magnetic field. These two effects were allowed for by introducing the Arrott and Noakes (1967) equation of state for nickel into the analysis and by introducing an arbitrary zero level into both the transmission measurements and the calculations.

4.2c The Role of Strain

The samples were strained during the measurements because the thermal expansion of the nickel was less than that of the brass or of the stainless steel cavities. In order to obtain the values of the magnetostrictive demagnetization factors appropriate to the 18 mm sample the following stress-strain history was assumed. (a) The sample was unstrained until it reached 120°C, whereupon it ceased to slip relative to the cavities. This assumption was supported by the fact that there was microwave leakage around the sample for the measurements up to 100°C and not for the measurement at 120°C. This indicated that the sample was not gripped tightly by the cavities until the temperature reached 120°C. Also, the apparatus was left at 120°C for one week before the transmission measurements were made. (b) Upon increasing the temperature beyond 120°C the stress was proportional to the strain until the stress reached the yield strength. Thereafter the stress remained constant to the highest temperature reached. Creep was neglected. (c) The stress decreased proportionally with the strain with decreasing temperature until the stress reached zero. (d) At this point the sample was assumed not to be able to support a compressional stress but to bend instead. As the temperature decreased to room temperature the sample bent further but was nearly stress free. (When the apparatus was disassembled the sample was indeed observed to be permanently deformed

into a dish shape.)

The magnetostrictive demagnetization factors for the 18mm sample were calculated from the elastic constants of nickel (Simmons and Wang 1971) and from the strain found from the differential thermal expansion of nickel and stainless steel (Thermophysical Properties of High Temperature Solid Materials 1967). The yield strength of annealed nickel was taken to be 8,500 psi (Metals Handbook 1961). The temperature dependent value of the magnetostrictive constant used in calculating the demagnetization factors was taken from Birss and Lee (1960). The magnetization was treated as a parameter to be found, as indicated in Section 4.2a.

The primary effect of the stress was to shift the position of the peak transmission amplitude by $+(3\lambda_s\sigma/M_o)$ gauss[7] in the perpendicular configuration and by $-(3\lambda_s\sigma/2M_o)$ gauss in the parallel configuration. (See Appendix I.) Fig. 4.4 shows the magnitude of the shift in the perpendicular configuration as a function of temperature. It is clear that magnetostrictive fields approaching 100G were present in the nickel sample.

The effect of strain in the sample was to alter the position of the transmission peak in both the parallel and perpendicular configurations. The g-factor and magnetization extracted from experiment were dependent on these peak

[7]Here λ_s is the magnetostrictive constant and σ is the magnitude of the uniform planar stress in the sample. σ is the conventional symbol for stress and is not to be confused with the conductivity.

Fig. 4.4: The calculated shift of the position of the FMAR peak in the perpendicular configuration caused by thermal strain vs. temperature. The arrows indicate the cycle this shift followed as the sample was heated and cooled. The sample was assumed to be unstrained at the point labelled "A".

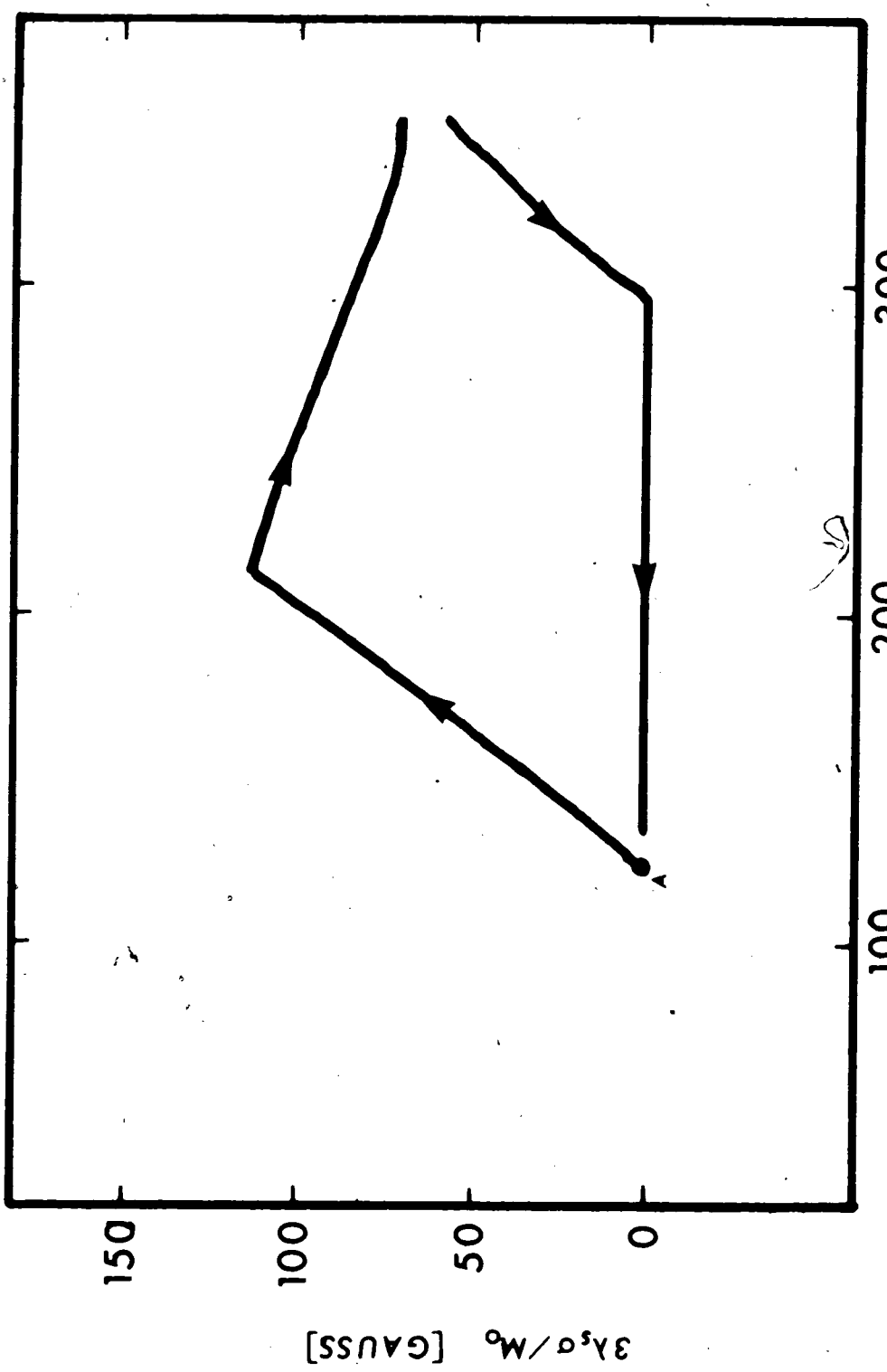
150
100
50
0
$3\lambda_s\sigma/M_o$ [GAUSS]
100
200
300
TEMPERATURE [°C]

Fig. 4.4

positions. In the following sections results for the g-factor and magnetization obtained both with and without allowing for the effect of strain are presented. The strain played no role in determining the damping parameter extracted from the data.

4.3a Results: Damping Parameter from Transmission Lineshapes

The Landau-Lifshitz damping parameter for both the 16 and 18 mm samples, determined from the curve-fitting procedure described above is plotted against temperature in Fig. 4.5. For temperatures above 100°C, but below T_c, a change of 4% in the damping parameter resulted in noticeably poorer agreement between the calculated and measured transmission lineshapes. There could also be a systematic error in the damping parameter of 3% due to uncertainties in the measurement of resistivity and thickness of the specimens. Below 100°C comparison of theory and experiment for the 18 mm specimen was made difficult by microwave leakage around the sample. This problem was alleviated at higher temperatures partly because the transmission amplitude increased and partly because the specimen became sintered to the stainless steel cavities. There was no perceptible leakage around the 16 mm sample.

The magnetic anisotropy of nickel tended to broaden the observed transmission lineshapes and, since this broadening was not taken into account in the theoretical calculation, the damping parameter obtained by comparing the calculation with experiment overestimated the intrinsic damping in the sample. Fortunately, this effect due to anisotropy was only significant for temperatures less than 100°C. (See Fig. 4.5.)

Neglecting the data for temperatures less than 100°C, the Landau-Lifshitz damping parameter as determined from the FMAR transmission measurements had the temperature independent

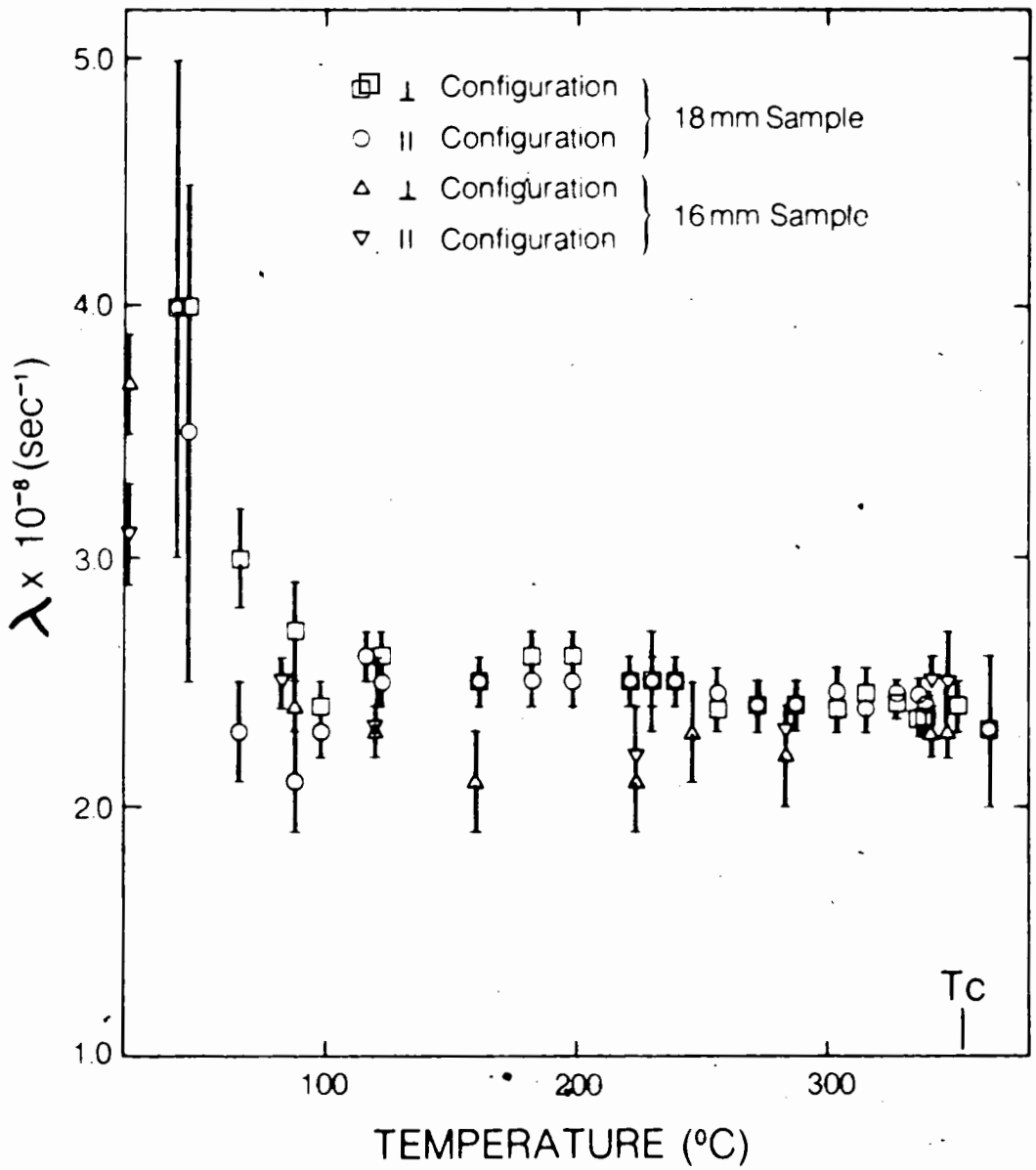

Fig. 4.5: Landau-Lifshitz damping parameter for nickel as a function of temperature. The error bars signify the limits to which λ could be varied without resulting in totally unacceptable fits between calculated and measured lineshapes.

value $\lambda = 2.45 \pm .1 \times 10^8$ sec^{-1}. This is comparable to the values $\lambda = 2.3 \times 10^8$ sec^{-1} (Bhagat and Chichlis 1969, Anders et al. 1971) and $\lambda = 2.5 \times 10^8$ sec^{-1} (Rodbell 1964) obtained from FMR measurements on carefully prepared nickel single crystals and platelets. In particular, the damping parameter observed in the present work was constant in the temperature range 300° to 364°C. This observation is contrary to previous deductions made from FMR measurements which indicated that the damping parameter decreased by a factor of two in this temperature range (Bhagat and Chicklis 1969, Bhagat and Rothstein 1971). Bhagat and Rothstein found that none of the damping terms in Equation (2.9) adequately described their 9.4 GHz FMR data near the Curie temperature. They suggested that fluctuation effects may be important. The data here indicate that FMAR measurements are insensitive to whatever mechanism causes the FMR linewidths near T_c to be narrower than that which one would expect from a temperature independent damping.

The experimental lineshapes could be fitted equally well using either the Gilbert, the Bloembergen, or the Landau-Lifshitz form of damping. The best-fitting Gilbert damping parameter was numerically equal to the best-fitting Landau-Lifshitz damping parameter at all temperatures below T_c and slightly larger just above T_c. (See Table 4.2.) The Bloembergen damping parameter obtained for the 18 mm sample is plotted as a function of temperature in Fig. 4.6. From Fig. 4.6 it is clear that the value of the Bloembergen

TABLE 4.2

Parameters determined from fitting the experimental data with the phenomenological theory. The data were taken at 364°C and are shown in Figs. 4.10 and 4.11.

Form of Damping	Damping Parameter (sec^{-1})	g-factor
Landau-Lifshitz	$2.3 \pm .3 \times 10^{8}$	$2.20 \pm .02$
Gilbert	$2.5 \pm .3 \times 10^{8}$	$2.30 \pm .02$
Bloembergen	$3.0 \pm .4 \times 10^{10}$	$2.27 \pm .02$

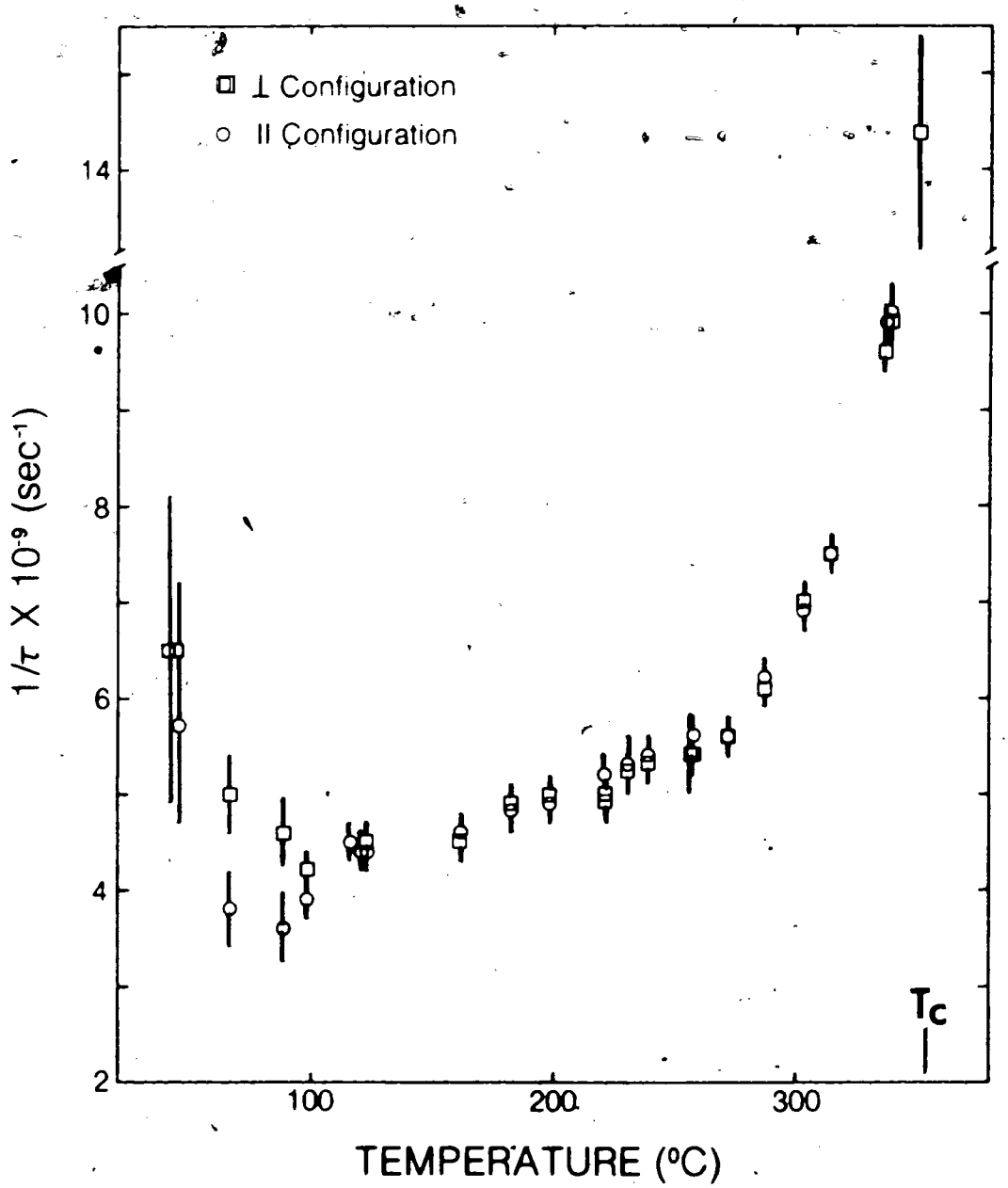

Fig. 4.6: The temperature dependence of the Bloembergen damping parameter which is required to fit the experimental data for nickel. Only results from data taken for temperatures less than the Curie temperature are shown. The error bars signify the limits to which $1/\tau$ could be varied without resulting in totally unacceptable fits between calculated and measured lineshapes.

damping parameter required to fit the data was markedly temperature dependent.

In summary, the linewidth of the FMAR transmission data was most simply described by a temperature independent Landau-Lifshitz damping parameter of $2.45 \pm .1 \times 10^{8} sec^{-1}$. The Bloembergen damping parameter described the data equally well but this damping parameter was found to be temperature dependent.

4.3b Results: Damping Parameter and the Maximum Transmission Amplitude

We were able to measure the variation of the maximum transmission amplitude at FMAR as a function of temperature. Fig. 4.7 is a plot of this maximum amplitude versus temperature for the polycrystalline 18 mm sample. The scale for the experimental points was determined by assigning the maximum amplitude at 257°C the value 1.0, all other amplitudes are plotted relative to this transmitted amplitude. The frequency dependent response of the microwave detection system was eliminated by using two stainless steel cavities which could be tuned to the same resonant frequency over a wide temperature range. This eliminated the primary source of error in such a measurement. The maximum amplitude at any one temperature was reproducible to ≈5%. Additionally, microwave leakage introduced some error into the measurements below 100°C (≈ 5% in the perpendicular configuration, ≈10% in the parallel configuration) and the uncertainty in the cavity Q-factor introduced an error of ≈6% at the highest temperature reached. For the measurement at 257°C the peak power detected (perpendicular configuration) was found to be 3×10^{-12} watts[8] (R.F. magnetic field amplitude along the axis of the waveguide = 2.1×10^{-7} oe). for an input power of 150 mW. This corresponded to a signal

[8] The transmission amplitude calculated from theory predicted a peak transmitted power of 5×10^{-12} watts for this level of power input. Waveguide losses were included in computing this transmitted power. See Cochran et al. (1977a) for a disucssion on the calculation of absolute values of transmitted power.

to noise ratio of 2×10^3 in the amplitude of the transmitted signal.

The maximum transmission increased as the temperature increased from room temperature because the sample resistivity increased, thereby causing a decrease in the total number of skin depths in the sample thickness. However, above $\approx 250°C$ the magnetization decreased rapidly with temperature and this caused the maximum transmission to fall to a level comparable with that observed in skin depth modulated electron spin resonance transmission.

The solid lines in Fig. 4.7 were generated from maximum transmission amplitudes calculated using $\lambda = 2.45 \times 10^8 \text{sec}^{-1}$, $g = 2.187$, and the magnetization appropriate for the 18 mm sample. Stress effects were included. The calculated curves were normalized by assigning the peak transmission in the perpendicular configuration the value 1.0[9]. The shape of the curves in Fig. 4.7 was found to be insensitive to the g-factor used in their calculation; however, the shape was sensitive to variations with temperature of the damping parameter. Consider, for illustrative purposes, a hypothetical temperature dependence of the damping of the form:

$$\lambda = \frac{1.46 \times 10^{11}}{(T + 340)} \text{ sec}^{-1} \qquad (4.4)$$

---

[9] The calculated ratio between the maximum transmitted amplitudes in the perpendicular and parallel configurations agreed with the experimentally observed ratio. See Cochran et al. (1977a) for a discussion of this ratio.

Fig. 4.7: Maximum transmission amplitude at FMAR plotted as a function of temperature. Experimental points are data taken for the 18 mm sample. The solid lines were calculated using the temperature independent damping of $\lambda = 2.45 \times 10^{8} sec^{-1}$ and $g = 2.187$. The dashed line was calculated using the temperature dependent damping of Equation (4.4). Stress effects were included. These calculated lines were normalized by requiring the peak transmitted amplitude in the perpendicular configuration to be 1.0. The error bars reflect the uncertainty in the gain of the detection system, the uncertainty in the temperature dependence of the cavity Q-factors, and the contributions of spurious leakage signals.

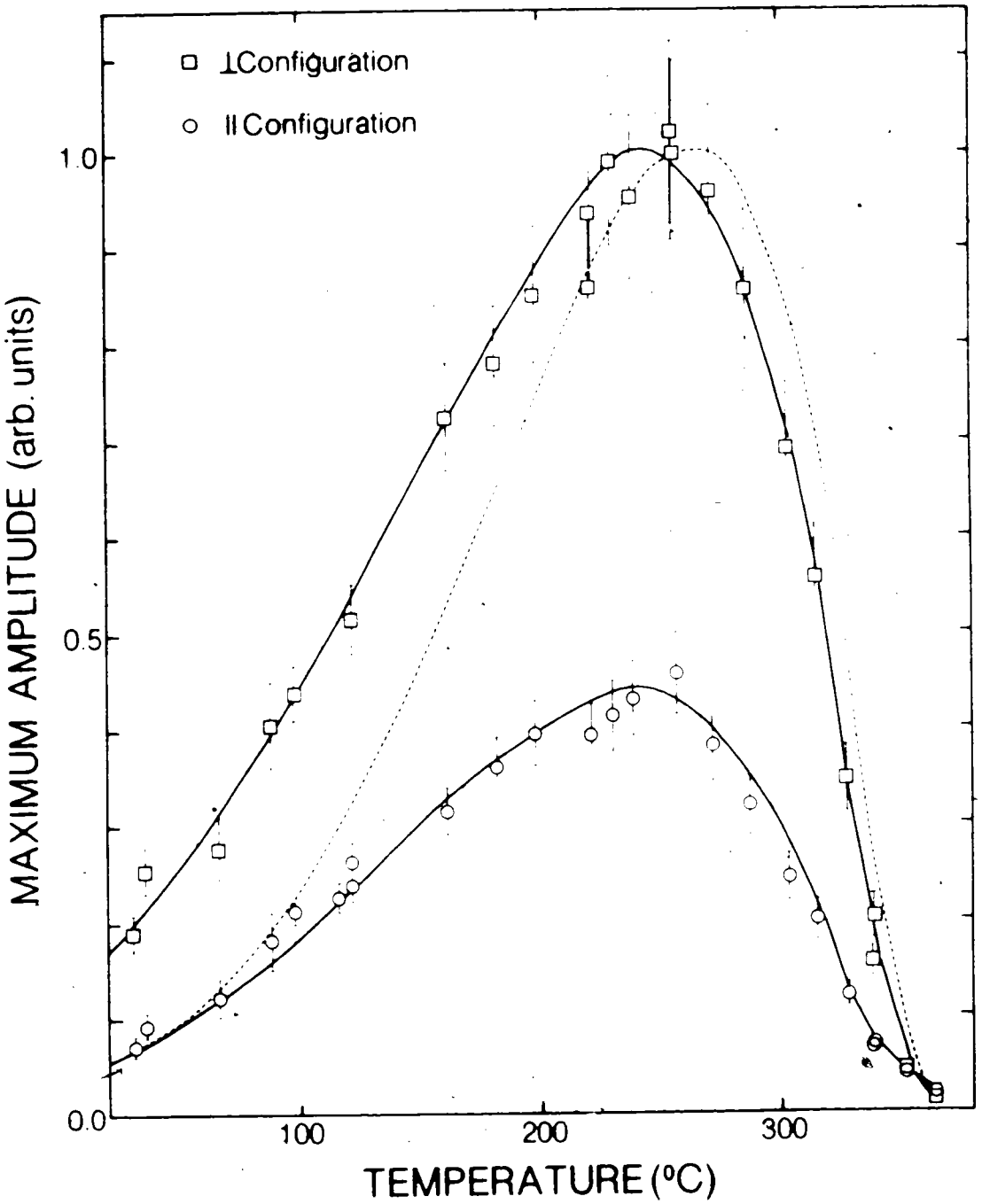
⊥Configuration
∥Configuration
1.0
0.5
0.0
100
200
300
MAXIMUM AMPLITUDE (arb. units)
TEMPERATURE (°C)

where T is the temperature in degrees Centigrade. This relation is not intended to represent the observed damping; it is used here only to indicate how a reasonable and relatively slowly varying temperature dependent damping would affect the variation of the maximum transmitted amplitude with temperature. This damping would have the value 4.0 $10^8 sec^{-1}$ at 20°C, $2.45 \times 10^8 sec^{-1}$ at 255°C, and $2.2 \times 10^8 sec^{-1}$ at 320°C. The dashed line in Fig. 4.7 is a plot of the maximum transmission amplitude in the perpendicular configuration versus temperature calculated using this temperature dependence of λ; all other parameters are the same as were used to calculate the solid curves. It is obvious that this temperature dependent damping factor gives a very poor fit to the experimental data. In particular, if the damping parameter of nickel did decrease about $0.25 \times 10^8 sec^{-1}$ between 255°C and 350°C, the transmission near 350°C relative to the transmission at 250°C would have been about a factor of two greater than the experimentally observed ratio. This is strong evidence that the Landau-Lifshitz damping parameter required to fit our data varies very little with temperature in the range 30° to 360°C.

4.3c Results: g-factor

The g-factor was extracted from the transmission data in the manner described in section 4.2. In Fig. 4.8 the g-factor for the polycrystalline 18 mm sample is shown as a function of temperature. Values of the g-factor found both with (filled symbols) and without (open symbols) using magnetostrictive demagnetization factors are plotted. Notice that in the case in which the magnetostrictive demagnetization factors are employed the g-factor for the measurement at 224°C[10], with temperature decreasing, lies far from the g-factors found from the data taken with the temperature increasing. This discrepancy is removed when the magnetostrictive demangetization factors are invoked. The data indicate that the g-factor for our sample had the temperature independent value of 2.187 ± .005. Previously reported g-factors were 2.22 ± .03 (Rodbell 1964, 1965) and 2.21 (Bhagat and Chicklis 1969).

[10] The transmission measurements at 224°C are shown in Figs. 1.1 and 1.2.

Fig. 4.8: The g-factor of nickel plotted as a function of temperatures for the 18 mm sample. The unfilled symbols indicate the g-factor determined from the experimental transmission data using the Landau-Lifshitz damping parameter without considering stress effects. Filled symbils represent the g-factors found with stress effects included. The error bars represent the range through which the g-factor could be varied without resulting in totally unacceptable fits between the calculated and measured transmission line positions. The error bars have been left off the filled symbols for clarity.

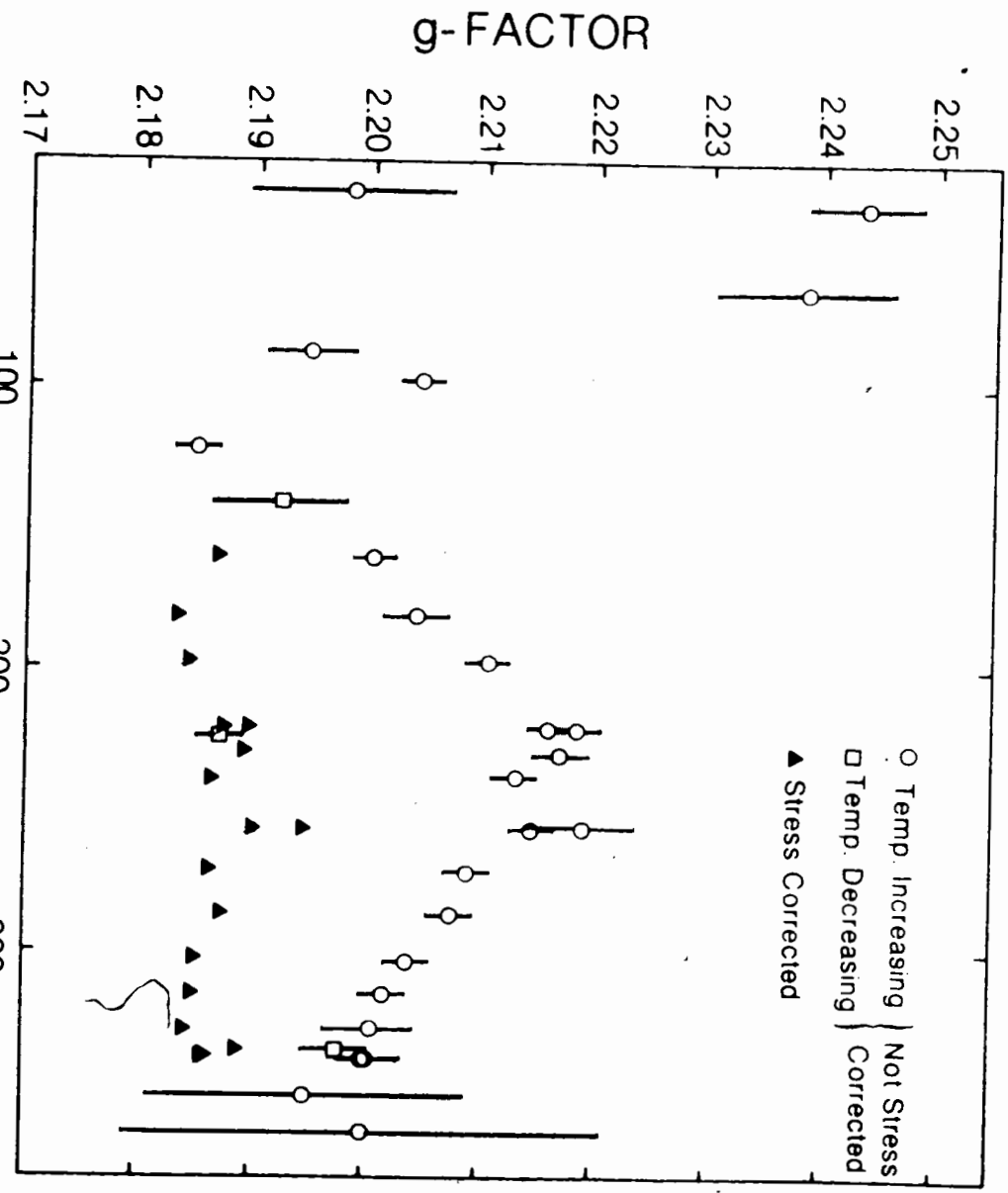
g-FACTOR
2.25
2.24
2.23
2.22
2.21
2.20
2.19
2.18
2.17
100
200
300
TEMPERATURE (°C)
○ Temp. Increasing } Not Stress
□ Temp. Decreasing } Corrected
▲ Stress Corrected

Fig. 4.8

4.3d Results: Transmission above T_c

It is notable that for temperatures slightly above the Curie temperature there is no FMAR effect. The magnetization, M_o, becomes so small that at no value of the external field does the real part of the dynamic permeability at 24 GHz become zero. This is the regime which corresponds to the original work on gadolinium reported by Lewis et al. (1966) and correctly explained by VanderVen (1967). Fig. 4.9 shows a family of calculated permeabilities versus applied magnetic field for temperatures near T_c. For nickel at 24 GHz the FMAR disappears between 354° and 356°C.

Figs. 4.10 and 4.11 show the experimental and calculated transmission amplitude versus magnetic field for the 18 mm sample at 364°C. The signal amplitude was much smaller at this temperature than below T_c; in fact, the peak amplitude in the perpendicular configuration corresponded to a detected power of 4×10^{-16} watts. (A system time constant of 0.3 seconds was used in taking this data.)

The g-factor required to fit the data at 364°C was dependent on the form of damping considered in the equation of motion for the magnetization, Equation (2.9). (See Table 4.2.) Salamon (1967) noted that the g-factor found using the Bloembergen form of damping to analyze his FMAR data changed from 2.21 below T_c to 2.29 above T_c. The g-factor extracted from the FMAR transmission data shown in Fig. 4.11 using the Bloembergen form of damping was 2.27, and

Fig. 4.9: Calculated permeability (at 24 GHz) of nickel vs. magnetic field applied in the perpendicular configuration. The low field zero crossing of the real part of the permeability characterizes FMAR. The real part of the permeability is 1.0 at FMR. A Landau-Lifshitz damping of $2.45 \times 10^{8} sec^{-1}$ and a Curie temperature of 354°C were used in the calculation.

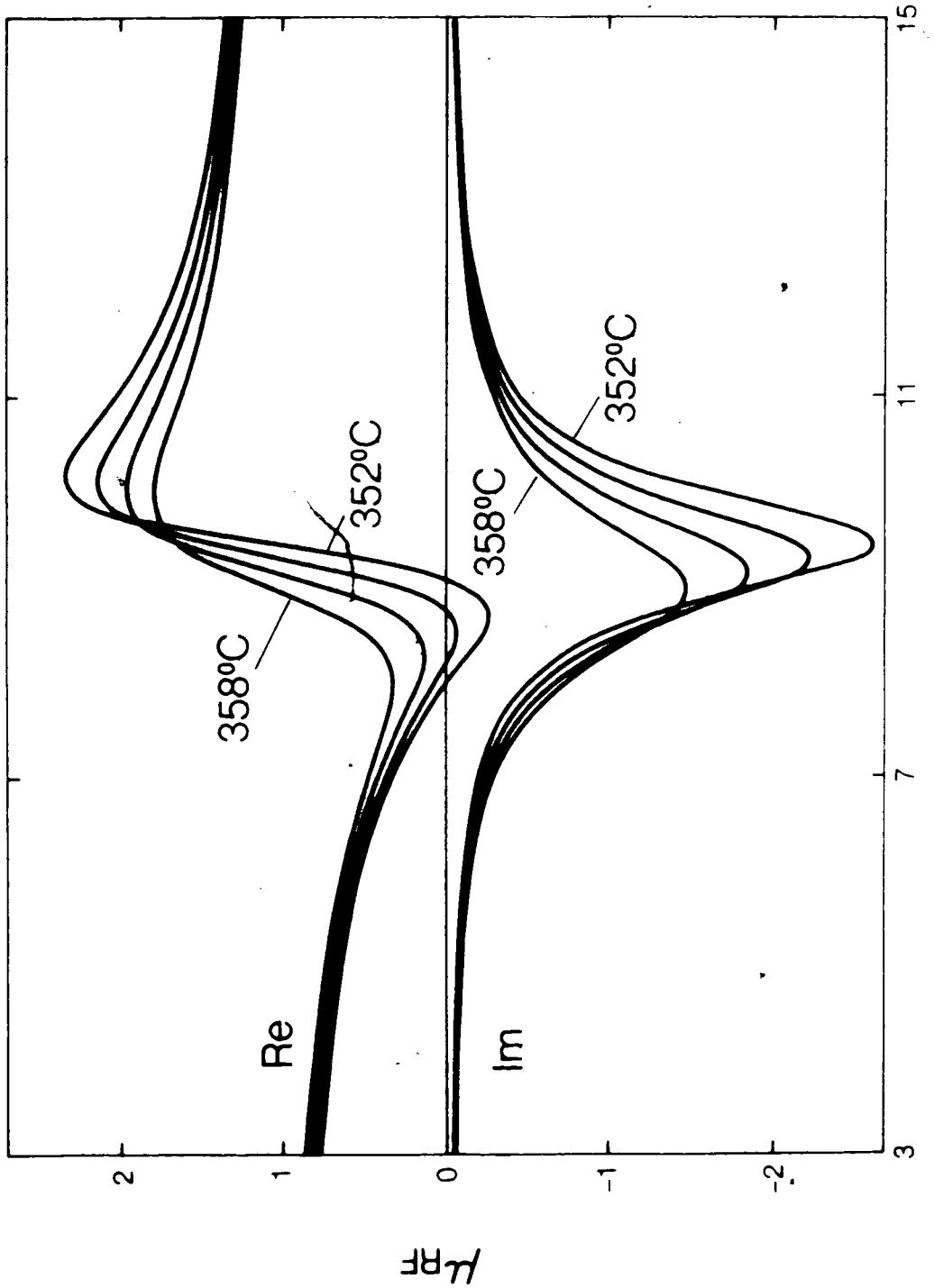

Fig. 4.9

Fig. 4.10: Transmission amplitude as a function of magnetic field for the 18 mm sample in the parallel configuration. Dotted symbols represent the experimentally measured transmission amplitude. The data were taken at 364°C. The scale for the transmission amplitude refers to the longitudinal RF magnetic field for the $TE_{1,0}$ mode of the waveguide. The calculated transmission curves (solid lines) have been normalized to an RF magnetic field amplitude for 3.24×10^{-9} oe. This corresponds to a detected power of 6.9×10^{-16} watts. A resistivity of 29.6×10^{-6} watts. A resistivity of 29.6×10^{-6} Ωcm was used in these calculations. Curve (a) is the calculated transmission for $\lambda = 2.3 \times 10^{8} sec^{-1}$ and $g = 2.20$. Curves (b), (c) and (d) have had a vector baseline subtracted equal to the transmission at 11 kOe. Parameters are: (b) $\lambda = 2.1 \times 10^{8} sec^{-1}$, $g = 2.21$; (c) $\lambda = 2.3 \times 10^{8} sec^{-1}$, $g = 2.20$; (d) $\lambda = 2.5 \times 10^{8} sec^{-1}$, $g = 2.19$.

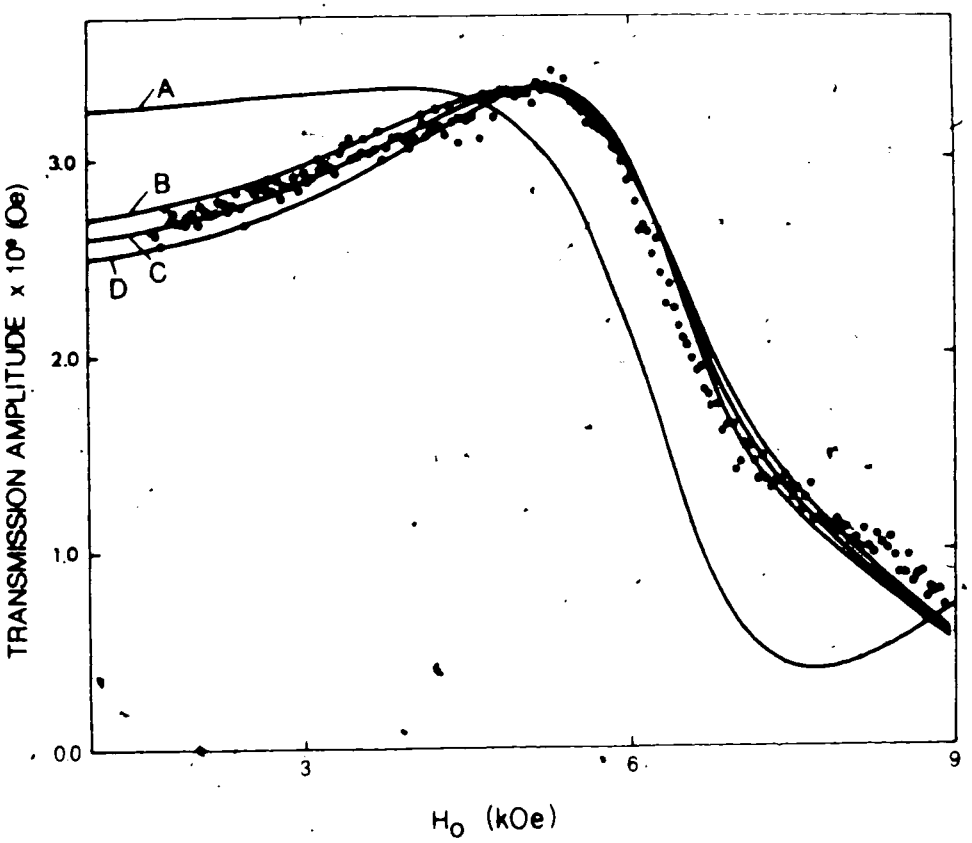

Fig. 4.10

Fig. 4.11: Transmission amplitude as a function of magnetic field for the 18 mm sample in the perpendicular configuration. The data were taken at 364°C. The scale for the transmission amplitude refers to the longitudinal RF magnetic field for the $TE_{1,0}$ mode of the waveguide. Calculated curves have been normalized to an RF magnetic field amplitude of 2.38×10^{-9} oe. This corresponds to a detected power of 3.7×10^{-16} watts. A resistivity of 29.6×10^{-6} Ωcm was used in these calculations. Curve (a) is the calculated transmission for $\lambda = 2.3 \times 10^{8} sec^{-1}$ and $g = 2.20$. Curves (b), (c) and (d) have had a vector baseline subtracted equal to the transmission at 11 kOe. Parameters are: (b) $\lambda = 2.1 \times 10^{8} sec^{-1}$, $g = 2.21$; (c) $\lambda = 2.3 \times 10^{8} sec^{-1}$, $g = 2.20$; (d) $\lambda = 2.5 \times 10^{8} sec^{-1}$, $g = 2.19$.

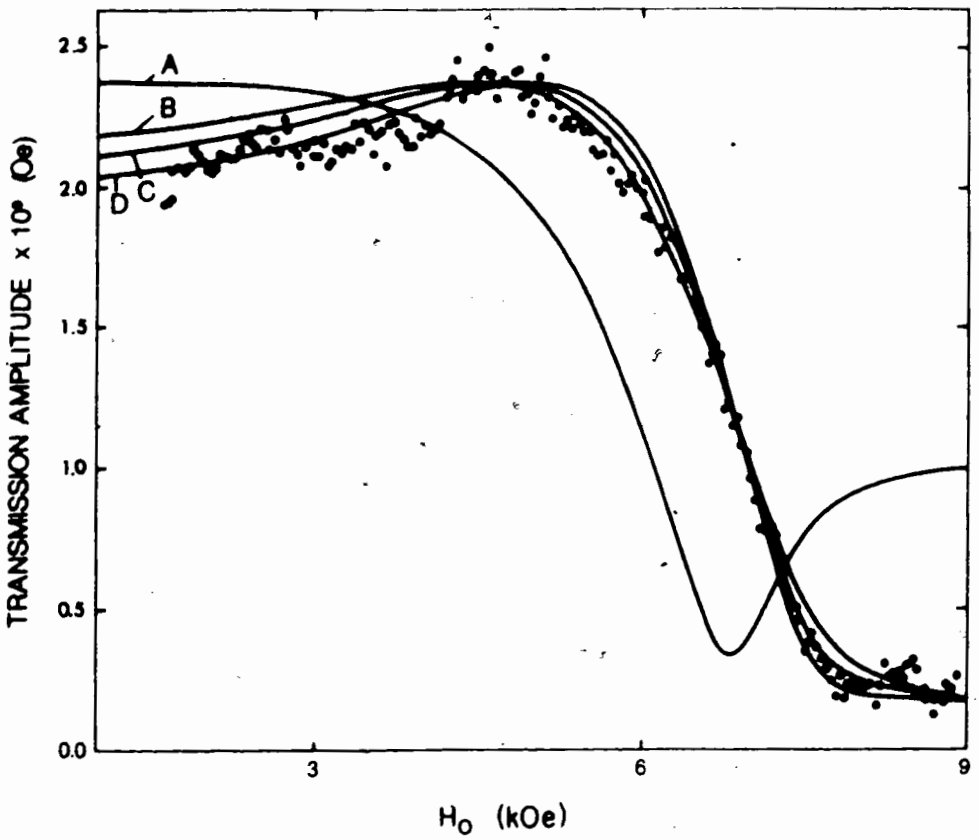
TRANSMISSION AMPLITUDE x 10⁶ (Oe)
2.5
2.0
1.5
1.0
0.5
0.0
A
B
C
D
3
6
9
H₀ (kOe)

Fig. 4.11

using the Gilbert form of damping was 2.30. This was a marked increase over the value found for the g-factor at temperatures less than T_c[11]. However, the g-factor extracted from the experimental data using the Landau-Lifshitz damping parameter was essentially the same at 364°C (g = 2.20) as it was below T_c. Thus the determination of the g-factor from the data collected above T_c was clearly dependent upon the form of damping used in the equation of motion for the magnetization.

The result that the g-factor obtained using the Landau-Lifshitz damping term in the equation of motion for the magnetization was temperature independent over the range 30°C to 364°C is the simplest description of the g-factor extracted from the FMAR transmission measurements reported here. This result, taken with the result that the Landau-Lifshitz damping parameter is also constant over this temperature range, suggests that the band structure which determines the g-factor is also temperature independent over this temperature range.

---

[11] Stress effects were not taken into account above T_c. The magnetostriction constant at these temperatures varied appreciably with applied magnetic field. In any case the shifts in the apparent g-factor caused by magnetostrictive effects were of the order of the uncertainty in the g-factor.

4.3e Results: Magnetization

The magnetization for the 18 mm sample above 100°C was determined both with and without taking magnetostrictive effects into account. These magnetizations are plotted in Fig. 4.12. Open symbols are for magnetizations determined without considering stress effects; filled symbols are for magnetizations found by including stress effects. The solid line in Fig. 4.12 is the magnetization of nickel, at the appropriate internal field, interpolated from the data of Weiss and Forrer (1926). It is clear that the inclusion of stress effects improves the agreement between values for the magnetization of our 18 mm sample and the magnetization for the specimen of Weiss and Forrer. The fact that the magnetization found for the 18 mm sample falls below the magnetization curve interpolated from the data of Weiss and Forrer is characteristic of alloyed nickel.

It was possible to find a set of parameters in the equation of state for nickel appropriate for the 18 mm sample used in the transmission experiments rather than for that of the nickel used by Arrott and Noakes (1967) and Weiss and Forrer (1926). The experimental data in the inset of Fig. 4.12 represent the magnetizations required to fit the calculated positions of the transmission curves to the experimental ones. The temperatures on the graph were measured using the thermocouple attached to the cavities. The experimental value of the Curie temperature, found from

Fig. 4.12: Magnetization of the 18 mm sample as a function of temperature. The sample was heated from 30° to 364°C and then cooled. Open symbols show the magnetization for this cycle found by neglecting stress effects. The filled symbols indicate the magnetization found when the stress effects were taken into account. The solid line is the magnetization, at the appropriate internal field, interpolated from the data of Weiss and Forrer (1926). Above 330°C the magnetization of Weiss and Forrer is identical with the magnetization given by the Arrott and Noakes equation of state for nickel, Equation (4.2) with T_c = 354°C, T_1 = 0.309°C, M_1 = 39.5 G, δ = 1.31, and β = 0.3864. The dashed line in the inset is from Equation (4.2) with a lower value of M_1, i.e. M_1 = 37.0 G, and T_c, T_1, δ, β as above.

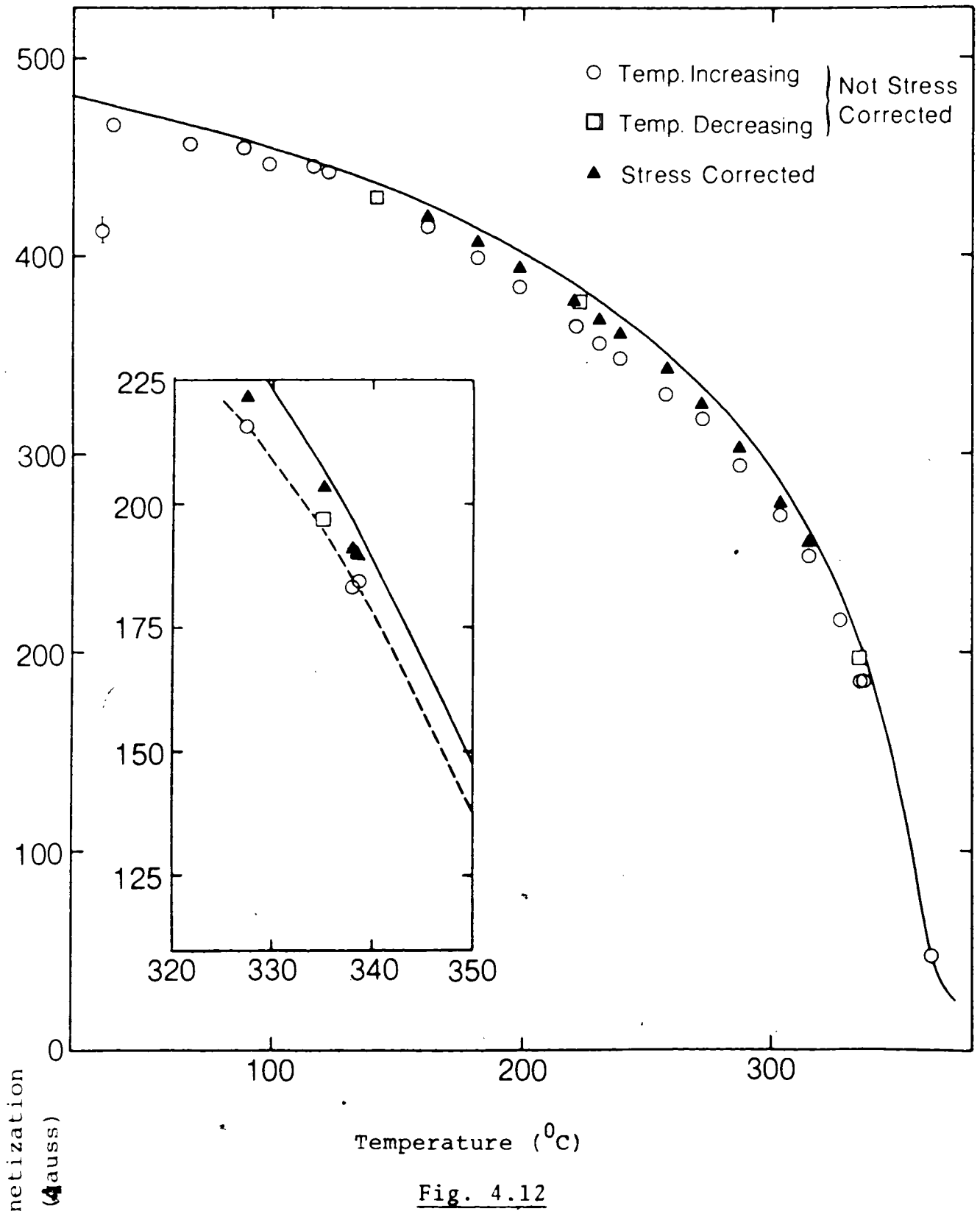
Temp. Increasing
Temp. Decreasing
Not Stress Corrected
Stress Corrected
500
400
300
200
100
0
100
200
300
225
200
175
150
125
320
330
340
350
Magnetization (Gauss)
Temperature (°C)

Fig. 4.12

resistivity measurements, coincided with the T_c of 354°C obtained by Weiss and Forrer. Equation (4.2) can be fitted to this data by taking the critical exponents and T_1 to be fixed at the Arrott and Noakes values and by altering M_1 to fit the data. The dashed curve in Fig. 4.12 was plotted using Equation (4.2) for the appropriate internal field, H, and T_c = 354°C, T_1 = 0.309°C, and M_1 = 37.0 gauss. A similar curve with M_1 = 38.5 gauss would fit the data with strain effects taken into account. (The solid line in the inset of Fig. 4.12 is interpolated from the data of Weiss and Forrer and is identical to Equation (4.2) plotted with the Arrott and Noakes values for T_1 and M_1.) The transmission data for the 18 mm sample at each temperature near T_c were refitted using the value of M_1 appropriate to our sample, i.e. the g-factor, damping parameter, and magnetization were found self-consistently. It is these results which are plotted in Figs. 4.10 and 4.11 and quoted in Table 4.2.

The results for the magnetization of the 18 mm sample are not in themselves remarkable. However, the smoothness of the temperature dependence of the stress corrected magnetization is evidence that the magnetostrictive effects have been adequately described. This lends confidence to the results obtained for the g-factor.

Chapter 5

NICKEL SINGLE CRYSTAL MEASUREMENTS

Microwave transmission measurements were made on nickel single crystals in the temperature range 4K to 300K. These measurements were motivated by the desire to determine the variation of the magnetic damping parameter over the temperature range which Bhagat and Hirst (1966) observed the damping to increase by a factor of six. As stated in Chapter 1, the interpretation of the FMR experiment of Bhagat and Hirst was complicated by the onset of the anomalous skin effect régime concurrently with the increase of the damping parameter. The magnetic damping parameter results presented here were obtained over a temperature range for which the usual local conductivity was appropriate. The damping parameter did in fact increase dramatically as the temperature was lowered from room temperature to 120K.

A new peak was observed in the magnetic field dependent microwave transmission through nickel. This peak occurred at an applied magnetic field which corresponded to FMR. The peak was observed only at temperatures for which the nickel was in the anomalous skin effect régime. Additionally, a significant magnetic field independent microwave signal was transmitted through the nickel at the lowest temperature used in these experiments.

This chapter is organized as follows. After a short description of the sample preparation technique some of the

problems involved in low temperature microwave transmission measurements are discussed. Next, transmission measurements from which the magnetic damping between 120K and 300K was obtained are reported and discussed. Finally, the measurements in which the new transmission peak was observed are presented.

5.1 Sample Preparation

Discs were speak cut from a nickel single crystal[1] with the [100] axis normal to the plane of the disc. These discs were approximately 1 cm in diameter and between 300μm and 400μm thick. The rough surfaces left by the spark cutter were smoothed on a mechanical lapping/polishing apparatus[2]. The finest grade of polish employed was 5μm aluminum oxide grit. After this mechanical polishing stage the discs were 150μm to 200μm thick with shiny, parallel sides.

The final stage of thinning of the discs down to less than 10μm thickness was accomplished by electropolishing the discs in a specially designed electropolishing apparatus. For the details of the electropolishing apparatus and polishing technique see Appendix IV. The final discs were 3μm to 8μm thick and 4 mm to 7 mm in diameter. Judging from the rate at which the sample diameter decreased with decreasing thickness in the final stages of electropolishing, the central portion of the best samples were uniform in thickness to approximately 1μm.

Each sample disc was soldered with indium over a 2.0 mm diameter hole in a gold plated nickel diaphragm. Details of how samples with diaphragms were incorporated into the micro-

---

[1]The measured residual resistivity ratio for the single crystal was 300 ± 50. This is a lower bound to the intrinsic residual resistivity ratio since no magnetic field was applied to the crystal to align the magnetization parallel to the current

[2]CTF Systems, Inc., 1750 McLean Street, Port Coquitlam, B.C.

wave cavity system are given in Chapter 3. Throughout the electropolishing process and after the final mounting of the samples, X-ray photographs were made to check the quality and orientation of the samples.

Nickel was used as a diaphragm material to eliminate thermal strains between the sample and the diaphragm. If a material such as copper were used the differential thermal contraction between the nickel and copper would have either buckled the sample or introduced an effective magnetostrictive field of $\approx 10^2$ gauss. The nickel diaphragms did introduce a slightly nonuniform demagnetizing field (see below) but this was tolerable.

Indium was used as the solder because the indium was soft enough that even upon cooling to 4K the sample was not strained by the solder.

The diaphragms were 25 mm diameter circular discs cut from 125 μm thick nickel foil. After mounting holes and a central diameter hole were drilled into the diaphragm (see Fig. 5.1), the diaphragms were mechanically polished to a thickness of approximately 80 μm thickness and annealed at 1000°C for one hour. These smooth, flat diaphragms were then covered with a 2 μm to 3 μm thick layer of evaporated gold. The gold surface prevented spurious magnetic field dependent absorption of microwaves by the nickel diaphragm for fields corresponding to FMR.

Two major problems involving sample preparation for the

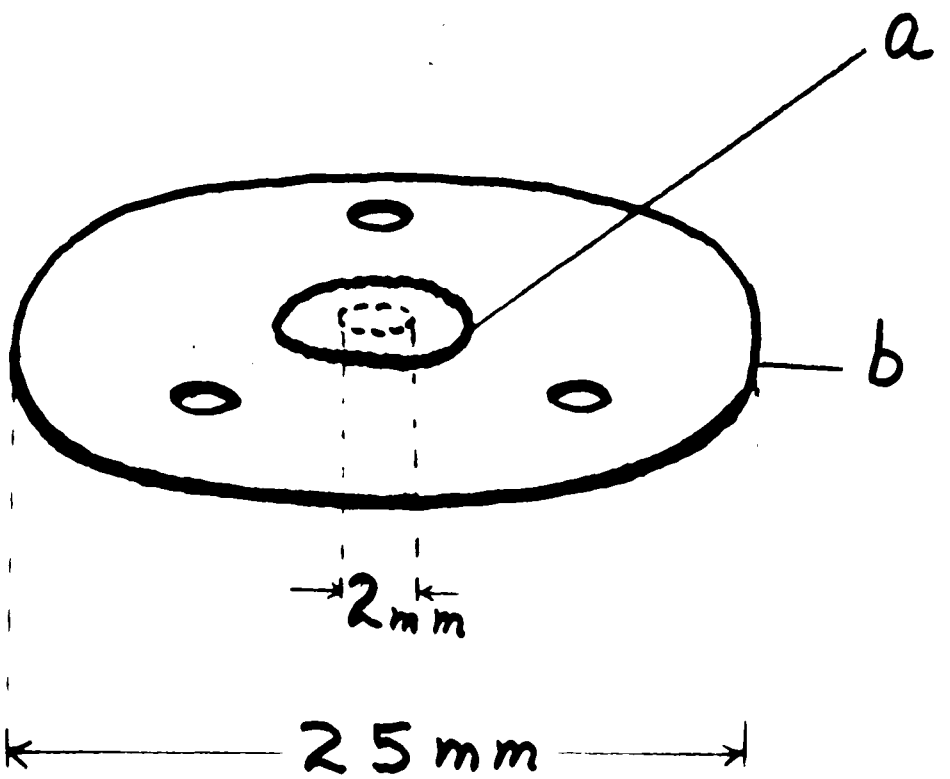

Fig. 5.1: Sample and diaphragm. The nickel sample (a) is soldered with indium onto the diaphragm (b). The sample is centred over a 2 mm diameter hole in the diaphragm.

transmission experiments were encountered. First, the only directions of high symmetry in the plane of the sample were the [100] and [110] directions. These are the "hard" and "intermediate" directions of the magnetization with respect to the magnetocrystalline anisotropy. At low temperatures the anisotropy was so large that the samples wrinkled in an applied magnetic field. This problem could have been overcome by cutting the crystals with the [110] direction normal to the plane of the sample discs. For such an orientation the [111] or "easy" direction of magnetization, as well as the [100] and [110] directions, would have been in the plane of the samples. The samples would not have wrinkled if the magnetic field were applied along the [111] direction.

The second major problem involved the annealing of the samples as a matter of course to remove any strain which may have been produced in handling. The annealing process was carried out in a vacuum of $\approx 10^{-6}$ torr. This was an insufficiently good vacuum to prevent contamination of the samples. An annealed nickel single crystal sample disc was found to have a residual resistivity ratio of less than 15. This problem was eliminated by the simple expedient of omitting the annealing step in the sample preparation procedure and by taking great care in handling the samples.

5.2 Transmission Experiments

The beryllium-copper microwave cavities employed in these nickel single crystal experiments were constructed in such a manner that the sample plus diaphragm constituted the common end-wall of the transmitter and receiver cavities (see Chapter 3). The applied magnetic field could be rotated to any direction in the plane of the sample. Once the sample was mounted in the microwave cavity system the direction of the radio frequency magnetic field was fixed with respect to the crystalline axes of the sample.

Extensive transmission experiments were carried out on a total of four nickel single crystal samples between 4K and 300K. The microwave cavity assembly was enclosed in a stainless steel dewar described by Lyall (1970). The temperature of the cavities and sample was monitored by a copper constantan thermocouple which was calibrated at the boiling points of nitrogen and helium. The temperature of the sample was usually stable to about $\pm$ 1K during the time interval required for a transmission measurement. The stability was poorer in the temperature range 5K to 25K because the heat capacity of the cavities was small at these temperatures and approximately 150 MW of microwave power was incident upon the cavities. For example, the sample temperature increased 5K during the course of a transmission measurement near 20K.

5.3 Results: 77K to 300K

a) Sample Characterization

The best of the unannealed samples, Ni8μ, was used to deduce the temperature dependent value of the magnetic damping at low temperatures. Extensive room temperature (305K) transmission measurements were made on this sample to determine its physical parameters. The calculation which was compared to the experimental data required the specification of two anisotropy constants, the g-factor, the magnetization, the magnetic damping, the resistivity, and the thickness of the sample. Not all of these parameters could be determined directly from the data.

The magnetic field at which the peak transmission occurred depended on the two anisotropy constants, the g-factor, and the magnetization. Only two peak positions were readily available from experiment: the peak transmission field obtained with the magnetization parallel to the [100] axis and with the magnetization parallel to the [110] axis. One anisotropy constant, K_1, was taken from the data of Okamoto (1966) and the magnetization was taken from the data of Aldred (1975). The second anisotropy constant, K_2, and the g-factor were obtained by comparing the calculated peak transmission fields with the experimental data. The value of K_2 which best described the data was $(4.5 \pm 2.0) \times 10^4$ ergs/cm^2. The g-factor found for Ni8μ was 2.2 ± .1, close to the value 2.187 ± .005 deduced from transmission data on

polycrystalline samples. The parameters used in the calculation are listed in Table 5.1. Of course other choices for K_1 and magnetization would lead to different values for K_2 and the g-factor[3]. This, as well as the fact that the nickel diaphragm introduced a demagnetizing field of approximately 135 gauss which was uniform to about 25 to 30 gauss over the area of the sample, accounts for the liberal errors associated with K_2 and the g-factor found for Ni8μ.

The lineshape of the calculated transmission vs. applied magnetic field was dependent on the magnetic damping, the resistivity, and the sample thickness used in the calculation. The resistivity was taken from the data of White and Woods (1959) and the Landau-Lifshitz damping parameter was taken to be 2.45×10^8 sec^{-1} as found from previous experiments on polycrystalline nickel samples. The precise lineshape was not critically dependent on the value of the damping parameter employed in the calculation. This is because the sample was so thin that a small change in the damping would alter the amount of power absorbed within the sample only slightly. Changing the thickness (or resistivity) used in the calculation has a more direct influence on the calculated power absorbed within the sample. The sensitivity of the lineshape to thickness is illustrated in Fig. 5.2. The agreement between

---

[3]Alternatively, one could have used Aldred's value for the magnetization and taken g=2.187 as found in Chapter 4. Then the positions of the peak transmission along the [100] and [110] directions require that $K_1 = -4.5 \times 10^4$ ergs/cm^2 and $K_2 = 6.6 \times 10^4$ ergs/cm^2 at 305°K.

Table 5.1

Parameters used in transmission calculations for comparison with Ni8μ room temperature (305K) measurements.

f	R.F. frequency	24.032 GHz
g	g-factor	2.199
M_o	magnetization	485 gauss
K_1	1st anisotropy constant	-5.56×10^4 ergs/cm^2
K_2	2nd anisotropy constant	4.5×10^4 ergs/cm^2
ρ	resistivity	7.41×10^{-6} Ω-cm
d	thickness	8.0×10^{-4} cm
λ	damping	2.45×10^8 sec^{-1}

Fig. 5.2: Transmission amplitude vs. applied magnetic field for Ni8μ. The data (+) were taken at 305K with the magnetic field along the [100] direction. The calculated transmission (solid lines) is normalized to the experimental peak amplitude. The three curves are for thicknesses 7.7μm (broadest curve), 8.0μm, and 8.3μm (narrowest curve). Other parameters are f = 24.032 GHz, g = 2.199, M_o = 485G, $K_1 = -5.56 \times 10^{-4}$ ergs/cm^2, $K_2 = 4.5 \times 10^4$ ergs/cm^2, $\lambda = 2.45 \times 10^8$ sec^{-1}, resistivity = 7.41×10^{-6} -cm, D_{zz} = 1.04, and D_{xx} = -0.02.

Fig. 5.2

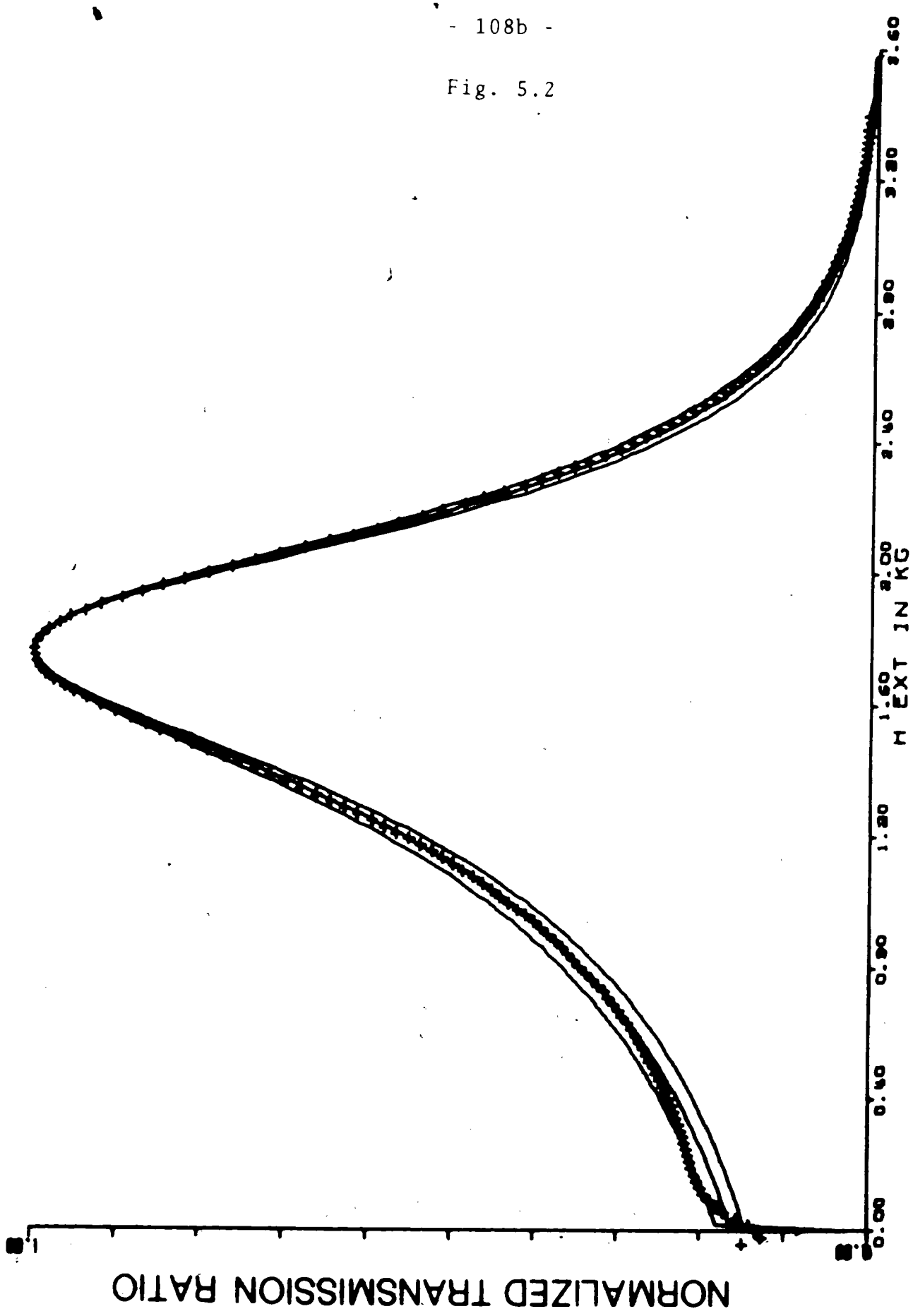
NORMALIZED TRANSMISSION RATIO
H EXT IN KG
0.00
0.40
0.80
1.20
1.60
2.00
2.40
2.80
3.60

the experimental data and the calculation for a sample of 8.0μ thickness is quite good. (The calculation cannot be expected to agree with the data for an applied field of 0.3kG or less because the magnetocrystalline anisotropy is of this order of magnitude. For small magnetic fields the magnetization is not parallel to the applied field as the calculation assumes.)

From the transmission data the central portion of Ni8μ exposed to microwaves was determined to be 8.0 ± .3μ. The thickness determined from the weight, area, and density of Ni8μ was 6.5 ± 1μ. This latter value underestimated the thickness of the central portion of the sample because the sample is shaped like a convex lens. Hence, these two values for the thickness are consistent.

(b) Damping parameter

Extraction of the magnetic damping parameter from the transmission data was complicated by the wrinkling of the sample. (See Section 5.1.) The damping could not be found by fitting the transmission lineshapes because the effect of the wrinkling of the specimen was to broaden the transmission peak. This imitated the effect of an increased damping. After the sample wrinkled the calculation could not be made to fit even the room temperature experimental data. However, the peak amplitude of the transmitted signal at room temperature was changed little by this wrinkling of the sample. The peak

transmitted amplitude found with the magnetization along the [100], or hard, axis decreased about 5% after wrinkling and the peak amplitude with the magnetization along the [110], or intermediate, axis increased about 5%. Comparison of the peak transmitted amplitude at room temperature with the peak amplitudes at lower temperatures enabled the damping to be extracted from the data with an accuracy of $\pm$ 0.3 $\times$ $10^8 sec^{-1}$ for temperatures near room temperature and with an accuracy of $\pm$ 0.5 $\times$ $10^8 sec^{-1}$ at 120K. The primary uncertainties involved in obtaining the damping in this manner were:

a) uncertainty of $\pm$ 0.1 $\times$ $10^8 sec^{-1}$ in room temperature damping of 2.45 $\times$ $10^8 sec^{-1}$.

b) uncertainty of $\pm$ .3μm in sample thickness of 8.0μm.

c) uncertainty of $\pm$ 3K in temperature measurement.

d) uncertainty in the temperature dependence of the cavity Q-factor resulted in an uncertainty in the transmitted amplitude of $< 5\%$.

e) uncertainty in the effect of wrinkling of the sample resulted in an uncertainty in the transmitted amplitude $\leq 10\%$.

f) system reproducibility introduced an uncertainty in the transmitted amplitude $\lesssim 5\%$.

These uncertainties were not severe since the transmission amplitude is a strong function of the damping. The transmission amplitude varies approximately as

$\exp[-kd] \propto \exp[-\lambda^{1/2}]$. Thus any small change in the damping results in a large change in the transmission. For example, at 125K a change of the damping from $\lambda = 2.4 \times 10^8 sec^{-1}$ to $\lambda = 5.0 \times 10^8 sec^{-1}$ results in a change of over an order of magnitude in the transmission amplitude calculated for an 8.0μm sample.

The Landau-Lifshitz damping parameter obtained from the analysis of the peak transmission amplitude is displayed in Fig. 5.3. At 115K the signal transmitted through Ni8 was less than the noise level of the detection system. The noise power level was 168 db below the incident power level[4].

Data for two different directions of the magnetization and for two cooling cycles on Ni8μ are included. The solid line indicates the damping deduced from ferromagnetic resonance experiments carried out by Bhagat and Hirst (1966).

---

[4]The system time constant was 3.5 sec.

Fig. 5.3: Landau-Lifshitz damping parameter vs. temperature for Ni8μ. The damping parameter was extracted from transmission measurements made with the applied magnetic field along the [100] direction (■) and along the [110] direction (0). A typical error bar is shown at the upper right. The solid line is interpolated from the FMR data of Bhagat and Hirst (1966).

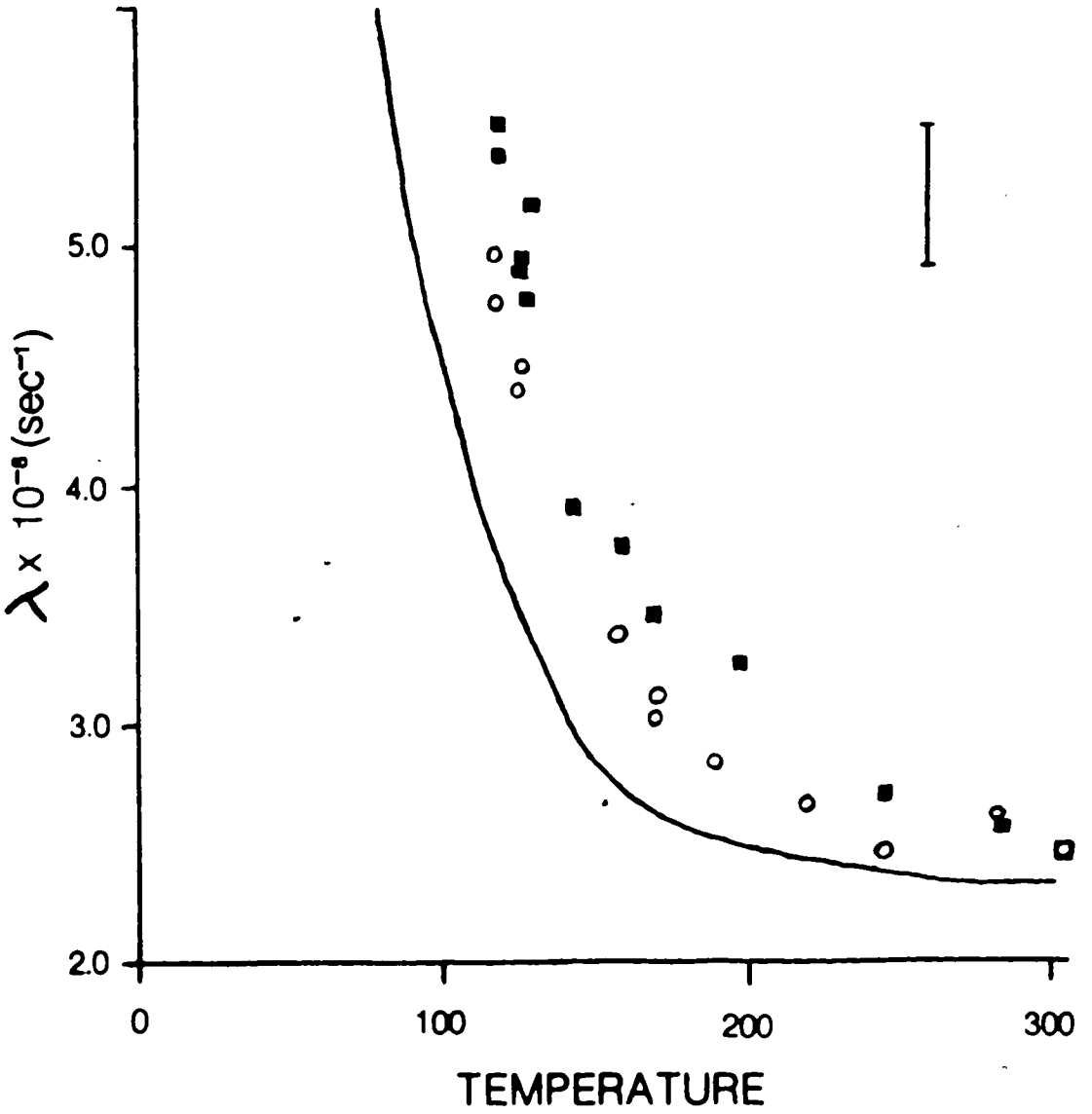

Fig. 5.3

5.4 Discussion of Results: 77K to 300K

Figure 5.3 provides a convenient point of departure to discuss the results of the previous section in comparison with the results obtained by Bhagat and Hirst (1966). The calculation used by Bhagat and Hirst to extract the damping from their data was complicated by the fact that the conductivity of nickel is in the anomalous régime at FMR for temperatures which coincide with the increase of the damping parameter. At FMR the radiation which enters the sample is absorbed in a shorter distance than is normally associated with an electromagnetic wave in a material of the same conductivity. This is a direct result of the large permeability at FMR decreasing the effective skin depth. This decay length of the radiation is comparable to the mean free path of the conduction electrons. For example, the scaling length is $\delta \approx 3 \times 10^{-5}$cm at 120K and it is effectively shortened a factor of 3 to 5 at FMR by the large permeability. The electron mean free path is[5] $\approx 10^{-5}$cm at 120K. In this regime Ohm's law is not valid. To describe the electric field-current relation one has to calculate the current density by considering the electric field each electron passing through an element of area has experienced since its last collision. See, for example,

---

[5]This mean free path, ℓ_{120K}, was calculated from the relation $\ell_{120K} = \left(\sigma_{120K}/\sigma_{273K}\right) \ell_{273K}$, when $\ell_{273K} = 2.66 \times 10^{-6}$cm (Mott and Jones 1936).

Pippard (1965). In the experiment described here the decay length of the electromagnetic radiation passing through the sample is enhanced at FMAR. (See Chapter 2.) Thus the characteristic length associated with the radiation is long compared witn an electron mean free path at the temperature of the onset of the increased damping in nickel, and for temperatures somewhat below as well. For instance, at 120K the characteristic length of the electromagnetic radiation at FMAR $\approx 10^{-4}$cm for a damping of 5×10^{8}sec^{-1} and the electron mean free path is approximately 10^{-5}cm. The results of the previous section show unambiguously that the low temperature magnetic damping does indeed increase dramatically over the room temperature value.

It is apparent from Fig. 5.3 that the magnetic damping found here increased more rapidly with decreasing temperature than did the damping found by Bhagat and Hirst. This fact is predicted by a calculation of magnetic damping made by Korenman and Pragne (1972) using a mechanism originally suggested by Kambersky (1970). Kambersky's idea was that the space and time variation of the magnetization, through the spin-orbit interaction, produced a periodic modulation of the fermi surface. Scattering allowed the electrons to follow the modulation of the fermi surface and to damp the spin wave. Nickel's band structure is such that there are certain parts of the fermi surface which are strongly spin-orbit dependent (Gold 1973). Korenman and Pragne extended this idea to the case in which the scattering time was long

enough that an electron moving at the fermi velocity travelled a distance comparable to a wavelength of the magnetic disturbance between collisions, i.e. they extended the theory to the anomalous damping limit.

According to Korenman and Pragne,

$$\lambda \propto \frac{\tan^{-1}(kv_f\tau)}{kv_f} \qquad (5.1)$$

Here k is the propagation constant of the wave inside the ferromagnetic metal, v_f is the fermi velocity, and τ is the scattering time for the electrons. At high temperatures the scattering time is short and $kv_f\tau << 1$ for the usual range of k's encountered in FMR or FMAR experiments. Then

$$\lambda \propto \tau \qquad (5.2)$$

The scattering time, and hence the damping, can be expected to vary with temperature in the same manner as the conductivity. Therefore, this theory cannot account for the large, temperature independent damping present in nickel. Korenman and Pragne proposed that this theory did account for the additional low temperature damping observed by Bhagat and Hirst.

Applying equation (5.1) to the case at hand, we can expand the inverse tangent in a power series and examine the theoretical damping appropriate to the experiment described in this thesis and compare it with the theoretical damping for the FMR experiment of Bhagat and Hirst. The theoretical damping is

of the form

$$\lambda \propto \tau - \frac{k^2 v_f^2 \tau^3}{3} \cdots \qquad (5.3)$$

where we are restricted to the case in which $kv_f\tau < 1$.

There are differences between this experiment and the experiment of Bhagat and Hirst which enter into equation (5.3). First, this experiment was carried out at 24GHz whereas Bhagat and Hirst's experiment was done at 9GHz. Second, this experiment produced results appropriate to FMAR; Bhagat and Hirst's experiment was appropriate to FMR. Combining these facts, the characteristic k at the onset of the increased damping for this experiment was $\approx 1/15$ of the k associated with Bhagat and Hirst's experiment. Therefore, Korenman and Pragne's theory predicts that as the temperature is decreased, the damping in this experiment will begin to increase at a higher temperature, i.e. smaller τ, than in the experiment of Bhagat and Hirst. This is indeed the case. Thus, this experiment confirms the results of Bhagat and Hirst and adds additional support to the theory of Korenman and Pragne.

5.5 Results: 4K to 77K

a) Sample characterization

The thinnest sample available, Ni3μ, was used to investigate the characteristics of the radiation transmitted through nickel at and below liquid nitrogen temperature. Inspection of Ni3μ under a microscope revealed that this sample was noticeably thicker on one edge. It was also smaller than most samples, being an ellipse of approximately 5mm by 3mm. The sample was soldered onto a gold plated nickel diaphragm with the thick edge not exposed to microwaves but the non-uniformity of this sample's thickness was apparent in the room temperature transmission experiment. Fig. 5.4 illustrates the improvement in the fit of the calculated transmission to the data obtained by combining two thicknesses in the calculation over the fit obtained by using one thickness. Fig. 5.5 shows the transmission for thicknesses of 2.8μm and 4.2μm separately as well as their sum. Clearly, the transmission at high fields, near the position of FMR, is due almost entirely to the thinner areas of the sample while the thick areas only contribute to the transmission near the peak. This accounts for the differences between the calculated transmission for a single thickness of sample and the experimental data shown in Fig. 5.4. The calculated transmission curve is too broad near the peak and too low at high fields. Of course, a weighted average of several thicknesses would produce a better fit to the data than the simple calculation using only two thicknesses as shown in Fig. 5.4.

Fig. 5.4: Transmission amplitude vs. applied magnetic field for Ni3μ. The data (+) were taken at 298K with the magnetic field along the [100] direction. The transmission curve indicated with an arrow was calculated using a thickness of 3.5μm. The other curve not so marked is the sum of two equally weighted calculated transmissions, one for 4.2μm thickness and one for 2.8μm thickness. The calculations were made with R.F. frequency = 24.032 GHz, g = 2.20, $4\pi M_o$ = 6.128 KG, resistivity = 7.2×10^{-6} Ω-cm, $K_1 = 5.56 \times 10^4$ ergs/cm^2, and $\lambda = 2.4 \times 10^8 sec^{-1}$.

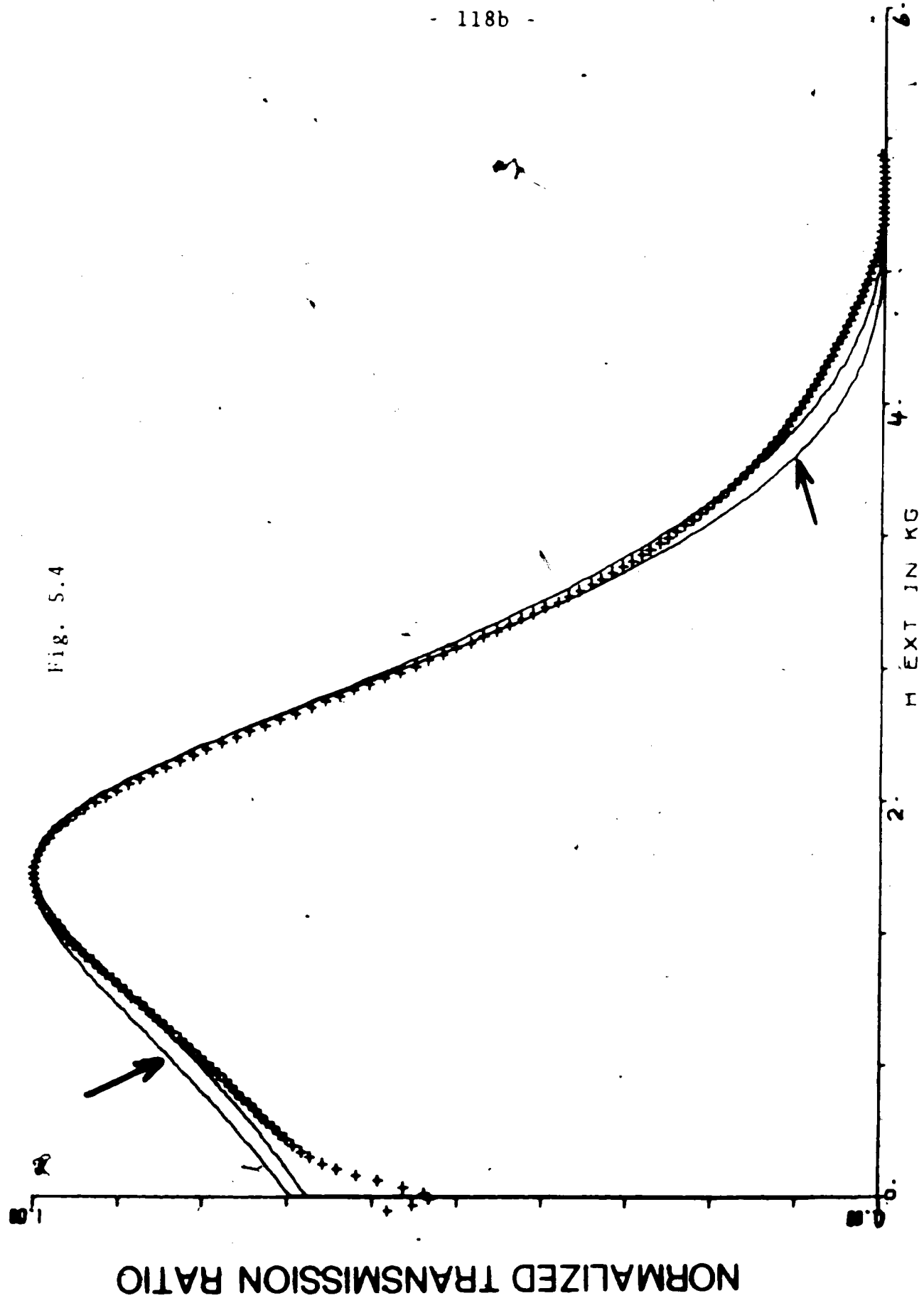

Fig. 5.4

Fig. 5.5: Calculated transmission amplitude vs. applied magnetic field for 4.2μm (A) and 2.8μm (B). Curve C is the sum of curves A and B. Other parameters used in the calculation are the same as for Fig. 5.4.

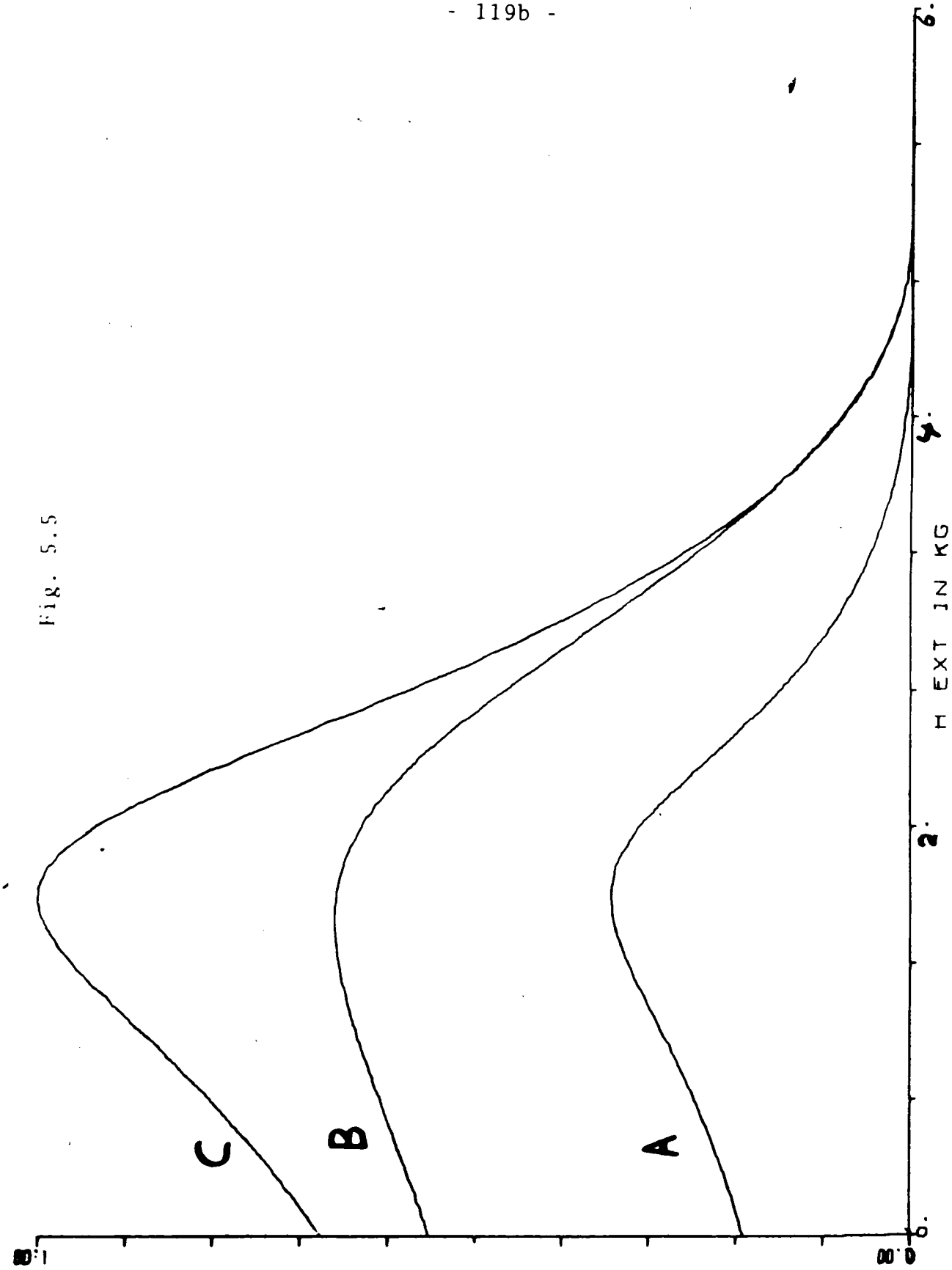

Fig. 5.5

Unfortunately, this non-uniformity of the thickness of Ni3μ precluded any estimation of the damping parameter from the peak amplitude of the transmitted signal. As the temperature was lowered the thinner areas of the sample would be expected to transmit an increased fraction of the total signal, i.e. the thickness of the sample would apparently decrease with temperature. Also, since the sample was very thin, the calculated amplitude was not as sensitive to the damping as it was for Ni8μ. This non-uniformity of the thickness as well as the wrinkling of the sample meant that only qualitative statements could be made about the low temperature transmission of microwaves through nickel.

b) The new transmission peak

The experimental transmission data for Ni3μ at various temperatures is shown in Fig. 5.6. The data were taken with the external field parallel to the [100] crystal axis.

A large peak in the transmitted signal is readily apparent in the measurements made at 4K. This peak occurred at an applied field of 9kG which coincided with FMR in the sample. This new peak was unexpected in that the microwave radiation inside the sample is most heavily attenuated at FMR. Accompanying this peak was a large field independent signal[6].

[6]The zero level for these measurements was determined by closing attenuator DBE 410 in the incident microwave line (see Fig. 3.1) and noting the receiver reading. This method of determining the zero level does not allow for the low level of direct microwave leakage between the transmitter and receiver lines. However, this extraneous signal is less than 5% of the peak transmission at 4K.

Fig. 5.6: Measured transmission amplitude vs. applied magnetic field for Ni3μ at various temperatures. The same (arbitrary) scale has been used to display each set of data. The peak transmission at 4K corresponded to a transmitted power 106 db below the incident power level.

Fig. 5.6 (Part 1)

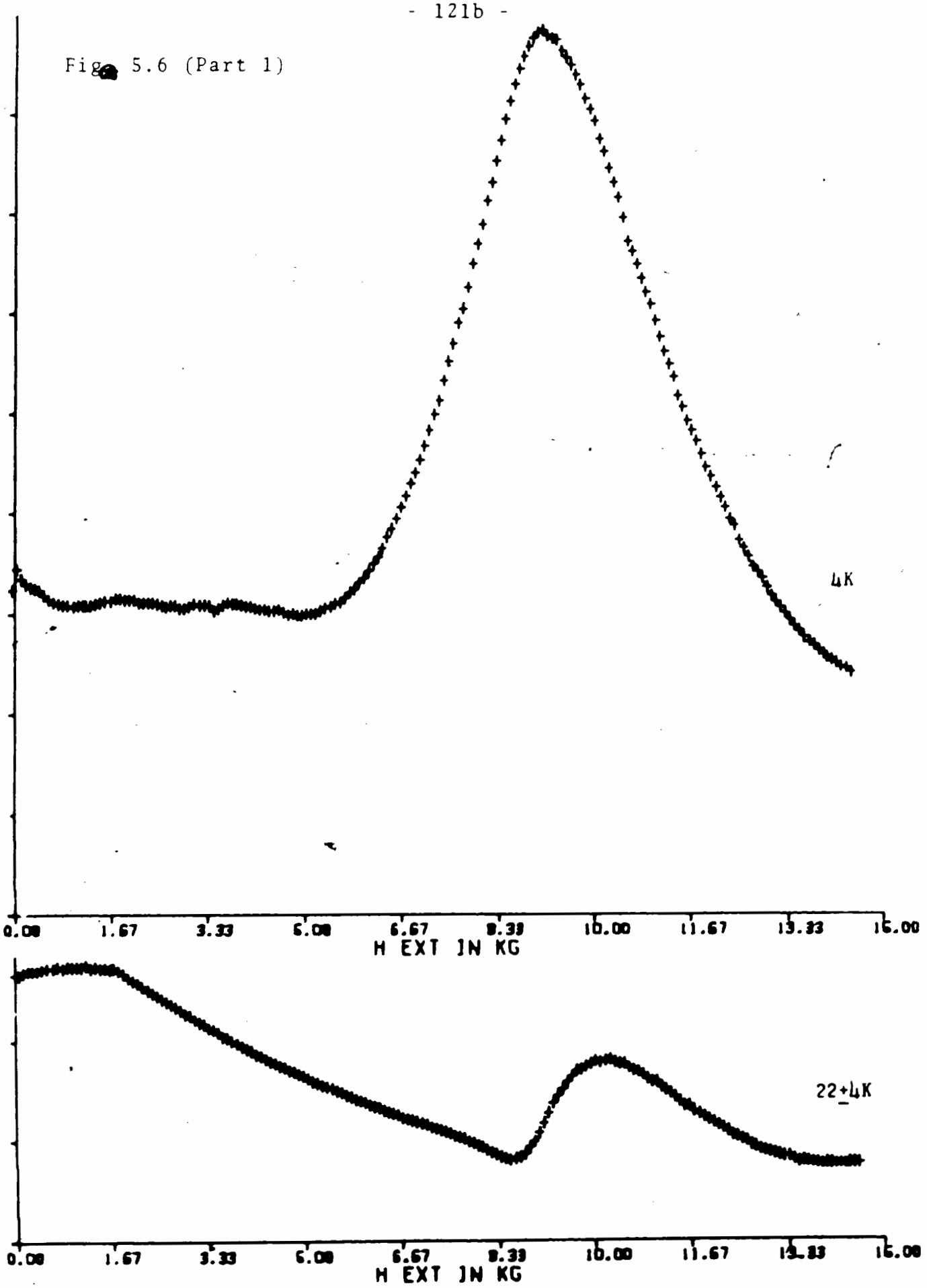
4K
0.00
1.67
3.33
5.00
6.67
8.33
10.00
11.67
13.33
15.00
H EXT IN KG
22±4K
0.00
1.67
3.33
5.00
6.67
8.33
10.00
11.67
13.33
15.00
H EXT IN KG

Fig. 5.6 (Part 2)

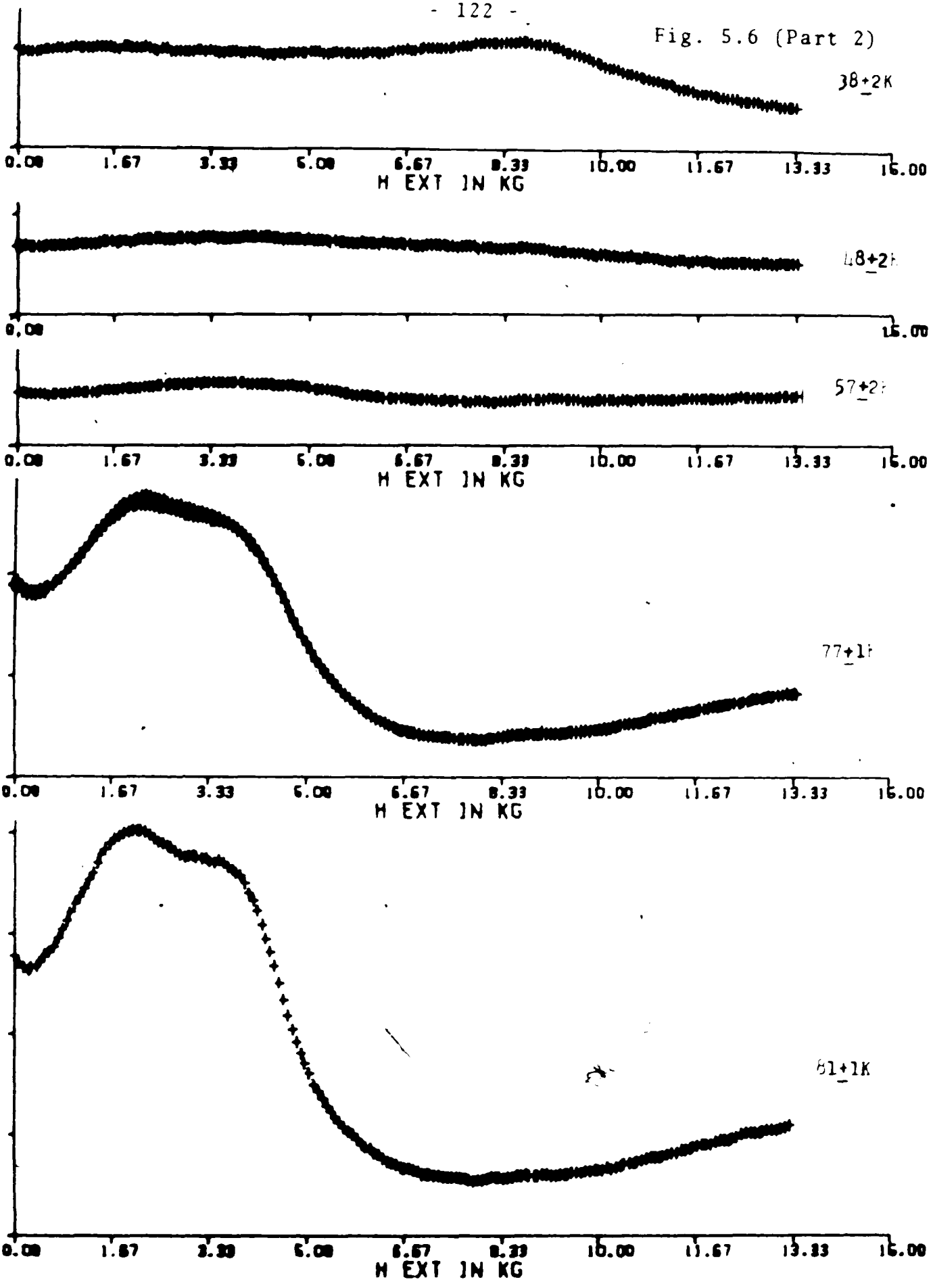
38±2K
0.00
1.67
3.33
5.00
6.67
8.33
10.00
11.67
13.33
15.00
H EXT IN KG
48±2K
0.00
15.00
57±2K
0.00
1.67
3.33
5.00
6.67
8.33
10.00
11.67
13.33
15.00
H EXT IN KG
77±1K
0.00
1.67
3.33
5.00
6.67
8.33
10.00
11.67
13.33
15.00
H EXT IN KG
81±1K
0.00
1.67
3.33
5.00
6.67
8.33
10.00
11.67
13.33
15.00
H EXT IN KG

Note that there is no evidence for a peak at the expected position of FMAR ($\approx$ 4kG).

With increasing temperature the peak at FMR disappeared and the familiar FMAR transmission peak appeared. The field independent signal decreased with increasing temperature. (The apparent field dependence of the transmitted signal between 0 and 8kG for the measurement at $\approx$ 22K was an artifact caused by the rapidly changing temperature of the sample as the measurement was made.) At 77K the FMAR transmission was a double peak. The high field peak was the usual FMAR peak; the low field peak occurred because the applied field was small enough to allow the magnetization to rotate away from the direction of the applied field, under the influence of magnetocrystalline anisotropy and the FMAR condition was satisfied a second time. This phenomena was also noted by Bhagat and Hirst (1966) who reported double FMR absorption maxima in nickel at low temperatures.

5.6 Discussion of Results: 4K to 77K

The detailed explanation of this new transmission peak is not known at present. This peak cannot be explained simply by putting a non-local conductivity into the theory developed in Chapter 2. The mean free path of the electrons, for temperatures less than 40K, is much longer than a wavelength of the microwave radiation at FMR within the nickel. The strong temperature dependence of this new peak between 4K and 30K cannot be due simply to the non-local conductivity because the conductivity at 24GHz changes little over the temperature range. One possibility is that a sound wave is involved in transmitting energy through the sample.

In order to elucidate the nature of this FMR transmission peak it will be necessary to undertake experiments to study the temperature, thickness, and orientation dependence of this peak. Such a programme is beyond the scope of this thesis.

CHAPTER 6

CONCLUSION

The ferromagnetic antiresonant transmission experiments described in this thesis were undertaken for two principal reasons: to determine the magnitude of the temperature independent magnetic damping in nickel as well as the temperature range over which this damping was indeed constant, and to verify the anomalous magnetic damping observed at low temperatures by Bhagat and Hirst (1966).

An analysis of the transmission data employing the Landau-Lifshitz equation of motion for the magnetization indicated that the Landau-Lifshitz damping parameter had the value $\lambda = 2.45 \pm .1 \times 10^8 \text{sec}^{-1}$ between room temperature and 637K (364°C). The g-factor was determined to have the temperature independent value $g = 2.187 \pm .005$ over the same temperature range. It is noteworthy that this temperature range extends beyond the Curie temperature (627K) and that the Landau-Lifshitz equation of motion, together with Maxwell's equations, was adequate to describe the microwave transmission data. This is contrary to the findings of Bhagat and Rothstein (1971) who stated that the usual phenomenological calculations did not describe their ferromagnetic resonance absorption measurements made at temperatures near the Curie temperature.

The temperature independence of the magnetic damping and

g-factor supports the theory of magnetism recently advanced in a series of papers by Korenman and Prange et al. (1977)[1]. Consider first the magnetic damping. According to a theory of L. Berger (to be published) the temperature independent magnetic damping in nickel arises from its complicated band structure. In the earlier band theory of magnetism the static magnetization was proportional to the population difference between the spin-up and spin-down subbands. At the Curie temperature the magnetization disappeared because the populations of the spin-up and spin-down subbands were equalized. The fermi surfaces for the spin-up and spin-down subbands in nickel are quite different (Gold 1973). Thus the earlier band theory of magnetism demanded that the fermi surface of nickel change substantially as the Curie temperature was approached. Provided Berger's proposal that the temperature independent damping in nickel is intimately related to the fermi surface is valid, it can be argued that the observed damping requires that the fermi surface not change near the Curie temperature. This is at variance with the earlier band theory of magnetism. However, an idea central to Prange's band theory of magnetism is that the spin-up and spin-down subbands remain split at the Curie temperature. The observed temperature independence of the magnetic damping supports this idea.

---

[1]I am indebted to A.S. Arrott for pointing out this fact.

The temperature independence of the g-factor also supports the Prange theory. In a calculation of nickel's g-factor, for example in the calculations of Arlinghaus and Reck (1975) or of Singh et al. (1976), the final result is sensitive to how accurately the band structure is parameterized. Thus, if the fermi surface for the spin-up and spin-down subbands were changing with temperature, one would expect the g-factor to change as well. The fact that the g-factor observed in these experiments was temperature independent supports Prange's contention that the spin-up and spin-down subbands remain split at the Curie temperature.

The low temperature transmission results confirmed the large increase in the magnetic damping observed by Bhagat and Hirst. The increase in the damping observed in this experiment set in at a higher temperature than in the experiment of Bhagat and Hirst. This is in agreement with the theory which Korenman and Prange (1972) advanced to explain Bhagat and Hirst's results.

In the temperature range $4K < T < 40K$ a new peak was observed at ferromagnetic resonance in the microwave transmission through nickel. The origin of this peak is not clear. The usual FMAR transmission peak was not observed below 25K but a relatively large, field independent, transmission signal was present.

The FMAR transmission technique proved its value with the experiments described in this thesis. The results were less

dependent on sample preparation than for FMR absorption measurements and sample to sample reproducibility was better than for FMR measurements. For example, the g-factor and damping parameter found using polycrystalline samples were consistent with the results obtained from the single crystal samples. The damping parameter was comparable to that found by Rodbell (1965) on highly perfect single crystal samples. The polycrystalline foils of nickel had no special surface preparation; their surfaces were shiny but not mirror-like. This supports the view that transmission measurements, in contrast to reflection (FMR) measurements, are relatively insensitive to surface properties. It is remarkable that the magnetic damping in these polycrystalline foils was found to be as small as that measured in high quality single crystals.

Appendix I

The direction of the magnetization[1] in a magnetized body depends on the applied magnetic field, magnetocrystalline anisotropy, stress, and the shape of the body. Conventionally, demagnetization factors have been used to describe the effect of these various sources on $\vec{M}_o$ (Macdonald 1951). The effective fields constructed from these demagnetization factors are important in the microwave transmission problem not only because they play a role in determining the direction of $\vec{M}_o$, but also because they exert restoring torques once the magnetization has been disturbed from equilibrium.

Consider the shape demagnetization field

$$\vec{H}_D = -4\pi \bar{\bar{D}} \vec{M}. \qquad (2.11)$$

For a body whose surface is described by a second order polynomial, e.g. an ellipsoid, $\vec{M}$ and $\vec{H}_D$ are uniform inside the body (see, for example, Chikazumi 1959). This D has the form

$$\begin{pmatrix} D_{XX} & 0 & 0 \\ 0 & D_{YY} & 0 \\ 0 & 0 & D_{ZZ} \end{pmatrix}$$

when expressed in the $(\hat{X}\hat{Y}\hat{Z})$ co-ordinate system of Fig. 2.3. For an ellipsoid $\nabla\cdot\vec{M}$ is zero everywhere except at the

---

[1]Only the case in which an applied field large enough to eliminate domain structure is of interest here.

surface and, since $\nabla\cdot\vec{B} = 0$, one can visualize $-\nabla\cdot\vec{M}$ as the "charge" which gives rise to the field $\vec{H}_D$ described by

$$\nabla\cdot\vec{H}_D = -4\pi\ \nabla\cdot\vec{M} \qquad \text{(AI.1)}$$

(The samples used in these experiments were usually thin circular discs whose demagnetization factors could be closely approximated by those for an ellipsoid.)

The equilibrium direction of the magnetization, for the simple case in which only shape demagnetization fields were present, was determined by the requirement that there be no net torque on the magnetization,

$$\text{i.e. } \vec{M}_o \times (\vec{H}_o + \vec{H}_D) = 0 \qquad \text{(AI.2)}$$

Next, consider magnetocrystalline anisotropy. The effective fields were obtained from angular derivatives of the magnetocrystalline energy. This energy, which originates from the spin-orbit interaction, cannot be accurately derived from first principles but can be expressed as a series of polynomials in direction cosines consistent with the crystal symmetry. The magnitude of the lowest order terms can be obtained from experiment. For cubic symmetry the first three terms in the energy are

$$E_{C.A.} = K_o + K_1(\alpha_1^2\alpha_2^2 + \alpha_2^2\alpha_3^2 + \alpha_3^2\alpha_1^2) + K_2(\alpha_1^2\alpha_2^2\alpha_3^2) \qquad \text{(AI.3)}$$

where K_o, K_1 and K_2 are constants and

$$\alpha_1 = \sin\phi\cos\psi \qquad \text{(AI.4a)}$$

$$\alpha_2 = \sin\phi\sin\psi \qquad \text{(AI.4b)}$$

$$\alpha_3 = \cos\phi \qquad \text{(AI.4c)}$$

and ϕ,ψ are the angular co-ordinates of the magnetization with respect to the crystal axes. The angular derivatives of $E_{C.A.}$ represents a torque $\vec{L}$ which can be used to determine an effective demagnetization field (or demagnetization factor) through the relation

$$\vec{L} = \vec{M} \times (-4\pi \overline{\overline{D}}\, \vec{M}) \qquad \text{(AI.5)}$$

The concept of using demagnetization factors to determine the direction of M_o becomes cumbersome once anisotropy is included[2]. Comparison of Equation (AI.2) with (AI.5) reveals the artificial nature of demagnetization factors which describe anisotropy. Shape demagnetization factors are useful simply because they can be measured or calculated for special geometries; torques resulting from magnetocrystalline anisotropy are directly available from the energy expression (AI.3).

The demagnetization fields also enter explicitly into the equation of motion for the magnetization, Equation (2.16). Although there is no net torque on the equilibrium magnetization, restoring torques appear once the magnetization has been disturbed from equilibrium. The restoring torques due to the applied magnetic field and the shape demagnetization field are exhibited in the terms of Equation (2.16) containing H_{oZ},

---

[2] All measurements reported in this thesis were made with $\vec{M}_o \parallel \vec{H}_o$ by suitably choosing the direction of $\vec{H}_o$ and the crystal orientation.

and $D_{Z'Z'}$[3]. The restoring torque due to anisotropy is introduced through $\overline{\overline{d}}$ in Equation (2.16). In view of the statements above this is not the most transparent manner to describe the anisotropy effects, but it is the conventional way (Macdonald 1951). The magnetocrystalline restoring torque is

$$\Delta\vec{L} = \frac{\partial\vec{L}}{\partial\phi}\Delta\phi + \frac{\partial\vec{L}}{\partial\psi}\Delta\psi \qquad \text{(AI.6)}$$

where $\Delta\phi$ and $\Delta\psi$ can be expressed in terms of $m_{X'}/M_o$ and $m_{Y'}/M_o$. Expressing this torque as

$$\Delta\vec{L} = (\vec{M}_o \times (-4\pi\ \overline{\overline{d}}\ \vec{m}) \qquad \text{(AI.7)}$$

allows one to determine the elements of $\overline{\overline{d}}$ which appear in Equation (2.16). For a general orientation of the $(\hat{X}'\hat{Y}'\hat{Z}')$ co-ordinate system with respect to the crystal axes, the expressions for the elements of $\overline{\overline{d}}$ are lengthy. Since the experiments were carried out with the magnetization along a few specific crystal directions, the much simpler expressions for $\overline{\overline{d}}$ along these high symmetry directions are given in Table (A.1).

---

[3] Note that $D_{Z'Z'}$ is expressed in the $(\hat{X}'\hat{Y}'\hat{Z}')$ co-ordinate system of Fig. 2.3 whereas $\overline{\overline{D}}$, in the form introduced above, is expressed in the $(\hat{X}\hat{Y}\hat{Z})$ co-ordinate system. The demagnetization tensors are related by a similarity transformation and $D_{Z'Z'} = D_{XX}\sin^2\theta + D_{ZZ}\cos^2\theta$.

Next, consider the effects of magnetostriction. The partieular case of interest here is that of a uniform stress in the plane of a polycrystalline sample. The resultant magnetoelastic energy may be expressed as (Lee 1955)

$$E_\sigma = -\frac{3}{2}\lambda_s \sigma \cos^2\theta \qquad \text{(AI.8)}$$

Here σ is the stress, λ_s the magnetostrictive constant, and θ the angle between the magnetization and the normal to the sample's plane. This energy can be treated in just the same manner as the magnetocrystalline energy to determine the equilibrium direction of the magnetization and the R.F. demagnetization factors associated with magnetostriction. The elements of $\bar{\bar{d}}$ which enter into Equation (2.16) are exhibited in Table (A.2).

Table A.1

Orientation	$d_{X'X'}$	$d_{X'Y'}$ (=$d_{Y'X'}$)	$d_{Y'Y'}$
$\vec{M}_o$ || <100> ||$^{\ell}$ or $\perp$ config.	$\frac{2K_1}{4\pi M_o^2}$	0	$\frac{2K_1}{4\pi M_o^2}$
$\vec{M}_o$ || <111> ||$^{\ell}$ or $\perp$ config.	$\frac{-\frac{4}{3}K_1 - \frac{4}{9}K_2}{4\pi M_o^2}$	0	$\frac{-\frac{4}{3}K_1 - \frac{4}{9}K_2}{4\pi M_o^2}$
$\vec{M}_s$ || <110> $\hat{z}$ || <100> ||$^{\ell}$ config,	$\frac{K_1 + \frac{1}{2}K_2}{4\pi M_o^2}$	0	$\frac{-2K_2}{4\pi M_o^2}$
$\vec{M}_s$ || <110> $\vec{h}_{RF}$ || <100> $\perp$ config.	$\frac{-2K_1}{4\pi M_o^2}$	0	$\frac{K_1 + \frac{1}{2}K_2}{4\pi M_o^2}$
$\vec{M}_s$ || <110> $\hat{z}$ || <110> ||$^{\ell}$ config.	$\frac{-2K_1}{4\pi M_o^2}$	0	$\frac{K_1 + \frac{1}{2}K_2}{4\pi M_o^2}$
$\vec{M}_s$ || <110> $\vec{h}_{RF}$ || <110> $\perp$ config.	$\frac{K_1 + \frac{1}{2}K_2}{4\pi M_o^2}$	0	$\frac{-2K_1}{4\pi M_o^2}$

Table A.2

θ	$d_{X'X'}$	$d_{X'Y'}$ $(=d_{Y'X'})$	$d_{Y'Y'}$
0°	$\frac{3\lambda_s\sigma}{4\pi M_o^2}$	0	0
90°	$\frac{-3\lambda_s\sigma}{4\pi M_o^2}$	0	$\frac{-3\lambda_s\sigma}{4\pi M_o^2}$

Appendix II

The procedure outlined in Equations (2.16) to Equation (2.18) of Chapter 2 result in the following expressions for the permeability:

$$\mu_{X',X'} = 1 + 4\pi\Delta^{-1}[M_o((H_{oZ'} - 4\pi D_{Z',Z'},M_o) - \frac{2Ak^2}{M_o} + 4\pi d_{Y',Y'},M_o + \frac{\lambda}{\gamma M_o}(4\pi d_{X',Y'},M_o)) + \frac{\omega}{\gamma}(\frac{i\lambda}{\gamma} - 4\pi d_{X',Y'},M_o + \frac{\lambda}{\gamma M_o}((H_{oZ'} - 4\pi D_{Z',Z'},M_o) - 2\frac{Ak^2}{M_o} + 4\pi d_{Y',Y'},M_o)].$$

$$\mu_{X',Y'} = 4\pi\Delta^{-1}[M_o(\frac{i\omega}{\gamma} - 4\pi d_{X',Y'},M_o + \frac{\lambda}{\gamma M_o}((H_{oZ'} - 4\pi D_{Z',Z'},M_o) - \frac{2Ak^2}{M_o} + 4\pi d_{Y',Y'},M_o)) + \frac{\lambda}{\gamma}((H_{oZ'} - 4\pi D_{Z',Z'},M_o) - 2\frac{Ak^2}{M_o} + 4\pi d_{Y',Y'},M_o + \frac{\lambda}{\gamma M_o}(4\pi d_{X',Y'},M_o))].$$

$$\mu_{Y',X'} = 4\pi\Delta^{-1}[-M_o(\frac{i\omega}{\gamma} + 4\pi d_{Y',X'},M_o + \frac{\lambda}{\gamma M_o}(H_{oZ'},-4\pi D_{Z',Z'},M_o) - 2\frac{Ak^2}{M_o} + 4\pi d_{X',X'},M_o)) + \frac{\lambda}{\gamma}((H_{oZ'},-4\pi D_{Z',Z'},M_o) - 2\frac{Ak^2}{M_o} + 4\pi d_{X',X'},M_o - \frac{\lambda}{\gamma M_o}(4\pi d_{Y',X'},M_o))].$$

$$\mu_{Y',Y'} = 1 + 4\pi\Delta^{-1}[M_o((H_{oZ'} - 4\pi D_{Z',Z'},M_o) - 2\frac{Ak^2}{M_o}$$

$$+ 4\pi d_{X',X'},M_o - \frac{\lambda}{\gamma M_o}(4\pi d_{X',Y'},M_o))$$

$$+ \frac{\omega}{\gamma}(\frac{i\omega}{\gamma} + 4\pi d_{Y',X'},M_o + \frac{\lambda}{\gamma M_o}((H_{oZ'} - 4\pi D_{Z',Z'},M_o)$$

$$- 2\frac{Ak^2}{M_o} + 4\pi d_{X',X'},M_o)].$$

$$\mu_{Z',Z'} = 1$$

$$\mu_{X',Z'} = \mu_{Y',Z'} = \mu_{Z',X'} = \mu_{Z',Y'} = 0$$

$$\Delta = [\frac{i\omega}{\gamma} + 4\pi d_{Y',X'},M_o + \frac{\lambda}{\gamma M_o}((H_{oZ'} - 4\pi D_{Z',Z'},M_o)$$

$$- 2\frac{Ak^2}{M_o} + 4\pi d_{X',X'},M_o)]$$

$$\times[\frac{i\omega}{\gamma} - 4\pi d_{X',Y'},M_o + \frac{\lambda}{\gamma M_o}((H_{oZ'} - 4\pi D_{Z',Z'},M_o)$$

$$- 2\frac{Ak^2}{M_o} + 4\pi d_{Y',Y'},M_o)]$$

$$+ [(H_{oZ'} - 4\pi D_{Z',Z'},M_o) - 2\frac{Ak^2}{M_o} + 4\pi d_{Y',Y'},M_o$$

$$+ \frac{\lambda}{\gamma M_o}(4\pi d_{X',Y'},M_o)]$$

$$\times[(H_{oZ'} - 4\pi D_{Z',Z'},M_o) - 2\frac{Ak^2}{M_o} + 4\pi d_{X',X'},M_o$$

$$- \frac{\lambda}{\gamma M_o}(4\pi d_{Y',X'},M_o)].$$

In these expressions the static demagnetization factor $D_{z'z'}$ refers to the shape of the material only. The effect of magnetocrystalline anisotropy and magnetostriction are contained in $\overline{\overline{d}}$.

Of course, Maxwell's equations must be combined with the above expressions to obtain the propogation constants which describe the waves inside the magnetic material.

Appendix III

Exchange does not play an essential role in the interpretation of the data presented in this thesis. However, it is worthwhile to note how exchange alters the calculations of Chapter 2.

From the equation of motion, Equation (2.16), one can observe that

$$\begin{pmatrix} f_{11}(k^2) & f_{12}(k^2) \\ f_{21}(k^2) & f_{22}(k^2) \end{pmatrix} \begin{pmatrix} m_{X'} \\ m_{Y'} \end{pmatrix} = \begin{pmatrix} g_{11} & g_{12} \\ g_{21} & g_{22} \end{pmatrix} \begin{pmatrix} h_{X'} \\ h_{Y'} \end{pmatrix} \qquad \text{(AIII.1)}$$

where $f_{ij}(k^2)$ is a first order polynomial in k^2 and g_{ij} is independent of k. The solution of Maxwell's equations in the slab geometry of Fig. 2.3 requires that h and m be related by:

$$\begin{pmatrix} h_X \\ h_Y \\ h_Z \end{pmatrix} = \begin{pmatrix} \frac{-4\pi}{ik^2\delta^2+1} & 0 & 0 \\ 0 & \frac{-4\pi}{ik^2\delta^2+1} & 0 \\ 0 & 0 & -4\pi \end{pmatrix} \begin{pmatrix} m_X \\ m_Y \\ m_Z \end{pmatrix} \qquad \text{(AIII.2)}$$

Equation (AIII.2) must be transformed into the same co-ordinate system as Equation (AIII.1) via rotation about the Y-axis. The outcome of this similarity transformation is of the form

$$\begin{pmatrix} h_{X'} \\ h_{Y'} \\ h_{Z'} \end{pmatrix} = \begin{pmatrix} \frac{U_{11}(k^2)}{ik^2\delta^2+1} & 0 & \frac{U_{13}(k^2)}{ik^2\delta^2+1} \\ 0 & \frac{-4\pi}{ik^2\delta^2\ 1} & 0 \\ \frac{U_{31}(k^2)}{ik^2\delta^2+1} & 0 & \frac{U_{33}(k^2)}{ik^2\delta^2+1} \end{pmatrix} \begin{pmatrix} m_{X'} \\ m_{Y'} \\ m_{Z'} \end{pmatrix} \tag{AIII.3}$$

where the $U_{ij}(k^2)$ are a linear combination of the $f_{ij}(k^2)$. Since $m_{Z'} = 0$ (Equation (2.16c)), the terms in Equation (AIII.3) involving $m_{Z'}$ can be dropped and the expression for $h_{Z'}$ can be treated separately. Comparison of Equations (AIII.1) and (AIII.3) then shows that

$$\begin{pmatrix} f_{11}(k^2) & f_{12}(k^2) \\ f_{21}(k^2) & f_{22}(k^2) \end{pmatrix} - \begin{pmatrix} g_{11} & g_{12} \\ g_{21} & g_{22} \end{pmatrix} \begin{pmatrix} \frac{U_{11}(k^2)}{i\delta^2k^2+1} & 0 \\ 0 & \frac{-4\pi}{i\delta^2k^2+1} \end{pmatrix} = 0 \tag{AIII.4}$$

One immediately sees that the secular equation associated with Equation (AIII.4) is quartic in k^2. Thus there are four different propagation constants, or four eigenmodes, for the system. For comparison, the no-exchange case results in f_{ij} independent of k^2 and the secular equation is quadratic in k^2, i.e. there are only two eigenmodes of the system. The two additional modes, or waves, introduced by exchange are spin-wave-like excitation of the system. (See, for example, Gurevich (1960).)

In the calculations presented in Chapter 2 there were just enough boundary conditions to specify all reflected and transmitted waves in terms of the incident wave. The introduction of two extra modes requires that more boundary conditions be specified. The R.F. magnetization may be an anti-node at the surface of the magnetic material (Ament and Rado 1955),

$$\text{i.e.} \quad \left.\frac{\partial m_X}{\partial Z}\right|_{\text{surface}} = \left.\frac{\partial m_Y}{\partial Z}\right|_{\text{surface}} = 0 \qquad \text{(AIII.5)}$$

where X,Y,Z refer to the co-ordinate system introduced in Fig. 2.3. Alternatively, the R.F. magnetization may be pinned in some particular direction, i.e. there is a node of the R.F. magnetization at the surface of the slab. The most reasonable choices for the direction of the pinned magnetization is either perpendicular to the surface or parallel to the magnetization. Then the boundary condition on the magnetization is

$$\left.\vec{m}\right|_{\text{surface}} = 0 \qquad \text{(AIII.6)}$$

More generally, the surface boundary condition can be derived from the torque exerted on the magnetization by a surface anisotropy. Depending on the strength of the anisotropy, boundary conditions intermediate between (AIII.5) and (AIII.6) can be described. (See, for example, Rado and Weertman (1959) and Cochran et al. (1977a).) In any event, one can use

a boundary condition on the magnetization which allows the determination of all the reflected and transmitted waves in a magnetic sample in terms of the incident wave.

Appendix IV

The final thinning of the nickel single crystal samples was done using a specially built electropolishing apparatus. This electropolisher was very similar to the acid polishing wheel described by Young and Wilson (1961) but modified for electropolishing.

The heart of the electropolisher is illustrated in Fig. AIV.1. In operation, a disc shaped sample was mounted on the end of a rotating shaft with the plane of the disc normal to the axis of rotation of the shaft. This shaft rotated at 35 rpm. The sample was normally held 1/4 to 1/2 mm from the face of a 20 cm diameter stainless steel polishing wheel. The wheel was covered by a fiberglass cloth held in place by a rubber O-ring. This polishing wheel was partially submerged in electrolyte (390 ml H_2SO_4 and 290 ml H_2O); Tegart (1959)) and rotated at 15 rpm. Thus fresh electrolyte impregnating the fiberglass cloth was constantly drawn up into the region between the sample (anode) and polishing wheel (cathode). The polishing was carried out at a rate of 0.1μm/sec (current density of 0.4 A/cm^2). The shaft to which the sample was attached was mounted on a bed which slid on two steel rods so that the sample could be brought up to the face of the polishing wheel. Every 60 to 90 seconds the sample was slid back from the face of the polishing wheel approximately 10 cm and washed with a stream of distilled water.

The bed which carried the sample could also be rotated about the vertical and horizontal axes. This facilitated alignment of the axis of the shaft carrying the sample so that it was perpendicular to the plane of the polishing wheel. The bed could also be translated horizontally to position the sample at different distances from the axis of the polishing wheel.

Two different schemes were used to mount the nickel samples to the end of the rotating shaft. In the first polishing cycles the sample was attached to a glass slide with beeswax. A #40 gauge copper wire lead was silver painted to the back edge of the sample through a hole in the glass slide, Fig. AIV.2. The glass slide was in turn attached to a lucite cylinder with nail polish and the wire connected to a slip ring on the lucite cylinder. The cylinder was then attached to the rotating shaft (Fig. AIV.2).

A typical sample disc, 200μm thick and 1.2 cm in diameter, was mounted and dismounted several times in the course of removing 80 to 100μm from each side. Once the sample was less than 20μm thick, as determined from area and weight measurements, a second mounting shceme was used. The nickel sample was attached with silver paint to a flat, polished and annealed polycrystalline nickel diaphragm. This diaphragm was then mounted on the glass slide in the manner indicated above. The wire lead was attached to the nickel diaphragm, not to the fragile sample. The portion of the nickel diaphragm exposed to electrolyte was masked off with

beeswax so that only the sample was wetted by the electrolyte. Care had to be taken to insure that no silver paint near the edge of the sample came in contact with the electrolyte as this caused a black deposit to form on the sample.

These sample mounting procedures had the virtue that little handling of the nickel sample itself was involved. The sample was mounted on the glass slide by placing it over the appropriate spot on the (heated) glass slide previously coated with beeswax. Once the slide cooled and the beeswax hardened, the sample was securely mounted. The sample was dismounted by placing the sample plus glass slide in trichloroethylene for three or more hours. This dissolved the beeswax and the sample floated off the slide. Mounting and dismounting the sample from the nickel diaphragm, though different in detail, was equally simple.

The electropolisher, used in the manner described above, was capable of producing flat single crystal samples with a thickness uniform to $\approx$ 1μm over a diameter of 5mm.

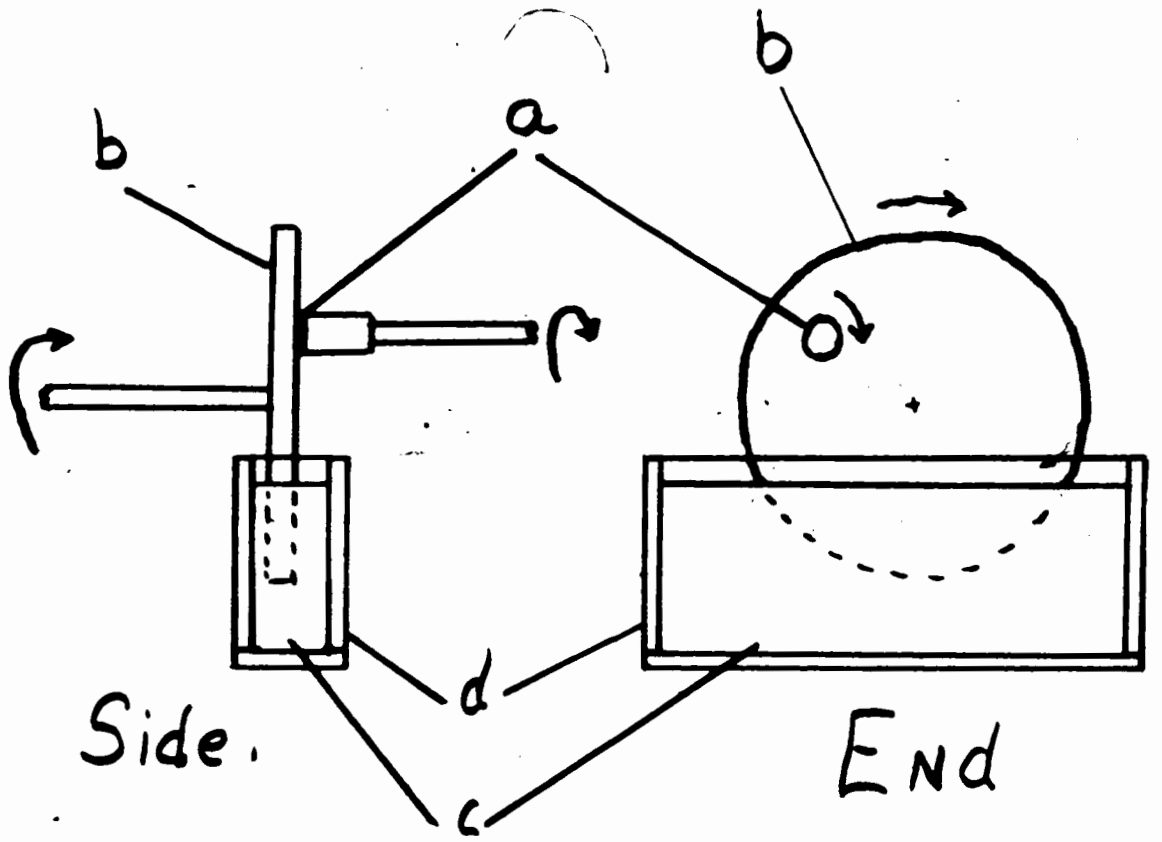

Fig. AIV.1: Side and end schematic views of electropolishing apparatus. The sample (a) on the end of a rotating shaft is almost in contact with the polishing wheel (b). The polishing wheel rotates through an acid bath (c) contained in a lucite box (d).

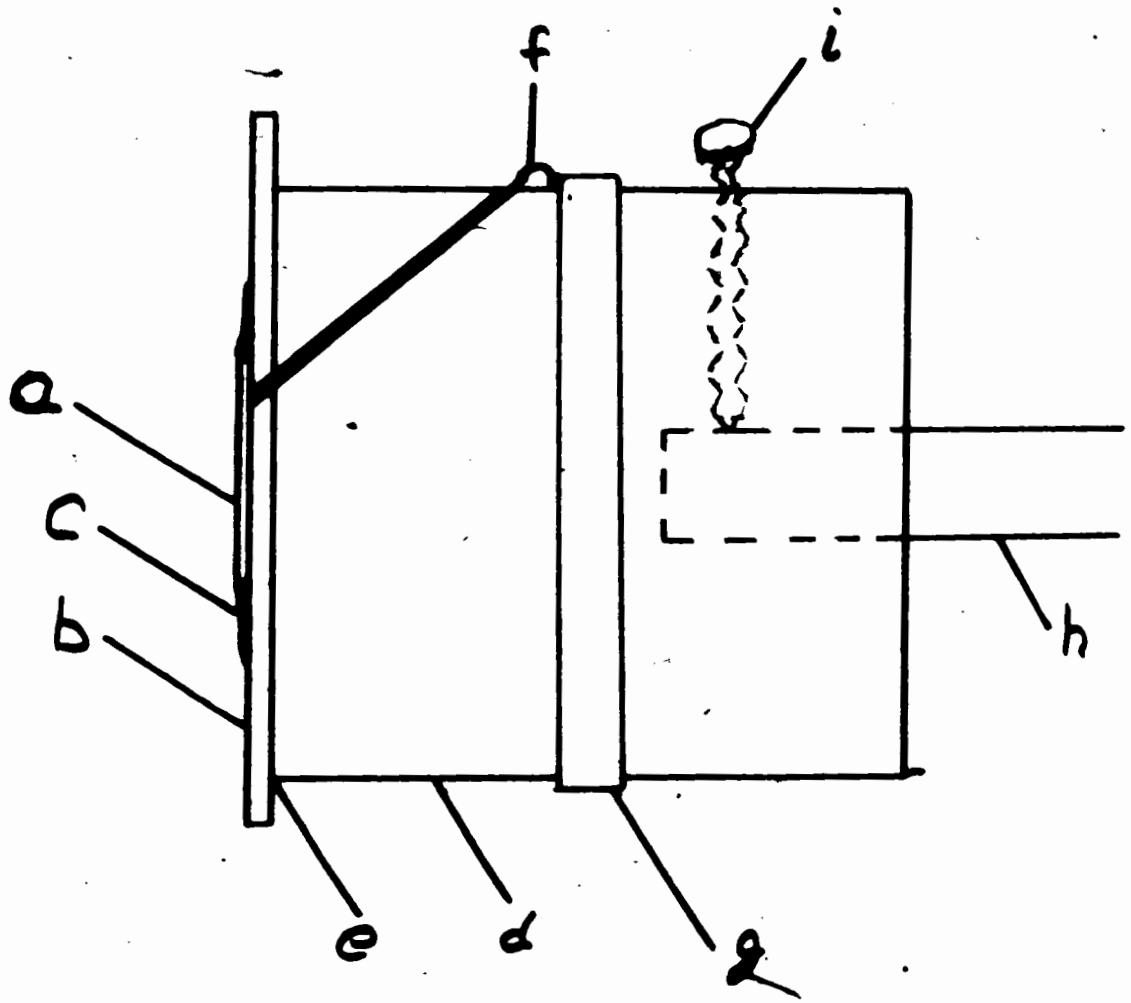

Fig. AIV.2: Sample mounting detail. The sample (a) is attached to a glass slide (b) with beeswax (c). The glass slide is attached to a lucite cylinder (d) with a thin layer of nailpolish (e). A wire (f), attached to the back of the sample with silver paint, is attached to a commutator (g). The lucite cylinder fits over the end of a steel shaft (h) and is held in place by the set screw (i).

REFERENCES

Aldred, A.T. 1975. Phys. Rev. B11, 2597.

Ament, W.S. and Rado, G.T. 1955. Phys. Rev. 97, 1558.

Anders, W., Bastian, D., and Biller, L. 1971. Z. Angew. Phys. 32, 12.

Arlinghaus, F.J. and Reck, R.A. 1975. Phys. Rev. B11, 3488.

Arrott, A. and Noakes, J.E. 1978. Phys. Rev. Lett. 19, 786.

Berger, L. To be published in J. Phys. Chem. Solids.

Bhagat, S.M. and Chichlis, E.P. 1969. Phys. Rev. 178, 828.

Bhagat, S.M. and Hirst, L.L. 1966. Phys. Rev. 151, 401.

Bhagat, S.M. and Rothstein, M.S. 1971. J. Phys. (Paris) 32, C1-777.

Bloembergen, N. 1950. Phys. Rev. 78, 572.

Birss, R.R. and Lee, E.W. 1960. Proc. Phys. Soc. (London) 76, 502.

Chikazumi, S. Physics of Magnetism. 1959. (John Wiley & Sons, Inc., New York.)

Cochran, J.F., Heinrich, B. and Dewar, G. 1977(a). Can. J. Phys. 55, 787.

Cochran, J.F., Heinrich, B. and Dewar, G. 1977(b). Can. J. Phys. 55, 834.

Dewar, D, Heinrich, B. and Cochran, J.F. 1977. Can. J. Phys. 55, 821.

Ferromagnetic Resonance, 1966. Ed. by S.V. Vonsovskii, trans. by H.S.H. Massey, trans ed. by D. ter Haar (Pergamon Press, Toronto).

Gilbert, T.L. 1955. Phys. Rev. 100, 1243.

Gold, A.V. 1974. J. Low Temp. Phys. 16, 3.

Griffiths, J.H.E. 1946. Nature 158, 670.

Gurevich, A.G. Ferrites at Microwave Frequencies. 1960. Trans. by Tybulewicz, A. 1963. (Consultants Bureau Enterprises,

Inc., New York.)

Heinrich, B. and Mescheryakov, V.F. 1969. ZhETF Pis. Red. 9, 378 (1969).

Heinrich, B. and Mescheryakov, V.F. 1970. Zh. Eksp. Theor. Fiz. 59, 424. Soviet Phys. JETP 32, 232 (1971).

Herring, C. and Kittel, C. 1951. Phys. Rev. 81, 869.

Jackson, J.D. Classical Electrodynamics. 1962. (John Wiley & Sons, Inc., New York.)

Kaganov, M. 1959. Fiz. Met. Metallov. 7, 287.

Kambersky, V. 1970. Can. J. Phys. 48, 2906.

Kittel, C. 1949. Phys. Rev. 76, 743.

Korenman, V. and Prange, R.E. 1972. Phys. Rev. B6, 2769.

Korenman, V., Murray, J.L. and Prange, R.E. 1977. Phys. Rev. B16, 4032, 4048 and 4058.

Kraus, L. and Frait, Z. 1973. Czech. J. Phys. B23, 188.

Landau, L. and Lifshitz, E. Physik. Z. Sowjetunion 8, 153.

Lee, E.W. 1955. Rep. Prog. Phys. 18, 184.

Lewis, R.B., Alexandrakis, G.C., and Carver, T.R. 1966. Phys. Rev. Lett. 17, 854.

Lyall, K. 1970. Electromagnetic Generation of Acoustic Waves in Metals; Applications to Ultrasonic Measurements. 1970. (Thesis, unpublished.)

MacDonald, J.R. 1951. Proc. Phys. Soc. (London) A64, 1968.

Marcus, S.M. and Langenberg, D.N. 1963. J. Appl. Phys. 34, 1367.

Metals Handbook, 1961. 8th ed., ed. by Taylor Lyman (American Society for Metals, Metals Park, Ohio.)

Mott, N.F. and Jones, H. The Theory of the Properties of Metals and Alloys. 1936. (Dover Publications, Inc., New York.)

Okamoto, T. et al. 1966. J. Sci. Hiroshima Univ. 31, 11.

Pippard, A.B. The Dynamics of Conduction Electrons. 1971. (Gordon and Breach, New York.)

Potter, H.H. 1931. Proc. Roy. Soc. A132, 560.

Rado, G.T. and Weertman, J.R. 1959. J. Phys. Chem. Solids 11, 315.

Rodbell, D.S. 1964. Phys. Rev. Lett. 13, 471.

Rodbell, D.S. 1965. Physics 1, 279.

Salamon, M.B. 1967. Phys. Rev. 155, 224.

Schmidt, L.B., Case, W.E., and Harrington, R.D. 1964. National Bureau of Standards Technical Note 221.

Simmons, G. and Wang, H. Single Crystal Constants and Calculated Aggregate Properties: A Handbook. 1971. 2nd ed. (The M.I.T. Press, Cambridge, Mass.)

Singh, M., Calloway, J., and Wang, C.S. 1976. Phys. Rev. B14, 1214.

Tegart, W.J. McG. Electrolytic Polishing of Metals and Alloys. 1959. 2nd ed. (Pergamon Press, London.)

Thermophysical Properties of High Temperature Solid Materials. 1967. ed. by Y.S. Touloukian. (The Macmillan Company, New York.)

VanderVen, N.S. 1967. Phys. Rev. Lett. 18, 277.

Weiss, P. and Forrer, R. 1926. Ann. Phys. (Paris) 5, 153.

White, G.K. and Woods, S.B. 1958. Roy. Soc. Phil. Trans. (London) A251, 273.

Young, F.W. and Wilson, T.R. 1961. Rev. Sci. Inst. 32, 559.